

ATOMISTIC MODELING OF CRACK TIP BEHAVIOR IN DUCTILE MATERIALS

A Dissertation

Presented to the Faculty of the Graduate School

of Cornell University

in Partial Fulfillment of the Requirements for the Degree of

Doctor of Philosophy

by

Wenjia Gu

May 2021

© 2021 Wenjia Gu
ALL RIGHTS RESERVED

ATOMISTIC MODELING OF CRACK TIP BEHAVIOR IN DUCTILE MATERIALS

Wenjia Gu, Ph.D.

Cornell University 2021

This dissertation is composed of three papers and related unpublished work that laid the foundation for the succeeding scientific discoveries. The first two papers detail work intended to illuminate the atomic-scale mechanisms governing the near threshold fatigue crack growth phenomenon. First, by harnessing a concurrent multiscale approach and contemporary computational resources, fatigue crack simulations with cycle counts well beyond those analyzed previously have been performed. The validity of long-hypothesized material separation mechanisms thought to control near threshold fatigue crack growth in vacuum is assessed. Results show that fatigue crack growth arrests after an initial transient period, reconciling reports of crack growth in atomistic simulations at loading amplitudes below experimental crack growth thresholds. It is also observed that sustained crack growth in vacuum only occurs when emitted dislocations return to the crack tip on a slip plane behind its original one, which is resulted from slip trace intersection in the 2D simulated system and is expected to occur in 3D crystals by other additional mechanisms. Second, building upon the concurrent atomistic-continuum multiscale modeling framework, the isolated effect of material dissolution on crack growth is investigated. A series of dissolution simulations are carried out with different loading conditions and dissolution rates. Simulation results and subsequent quantitative analysis suggest that while dissolution is capable of freeing arrested fatigue cracks, the crack tip is always blunted under both static and cyclic loading, implying that dissolution has an overall crack arresting effect, and the dissolution-induced-blunting is found to be independent of the mechanical loading magnitude. Finally, from a standpoint of how

state-of-the-art engineering and technology can be applied to other applications in an attempt to directly better the human condition, the third paper details a field work about the assessment of additive manufacturing for increasing sustainability and productivity of smallholder agriculture. This study analyzes and compares different manufacturing approaches from the perspectives of structural performance and cost efficiency and seeks to provide solutions to the mechanical obstacles encountered by smallholder farmers in the field. The acquired data suggests that the material extrusion 3D printing technology is able to provide functional parts more rapidly, accelerating the design cycle, and lowering cost relative to local fabrication routes, while traditional means is proved to be more economical in the case where mechanical performance of the part is the most critical.

BIOGRAPHICAL SKETCH

Wenjia Gu grew up in Laiwu, Shandong Province, China. She graduated from Jinan Foreign Language School in 2010 and was recommended for admission to Tianjin University without taking the national college entrance exam. In spring 2012, she transferred to University of Illinois at Urbana - Champaign to study Civil Engineering with concentrations in Structural Engineering and Construction Management. After graduating Magna Cum Laude in 2014 with a Bachelor of Science in Civil Engineering, she began her graduate study in the Department of Civil and Environment Engineering at Massachusetts Institute of Technology. She earned her Master of Engineering degree in High Performance Structures in 2015, and then joined Professor Derek Warner for the graduate research at Cornell University. Starting from 2017, she served in a leadership role in the Cornell Chinese Students and Scholars Association and was selected as the Vice President in 2019. In her spare time, Wenjia likes to travel, read, swim and play piano.

To the whole research group for a friendly and collaborative environment.

To all my friends for bringing so much joy and fun into my life.

To my family for all the unconditional love and support that I can never ask for more.

To my best friend Xiaoshu for your company over the past seven years.

ACKNOWLEDGEMENTS

I would first like to thank my advisor, Professor Derek Warner, for all his valuable advice, generous help and kind encouragement throughout my time at Cornell. Second, I would like to thank Professor Christopher Earls for the warm support he gave me from the beginning of this program and for the useful advice ever since. Third, I would like to thank Professor Matthew Peter Miller for participating in my graduate committee and providing me with helpful feedback. In addition, I would like to thank Professor Erika Styger for being such an insightful and patient advisor in the interdisciplinary project. I would also like to thank my friend and formal colleague, Peipei Li, for her invaluable help and company since I joined the group. Finally, I gratefully acknowledge support from W.A. Curtin, A.K. Vasudevan, S. Lynch, the US Office of Naval Research (Grant No. N00014-17-1-2035), and the Ross-Teteman Fellowship, as well as Cornell University's Atkinson Center.

TABLE OF CONTENTS

Biographical Sketch	iii
Dedication	iv
Acknowledgements	v
Table of Contents	vi
List of Tables	viii
List of Figures	ix
1 Introduction	1
1.1 Background Information	1
1.2 Thesis Statement	3
2 Research Context	7
2.1 Basics of Fatigue	7
2.2 Effect of Temperature	10
2.3 Material Potential Development	12
2.4 Isolating the Atomistic Simulation	17
2.5 Multiscale Model Development and Verification	20
2.6 Multiscale simulation of fatigue crack behavior in materials with different intrinsic ductility	24
2.7 Multiscale simulation of fatigue crack behavior with annealing	28
2.8 Multiscale simulation of fatigue crack behavior under Mode I + II loading	30
3 Atomic mechanism of near threshold fatigue crack growth in vacuum	34
3.1 Methods	46
4 Dissolution at a Crack Tip	52
5 Assessment of Additive Manufacturing for Increasing Sustainability and Productivity of Smallholder Agriculture	63
5.1 Introduction	63
5.2 Current mechanical obstacles in SRI adoption	65
5.2.1 Lahore, Pakistan	65
5.2.2 Uttarkhand, India	66
5.2.3 Selangor, Malaysia	67
5.2.4 Ségou Region, Mali	68
5.2.5 Bogotá, Columbia	69
5.2.6 Summary of field partner interactions	70
5.3 Case 1: Jang JP-1 push seeder roller	72
5.3.1 Traditional fabrication	73
5.3.2 Additive manufacturing cost	76
5.4 Case 2: Mandava weeder rotor	82
5.4.1 Traditional fabrication cost	82
5.4.2 Additive manufacturing cost	86

5.5	Summary and Conclusion	88
6	Conclusion and Future Work	91

LIST OF TABLES

2.1	Results of code verification of the displacement field. Units are normalized. The remaining error (which is deemed acceptable) is due to the analytic solution not accounting for the actual shape of the crack tip, and the linear shape functions used in the finite element analysis in the continuum domain.	23
5.1	Unit cost of producing different numbers of rollers for the JP-1 seeder via various fabrication methods (information obtained from field partners in April 2018 and from U.S. companies in April 2019). The prototyping unit cost was calculated from the initial investment cost and the fixed direct unit cost only, without considering the possibility of subsequent production volumes.	75
5.2	Model variables and values for AM cost estimation.	77
5.3	Unit cost of producing the Mandava weeder rotor via various fabrication methods. The quotes were obtained from field partners in April 2018 and from U.S. machine shops in February 2018. Quotes for additive manufacturing were obtained in June 2018. LASSP and CEE machine shops are both on the Cornell Ithaca NY campus.	84
5.4	Manufacturing cost breakdown of producing one Mandava weeder rotor at two Cornell University machine shops in Ithaca, U.S. (quotes obtained in February 2018).	85
5.5	Shipping cost of 50 rotors from the U.S. (quotes obtained in April 2019).	86

LIST OF FIGURES

2.1	Three regions of the fatigue fracture process.	8
2.2	Schematic drawings of Mode I, Mode II and Mode III loading.	10
2.3	Interatomic potentials with tunable intrinsic ductility in 2D. (a) Energy; and (b) Force vs interatomic separation distance. Units are normalized (source [1]).	14
2.4	Energy vs interatomic separation of Potential A and new potential with 4 times deeper energy well. Units are normalized. Curve of Potential A is shifted downwards for better comparison.	15
2.5	Energy vs interatomic separation of original Potential A and the extended Potential A with next nearest neighbor interactions included. Units are normalized. The two potentials have the same properties. Different numbers of counted bonds and different equilibrium atomic spacing lead to shifting of the energy curve.	16
2.6	Decohesion energy vs nominated interatomic separation (by equilibrium atomic spacing) from Potential A, extended Potential A, EAM potential and the new potential by superposition. Units are normalized.	17
2.7	Specimens under static Mode-I loading showing only atoms with a centrosymmetry parameter not equal to that of the perfect hexagonal crystal, i.e. atoms at the crack surface, boundaries, clusters around alloy atoms, and dislocation cores. (a) Potential A simulation with no dislocation insertion; (b) Potential A simulation after 38 dislocations inserted; (c) Potential A simulation with solute atoms after 38 dislocations inserted. Insertion of dislocations is shown to promote the plastic deformation and crack growth.	19
2.8	Plots of crack growth vs loading cycles from hexagonal lattice simulations for a range of atomistic window sizes with Potential A. Curves in different colors represent results from simulations with different atomistic domain sizes. The applied stress intensity range, ΔK , varies from 9.0 to 21.0. Cracks arrest at lower loads, and tend to grow as load increases. The effect of window size is shown to be not significant.	26
2.9	Plots of crack growth vs loading cycles from hexagonal lattice simulations with Potential C. The applied stress intensity range, ΔK , varies from 12.0 to 24.0. The size of the atomistic window is $[357 b \times 87 b]$. Crack arrest, cleavage and closure are observed.	27
2.10	Atomistic domain in cyclic loading simulation with Potential A ($\Delta K = 19.5$). Only atoms with a centrosymmetry parameter not equal to that of the perfect hexagonal crystal are shown in the left figures, i.e. atoms at the crack surface, continuum-atomistic interface, and dislocation cores. An artificial defect is formed near the bottom interface due to dislocation pile-up.	28

2.11	Plots of (a) temperature, and (b) pressure of the system during the annealing process. Units are normalized. Pressure of the system was maintained throughout the process.	29
2.12	Plots of crack growth vs loading cycles from ductile hexagonal lattice simulations with annealing introduced at different steps of each loading cycle. The applied stress intensity range, ΔK , varies from 9.0 to 16.0. Annealing is shown to promote crack growth.	29
2.13	Plots of crack growth, crack opening and crack surface offset vs loading cycles from ductile hexagonal lattice simulations under pure mode I and mixed-mode I+II loading. The applied stress intensity range, ΔK , varies from 6.0 to 11.5.	32
2.14	Atomistic domain in ductile hexagonal lattice simulation with $\Delta K = 11.5$ under mixed-mode I+II loading. Only atoms with a centrosymmetry parameter not equal to that of the perfect hexagonal crystal are shown in the left figures, i.e. atoms at the crack surface, continuum-atomistic interface, and dislocation cores. (a) Initial configuration at $K = 0.0$; (b) At the end of the 20 th cycle; (c) At the end of the 40 th cycle; (d) At the end of the 60 th cycle. Increasing crack opening and decreasing crack length can be observed.	33
3.1	Crack advance as a function of loading cycle from three sets of simulations. (a) {113} crack in an f.c.c. aluminum lattice. Each curve represents a distinct dislocation glide resistance in the continuum domain. The majority of cases show crack growth over the first 20 cycles and crack arrest shortly after. On the right, the location of the arrested cracks are shown as a function of glide resistance, showing no correlation between the two variables. (b) A ductile hexagonal lattice at various loading amplitudes. Again, cracks arrest after an initial transient period. Cases are shown both with and without dislocation passing from atomistic to continuum domains to establish that blocking dislocation motion does not influence the behavior. The right shows the dislocation distribution and the crack tip configuration for an arrested crack. (c) A ductile hexagonal lattice with no dislocation passing at larger cycle counts and higher loading amplitudes. Crack arrest was observed in all but a few cases at the higher loading amplitudes. The right image is a plot of $\log(da/dN)$ vs. $\log(\Delta K)$ from the first 10 cycles showing the data conforms to Paris' law, consistent with previous atomistic simulations that analyzed crack growth in the initial transient period. m represents the Paris law exponent, i.e. log-log slope. For the hexagonal lattice simulations, distances are normalized by interatomic spacing, b , and stress intensities are normalized by the stress intensity required to nucleate the first dislocation, $\Delta K^* = \Delta K_I / K_I^{nuc}$	37

3.2	Crack advance as a function of loading cycle from three sets of simulations. Sample continuum and atomistic configurations are shown from when the crack reaches an arrested state. (a) Simulations with slip irreversibility, where dislocation motion is limited to the direction away from the crack tip. (b) Simulations with dislocation sources in the continuum, which exhibit enhanced crack growth over the initial cycles, but eventually crack arrest. (c) Simulations with pre-existing dislocations in the continuum aligned as a PSB. The presence of the PSB dislocations enhances growth over the initial cycles, but eventually crack arrest occurs. Details about SET A, B, and C in (b) and (c) are discussed in the methods section. Distances are normalized by interatomic spacing, b , and stress intensities are normalized by the stress intensity required to nucleate the first dislocation, $\Delta K^* = \Delta K_I / K_I^{nuc}$	42
3.3	(a ₁)-(a ₆): Schematic of crack advance by slip trace intersection. Atom are colored to show deformation. A case is shown where the slip trace of a dislocation nucleated from the crack tip intersects the slip trace of a dislocation on a different slip plane. The intersection results in a change in slip plane when the dislocations return to their original position on the unload. This process leads to the removal of an atom from the crack tip without diffusion. Atom highlighted in yellow in (a ₆) is the companion to the vacancy that was created at the crack tip. (b) Crack growth vs. number of cycles with the slip plane of emitted dislocations being changed prior to their absorption into the crack on the unload. The results show that shifting the slip plane of emitted dislocations backwards (in the opposite direction of crack growth) produces sustained crack growth, consistent with the schematic in (a ₁)-(a ₆). Crack closure was observed in the case when the slip planes were shifted forward, and no crack growth was observed when dislocations were shifted forward and backward in equal proportion. Distances are normalized by interatomic spacing, b , and stress intensity by the stress intensity required to nucleate the first dislocation, $\Delta K^* = \Delta K_I / K_I^{nuc}$	43
3.4	Example of crack growth by the intersection of slip traces in a hexagonal lattice simulation, [600b x 300b] $\Delta K^* = 3.09$. The black dislocation dipole in (a) highlights a dislocation that has been emitted from the crack on the upload of cycle 82. Upon further loading, (b) shows the slip trace of the emitted dislocation (black line) having been intersected by an other dislocation slip trace. Upon unloading, (c) shows the highlighted emitted dislocation having returned to the crack tip in an offset location, leaving a pair of offset slip trace segments and removing an atom from the crack tip. Atoms are colored by strain relative to perfect lattice to illuminate dislocation cores.	45

3.5	Multiscale simulation set up for the $\langle 471 \rangle / \langle 113 \rangle$ crack orientation in which an atomistic domain (right) is embedded in a linear elastic continuum domain (left). Dislocations can move between domains on their corresponding slip planes. The lengths given in this figure are normalized with respect to the burgers vector b , and the images are not drawn to scale. The continuum coloring represents the macroscopic displacement in the y direction and the atomistic coloring corresponds to the potential energy of the atoms, highlighting an edge dislocation that has been emitted from the crack tip.	49
3.6	(a) Source-insertion simulation set up. In each set, an array of three Frank-Read sources was inserted into the continuum just outside the atomistic window on each side of the crack. The sources within each array were set apart by $20b$, and each source emitted a dislocation dipole when its total resolved shear stress exceeded a critical value along the slip plane. The dislocation entering the atomistic window was constructed to be an anti-shielding dislocation gliding towards the crack tip region. (b) PSB simulation set up. In each set, a pre-existing persistent slip band (PSB) with width of $10b$ and spacing of $200b$ was constructed following the schematics by M.D. Sangid [2]. The PSB was arranged to intersect the crack tip region. The lengths given in this figure are normalized with respect to the burgers vector b , and the images are not drawn to scale.	50
3.7	Illustration of slip plane shifting implementation. (a) When a dislocation (black) nucleated from the crack tip and glided across the detection band inside the atomistic domain, (b) its slip plane was shifted after being passed across the interface (red). In order to maintain the correct displacement fields of both the original and the shifted dislocations, the previously passed dislocation (black) was moved and pinned outside the continuum domain and a new “opposite” dipole dislocation (red) on the shifted slip plane was added. During unload, (c) the shifted (red) dislocation glided back into the atomistic and (d) eventually returned to the crack tip. In all slip plane shifting simulations, the distance of each shift is $1b$. The lengths given in this figure are normalized with respect to the burgers vector b , and the images are not drawn to scale.	51
4.1	Multiscale simulation setup with an atomistic domain embedded in a linear elastic continuum domain. The lengths given in this figure are normalized by the burgers vector magnitude, b , and the images are not drawn to scale. The continuum coloring represents the macroscopic displacement in the y direction, pad atoms are coloring in red, and atoms inside the atomistic region are colored according to their potential energy, highlighting the crack surface.	53

4.2	Atomistic domain and crack tip under static loading with dissolution. Only atoms with a centrosymmetry parameter not equal to that of the perfect hexagonal crystal are shown in the left figures, i.e. atoms at the crack surface, continuum-atomistic interface, and dislocation cores. Figures on the right show zoomed views of the crack with atoms colored by their energy, with the exception of the continuum region pad atoms that are shown in red. (a) Initial configuration at $K^* = 0.0$; (b) After application of load before atom removal ($K^* = 1.96$); (c) After removal of 20 atoms ($K^* = 1.96$); (d) After removal of 40 atoms ($K^* = 1.96$); (e) After removal of 2540 atoms ($K^* = 1.96$).	56
4.3	Crack growth and corresponding atomistic domain in cyclically loaded simulation with and without dissolution at $\Delta K^* = 1.62$. Only atoms with a centrosymmetry parameter not equal to that of the perfect hexagonal crystal are shown, i.e. atoms at the crack surface, continuum-atomistic interface, and dislocation cores. Inserts show zoomed view of the crack tip where atoms in the atomistic region are colored based on the coordination number. (a) Crack growth in x-direction as a function of simulation cycles; (b) Peak of the 71 st cycle ($K^* = 2.16$); (c) End of the 71 st cycle ($K^* = 0.54$); (d) Peak of the 72 nd cycle ($K^* = 2.16$); (e) End of the 72 nd cycle ($K^* = 0.54$).	58
4.4	Atomistic domain and crack tip in cyclic loading simulation ($\Delta K^* = 1.47$) with dissolution rate of 10 atoms/cycle. Only atoms with a centrosymmetry parameter not equal to that of the perfect hexagonal crystal are shown in the primary images, i.e. atoms at the crack surface, continuum-atomistic interface, and dislocation cores. Inset images give zoomed views with atoms colored by their energy. (a) Crack growth in x-direction as a function of loading cycles with (in red) and without (in grey) dissolution ; (b) Peak of the 83 rd cycle before dissolution; (c) Peak of the 83 rd cycle after dissolution; (d) Peak of the 84 th cycle before dissolution; (e) Peak of the 84 th cycle after dissolution; (f) Peak of the 85 th cycle before dissolution; (g) Peak of the 85 th cycle after dissolution.	60

4.5	Crack growth and opening for a range of loadings and dissolution rates. In (a) and (b) cyclically loaded simulations with dissolution of 10 atoms per cycle are compared to a corresponding set of simulations with no dissolution w.r.t. the number of loading cycles. These simulations are also compared to a corresponding set of statically loaded simulations w.r.t. the number of atoms removed due to dissolution. In (c) the dissolution enhanced crack growth and opening for the cyclically loaded simulations is shown to be independent of loading amplitude at 170 cycles. In (d) through (f), and (g) through (i) the effects of dissolution rate are shown for two cyclic loading amplitudes, i.e. $\Delta K^* = 2.21$ and $\Delta K^* = 1.47$ respectively. The units of the y-axes are normalized by b . In (f) and (i) the gray region represents a regime where increasing dissolution rate will increase crack blunting and the frequency by which arrested cracks are freed. In the gray region, crack arrest is not common so increasing the dissolution rate will only increase crack blunting. . . .	61
5.1	Computer models of the two components studied in this report: Mandava weeder rotor (left) and the Jang JP-1 push seeder roller (right). For scale, the square grid spacing represents 1cm.	71
5.2	The Jang JP-1 push seeder which was recommended by our partner in Pakistan. Zoomed images show the roller component that was studied in section 3 and printed using ME3DP thermoplastic.	73
5.3	The ME3DP printer used in this project - QIDI TECHNOLOGY 3DP-QDA16-01 Dual Extruder Desktop 3D Printer, bought in September, 2016.	76
5.4	Unit cost of the JP-1 seeder roller for different fabrication methods. Curves were plotted from equation 5.1 with parameters obtained by fitting the model to obtained quotes.	81
5.5	Sketch of the Mandava weeder developed by an Indian farmer. It is widely used due to its lighter weight. The zoomed view shows a 3D model of the rotor of the Mandava weeder which is the most geometrically complex part of the weeder. Drawings were provided by Earth Links, Inc.	82
5.6	Unit cost of the Mandava weeder rotor via different manufacturing methods.	89

CHAPTER 1

INTRODUCTION

1.1 Background Information

Designing an efficient, economical and reliable structure is the underlying principle of the structural engineering discipline across a broad range of applications such as buildings, watercraft, aircraft, industrial equipment, and nuclear plants. A successful design requires careful structural analysis, comprehensive cost analysis and also a thorough understanding of structural material behaviors. Incomplete knowledge of material properties, inaccurate modeling or prediction of structural performance, and deficiencies in many other aspects may lead to catastrophic structural failures. One kind of such failures, fatigue fracture, is of particular interest to this thesis. It is estimated that fatigue fracture is accountable for about 80% of all structural failures [3], with a total cost to the United States economy was \$119 billion in 1982, which equates to about 4% of that year's gross domestic product (GDP) [4].

In sea based aviation specifically, fatigue failure represents one of the primary structural failure modes. Despite its importance, the prediction of fatigue in complex marine environments has remained a substantial challenge, resulting in over-designed sea-based structures and conservative maintenance processes, and ultimately leading to increased ownership costs, decreased availability of existing aircraft, unexpected failures, and the sub-optimum performance of new designs across the fleet.

In order to address this issue, the acquisition of field and laboratory failure data, as well as a knowledge of how to use the data to predict the failure of deployed structures are necessary. Considering the complex nature of fatigue failure, these tasks present

a formidable challenge. Regarding the acquisition of data, fatigue tests are known to be time consuming, stochastic, and expensive. Additionally, the fatigue behaviour of a material can be highly dependent upon a vast number of variables such as component geometry, loading, humidity, and temperature histories. Thus, the fatigue phenomenon cannot be fully characterized through experimental testing. To build the connection between available data and the prediction of fatigue, a model that is consistent with the underlying mechanisms controlling the fatigue process must be established.

A great need of such a bridge motivated a sustained effort to develop fatigue crack growth models. While there has been significant advancement in this area, models continue to rely on tunable material separation (crack initiation and growth) rules as input, e.g. crystal plasticity [5–9] and discrete dislocation [10–14] models. Although these models shed light on fatigue crack behaviors on different levels, the establishment of a reliable prediction model must reply on a thorough understanding of the underlying physics behind these material separation processes. Considering the atomistic nature of such processes, it requires closer looks at the crack tip on the atomic scale to reveal the fundamental mechanisms that govern fatigue crack growth.

In this context, an atomistic modeling approach is alluring in that it can serve as a powerful probe to illuminate the atomic mechanisms. The theoretical atomistic methodology is advantageous in two ways. It not only allows monitoring of fatigue crack growth on the angstrom scale during each loading cycle in real time, which is unachievable in any experiments, but also enables studies of different parameters without the arduous time and abundant money required to set up and perform actual tests. When environment comes into play, where multiple factors can act simultaneously, e.g. material dissolution, oxide formation, and hydrogen embrittlement, atomistic modeling provides a means to study the atomic-scale environmentally assisted material separation

processes under the action of isolated mechanisms.

1.2 Thesis Statement

This dissertation consists of six individual chapters. The first chapter provides a brief discussion of the background and motivation of the research in investigating the underlying mechanisms of the fatigue crack growth, and the rationale behind the utilization of atomistic modeling tool to conduct related studies.

The second chapter reports some of the prior research efforts that lay the foundations for and ultimately lead to the work that has been submitted for publication. Eight topics are discussed in this chapter: (1) basic understandings of fatigue; (2) effect of temperature on fatigue crack growth; (3) material potential development; (4) isolating the atomistic simulation; (5) multiscale model development and verification; (6) multiscale simulation of fatigue crack behavior in materials with different intrinsic ductility; (7) multiscale simulation of fatigue crack behavior with annealing; (8) multiscale simulation of fatigue crack behavior under Mode I + II loading. The studies detailed in these sections along with many other not included research work are carried out with the common objective of understanding and illuminating the atomic mechanisms governing fatigue crack growth, and provide contexts and support for the findings presented in the following chapters.

The third chapter, entitled "Atomic mechanism of near threshold fatigue crack growth in vacuum", has been submitted for publication. I shared the co-first authorship with Mingjie Zhao on this paper. By harnessing a new implementation of a concurrent multiscale method and contemporary computational resources, we have been able to (1) assess the validity of long-hypothesized material separation mechanisms thought to con-

trol near threshold fatigue crack growth in vacuum, and (2) reconcile reports of crack growth in atomistic simulations at loading amplitudes below experimental crack growth thresholds. We find that sustained fatigue crack growth in vacuum requires emitted dislocations to change slip planes prior to their reabsorption into the crack on the opposite side of the loading cycle. This provides a mechanistic foundation to relate fatigue crack growth tendency to fundamental material properties, e.g. stacking fault energies and elastic moduli, opening the door for improved prognosis and the design of novel fatigue resistance alloys. The implementation of the concurrent multiscale methodology was done by me with the exception of the continuum discrete dislocation component which was implemented by Mingjie Zhao. High-cycle simulations involving no continuum discrete dislocations were conducted by me, while the other simulations involving continuum discrete dislocations were performed by Mingjie. A detailed discussion about our contributions in the development of this approach is presented in Section 2.5.

The fourth chapter, entitled "The Role of Dissolution on Crack Growth at the Atomic Scale", has been submitted for publication. It reports my recent work focusing on understanding the crack growth under the influence of material dissolution. The growth of cracks can be substantially influenced by the environment, and atomic modeling provides a means to isolate the action of individual mechanisms involved in such complex processes. Here, a newly implemented multiscale modeling approach is utilized to assess the role of material dissolution on crack growth. While dissolution is found to be capable of freeing arrested fatigue cracks, the crack tip is always blunted under both static and cyclic loading, suggesting that dissolution has an overall crack arresting effect. Despite observations of plasticity-induced-dissolution and dissolution-induced-plasticity that are consistent with macro-scale experiments, dissolution-induced-blunting is found to be independent of mechanical loading magnitude. This will simplify implementation of the dissolution-induced-blunting process into continuum crack growth models.

The fifth chapter, entitled "Assessment of Additive Manufacturing for Increasing Sustainability and Productivity of Smallholder Agriculture", is published in 3D Printing and Additive Manufacturing. Co-authors include Professor Erika Styger and Professor Derek Warner. Looking back at the big picture of the ultimate goal of structural engineering, this interdisciplinary work assesses the potential of additive manufacturing (AM) from perspectives of structural performance and cost efficiency. The study begins with the identification of the current obstacles encountered by smallholder farmers in the field. The potential of AM, and especially material extrusion 3D printing (ME3DP), to assist in overcoming the identified obstacles was assessed for two cases considering both local prototyping and low-volume production. A simplified cost model was used to compare to the cost of manufacturing both in the U.S. and locally in the field. The acquired data suggests that in specific cases current ME3DP technology can more rapidly provide functional parts, accelerating the design cycle and lowering cost by about a factor of 10 relative to local fabrication routes. In the case where mechanical performance is critical and dimensional precision and surface finish are not, wire arc metal additive manufacturing appears promising, but it is not as economical as fabrication by traditional means in the field. It should be noted at the end that a service work like this project applies scientific principles across the disciplines to solve actual problems in the field, which is key to keeping the scientific endeavor going strong.

The sixth chapter concludes the primary achievement of the studies presented in this thesis, and proposes some future work that would be worth investigating further or deeper utilizing our knowledge about the discovered mechanisms and the newly implemented modeling tool. The general objective is to gain a more thorough and extensive understanding of the fatigue crack growth and also connect with more realistic scenarios to reduce discrepancies between computational simulations and real-world fatigue phenomenon. Ultimately, we hope to bring new insights into the physical mechanisms that

control fatigue crack growth in real environments, and contribute to the improvement of prognosis and design of novel fatigue resistance alloys in the everyday world.

CHAPTER 2
RESEARCH CONTEXT

2.1 Basics of Fatigue

Fatigue is a failure mechanism of materials and structural components when subjected to loading that varies with time. One of the special characteristics about fatigue is that cracks can be initiated and propagate at stresses well below the ultimate tensile stress or even the yield stress of the material, yet still cause catastrophic failure.

The stress state at the tip of a crack is usually characterized by the stress intensity factor (SIF), K . This concept was developed by Irwin [15] following the investigations of Westergaard [16]. It is one of the most fundamental and useful parameters in the field of fracture mechanics. The magnitude of SIF depends on the sample geometry, size and location of the crack, magnitude and distribution of load, and thus can be described as

$$K = \sigma\beta\sqrt{\pi a}$$

where σ is the applied stress, a is the crack length, and β describes the relationship between gross geometrical features to the stress intensity factor. Experiments and simulations have demonstrated that fatigue crack propagation can be well described by two related parameters - stress intensity range, ΔK , and the load ratio, R .

$$\Delta K = K_{max} - K_{min}$$

$$R = K_{min}/K_{max}$$

The process of fatigue failure is a combination of crack initiation and the subsequent

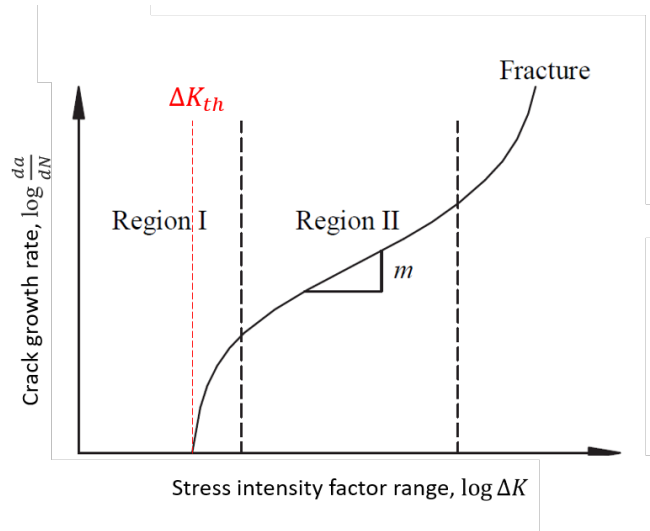


Figure 2.1: Three regions of the fatigue fracture process.

crack propagation, as shown in Figure 2.1. The initiation of a fatigue crack is considered to be closely related to localized plastic deformation during cyclic straining due to slip irreversibility [2, 17–19]. Once initiated, the propagation of the crack can be affected by so many variables such as the loading condition, material microstructure, and environment. Accordingly, the rates of crack growth have an extremely wide range from 10^{-9} to 10^{-1} mm/cycle [20]. Of the three regions shown in Figure 2.1, it is estimated that the crack initiation region, i.e. Region I, can take up to 90% of the fatigue life [21–23], which is governed by the fatigue crack growth near the threshold stress intensity factor, ΔK_{th} .

It has been reported that fatigue cracks can be initiated from surface defects or internal sites in the subsurface zone of materials. The subsurface fatigue cracks can grow at low stress amplitude levels that are below the conventional fatigue limits. While progression of technology has allowed researchers to directly observe and track fatigue crack growth in many subsurface materials, the mechanisms by which cracks grow remains elusive in some regimes. One prime example is the fatigue fracture behaviour in

vacuum near the threshold stress intensity range, ΔK_{th} , below which cracks remain dormant or propagate at experimentally undetectable rates (i.e. on the order of angstroms) [24–26]. Nonetheless, cracks with such show growth rates are still of considerable interest, since it can govern failures initiated from subsurface material defects and may lead to catastrophic failure over design lifetimes [27, 28].

Comparing with fatigue crack growth in vacuum, the presence of different environments such as moist air, sea water and corrosive liquids and gases can significantly change the associated characteristics. Adverse effects of the environment, predominantly from corrosive environments, contribute to the environment-assisted cracking. A corrosive media may both promote crack initiation and accelerate crack growth rate by orders of magnitude [29–31]. Despite a number of work has been conducted, there are still unknowns about the environmental effects on the fatigue crack growth. One of the challenges is the complex interactions between different factors that can act simultaneously on the fatigue crack, such as oxide formation, material dissolution, and hydrogen embrittlement [32–34]. These processes affect the fatigue crack growth by different mechanisms and thus require targeted and isolated studies.

Although the applied load on a crack can be arbitrary, any loading state could be decomposed into three independent stress intensity factors: (1) Mode I - opening mode, a tensile stress normal to the crack plane; (2) Mode II - sliding mode, a shear stress parallel to the crack plane and perpendicular to the crack front; and (3) Mode III - tearing mode, a shear stress parallel to both the crack plane and the crack front (as shown in Figure 2.2). A crack can be loaded in one mode exclusively, or it can be loaded in some combination of modes. In this thesis, the emphasis is focused on crack behaviors under pure Mode I loading, while effort has also been made to study the effect of mixed loading of Mode I and Mode II.

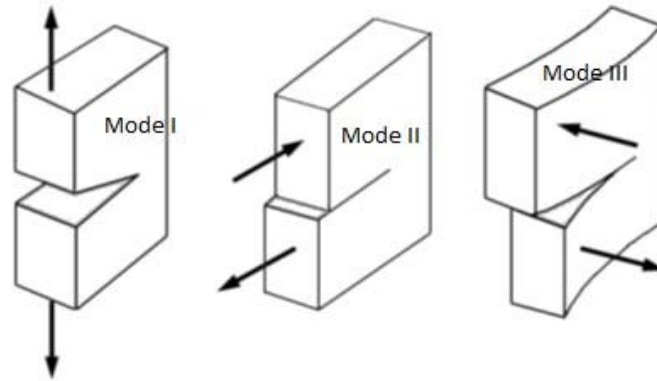


Figure 2.2: Schematic drawings of Mode I, Mode II and Mode III loading.

2.2 Effect of Temperature

The complexity of fatigue crack processes can be attributed to numerous parameters affecting the crack behavior at different levels and scales simultaneously. Thus, study of individual variable is a prerequisite for a thorough understanding of the fatigue cracking phenomenon. Among all the factors, the effect of temperature is of particular interest to us for two reasons. First, temperature plays an important role in the specific area of sea based aviation. Aircraft can experience a temperature difference as large as about 80 degrees Celsius from taking-off to landing. Thus, from a practical point of view, the effect of temperature must be taken into consideration in the analysis and prediction of fatigue crack behavior in aircraft. Second, temperature is also an important parameter in the determination of computational simulation setup. A change in temperature setting could lead to distinct results and thus bias our understanding of the governing mechanisms. Additionally, studying fatigue crack growth dependency on temperature can also help us interpret simulation results and/or any discrepancy observed between modeling and experiments.

A look at the literature focusing on fatigue crack growth in metal materials reveals that material resistance to near threshold fatigue crack growth increases with decreasing

temperature in ambient or humid environment. Liaw and Logsdon reviewed the near threshold fatigue crack propagation behaviors of five materials including aluminum, copper, steel, nickel and titanium alloys with temperature ranging from 297 K to 4.2 K [35]. Results showed that decreasing the temperature generally increased the value of the threshold stress intensity range, ΔK_{th} , in the five alloy systems investigated, while also decreased the rates of near threshold fatigue crack propagation. Similar findings in other materials have also been reported in many other literature [31, 36–41]. There is evidence showing that decrease in temperature impedes the environmental fatigue process primarily by retarding the hydrogen environment embrittlement process that is considered as the governing mechanism of environment assisted crack growth [42, 43].

Under vacuum or inert environment, on the contrast, a substantial amount of experimental and modeling investigations demonstrate a weak influence of temperature on fatigue crack propagation and the associated crack tip plasticity at the microstructure scale [44–49]. For instance, Cotterill and Knott [45] conducted a set of experiments to study fatigue crack growth in a steel material at elevated temperatures ranging from 298 K up to 898 K. Researchers reported that in vacuum, the fatigue crack growth rates are practically independent of temperature over the whole range of temperatures tested. Results from atomistic modeling of cracks in single crystal copper at 77 K, 300 K, and 600 K [50] reconciled the experimental observation, showing no dependence of crack growth on temperature. It was also concluded that temperature does not change the mechanisms of plastic deformation around the crack tip, as similar dislocation structures were found at all examined temperatures. Moreover, the dislocation density and the vacancy concentration are found to be only slightly influenced by temperature without a general trend. While there is a slight decrease noticed in the SIF required for dislocation emission from the crack tip as temperature raises, such correlation is driven by the change in elasticity constants and unstable stacking fault energy [51], which does

not contradict the statement about the temperature independence of plastic deformation mechanisms at the crack tip.

The finding of the weak influence of temperature on crack growth rates and crack tip plasticity in vacuum provides justification for the athermal setting of the simulations conducted in this thesis, which serves as one of the necessary conditions to make high cycle count simulations computationally tractable. It also inspires the study of fatigue crack growth with annealing by implementing the process of annealing into the loading cycle in order to explore the effect of the microstructural change, and more specifically dislocation reactions, induced by elevation of the temperature. Details are discussed in Section 2.7.

2.3 Material Potential Development

It has been discussed previously that atomistic modeling can serve as a powerful probe to study the near threshold fatigue crack growth considering its atomic nature. Although atomistic modeling has progressed substantially over the past decades, its application to fatigue crack growth has remained very limited due to significant obstacles. One of the most challenging problems is the choice of the interatomic potential, as computation of atomic forces involves a trade-off between accuracy and computational expense. Modern electronic structure methods can provide the desired accuracy for many chemically complex systems, while the associated computational cost limits these methods to systems of only a few hundred atoms. Alternatively, traditional empirical potential methods can be used to simulate billions of atoms, but they often struggle to reproduce behaviors outside of what they were fit. Thus, to choose an appropriate interatomic potential with adequate accuracy and acceptable computational expense that can best describe the

targeted system of interest is one of the most important tasks for atomistic modeling.

In previous work, we used the coupled atomistic and discrete dislocation (CADD) model and the aluminum potential from Ercolessi and Adams [52] in the atomistic region, which accurately modeled pure Al crack tip behavior under many conditions in literature [34, 53, 54]. However, the single slip plane of the simulated 2D aluminum system with the most favorable orientation made it a challenge to interpret these results relative to corresponding experiments, suggesting the limitation of this potential associated with our specific research interest. To address this issue, we determined to create an atomistic domain composed of 2D hexagonal lattices that offers 3 different slip planes, and utilize an interatomic pair potential with tunable intrinsic ductility [1].

This potential considering only nearest-neighbour pairwise interactions is characterized by the energy function $\phi(r)$, where r is the distance between atom centers. The intrinsic ductility of the potential can be tuned by altering the tail of $\phi(r)$ while leaving the energy well unchanged to ensure that near-equilibrium properties of the material, such as the elastic constants, remain constant. The specific form of the potential can be written as

$$\varphi(r) = \begin{cases} (1 - \exp[-\alpha(r - 1)])^2 - 1, & r \leq r_1 \\ A_1 r^3 + B_1 r^2 + C_1 r + D_1, & r_1 < r \leq r_2 \\ A_2 r^3 + B_2 r^2 + C_2 r + D_2, & r_2 < r \leq r_3 \\ 0, & r_3 < r \end{cases} \quad (2.1)$$

where the distances (r_1, r_2, r_3) , and the cubic spline coefficients (A_1, B_1, \dots, D_2) can be determined under various conditions to describe materials with different ductility. Applying this potential to a 2D hexagonal lattice system, a number of materials with increased ductility can be described as plotted in Figure 2.3.

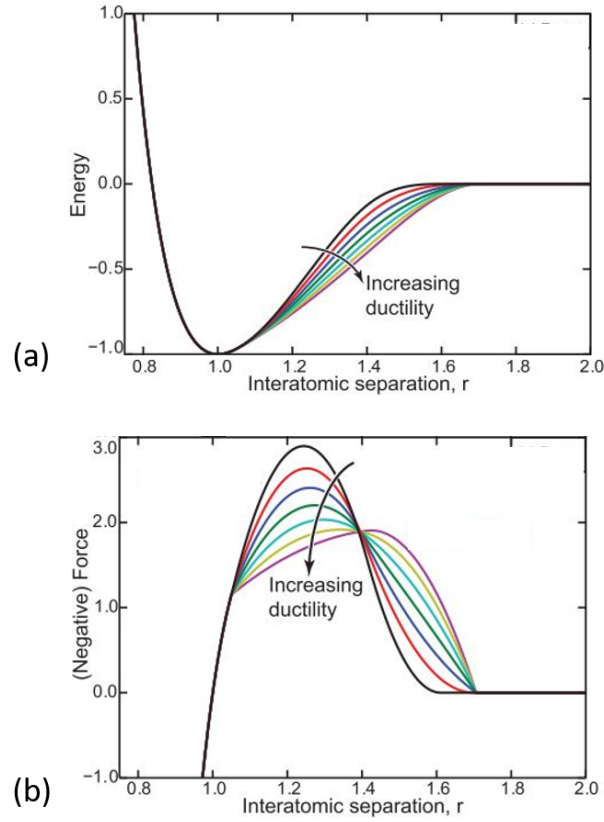


Figure 2.3: Interatomic potentials with tunable intrinsic ductility in 2D. (a) Energy; and (b) Force vs interatomic separation distance. Units are normalized (source [1]).

The study began by reproducing these potentials to fit our model. As a tabulated potential file is required for the atomistic simulation, different numbers of the interpreting points with different increments of the interatomic distance were examined in order to optimize the computational performance without sacrificing the accuracy. Two sets of fatigue crack simulations with materials of different intrinsic ductility (Potential A and Potential C) were then performed under a range of mechanical loadings (details are discussed in Section 2.6) to compare the outcomes. To simulate an alloy-like material, the most ductile potential in this family (i.e. Potential A) was modified so that the new potential has a 4 times deeper energy well but the same lattice and elastic constant (see Figure 2.4). Alloy-like simulations were performed with 5% of atoms in the atomistic

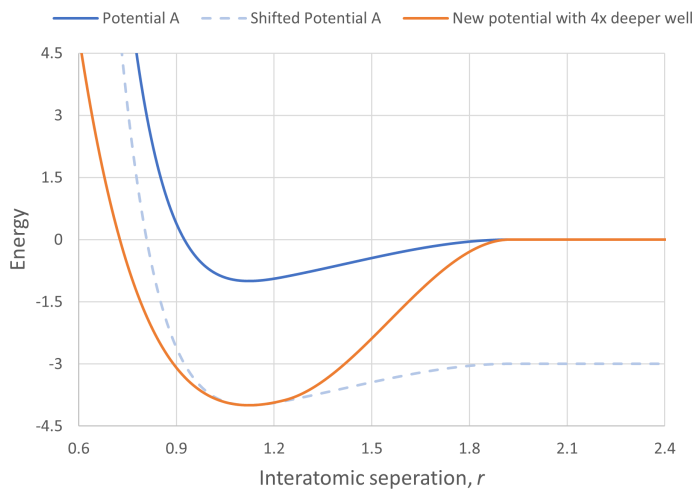


Figure 2.4: Energy vs interatomic separation of Potential A and new potential with 4 times deeper energy well. Units are normalized. Curve of Potential A is shifted downwards for better comparison.

box having the deeper well energy potential and the rest atoms described by Potential A. These solute atoms inside the domain acted as localized barriers to dislocation motions. While the barrier strength, i.e. flow strength, was not quantified, it was apparent that strengthening due to such solute atoms was significant, leading to two limiting cases of material for us to move forward with, i.e. brittle vs ductile.

To further understand the fatigue crack growth mechanisms and to relate fatigue crack growth tendency to fundamental material properties, recently we modified the original potentials to characterize materials with higher surface energies by extending the interactions to the second-nearest neighbors and superimposing a tuned embedded atom method (EAM) potential on it. The original Potential A is the most ductile material potential that can be achieved under the constraint of considering only nearest-neighbor pairwise interactions, yet there is still disconnection between it and real metal materials [55]. By extending this potential to include the next nearest neighbor interactions (Figure 2.5), we were able to improve the intrinsic ductility of the current potential by mitigating this discrepancy. Built on the extended potential, an addition of an embedding

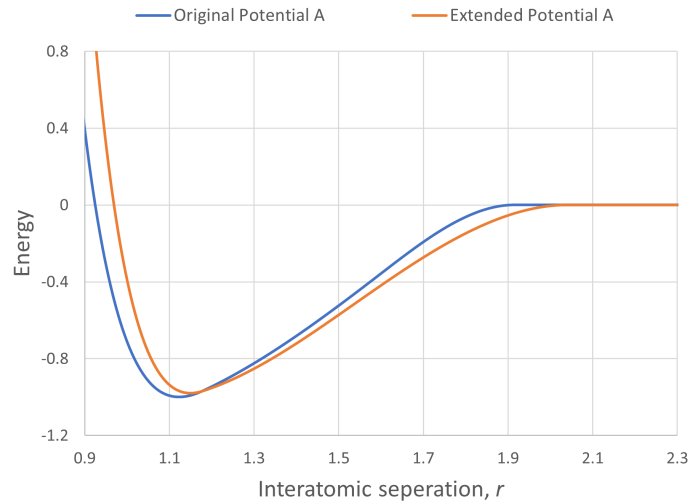


Figure 2.5: Energy vs interatomic separation of original Potential A and the extended Potential A with next nearest neighbor interactions included. Units are normalized. The two potentials have the same properties. Different numbers of counted bonds and different equilibrium atomic spacing lead to shifting of the energy curve.

energy can increase the surface energy of the potential, enabling the study of isolated effect of surface energy. The new superpositioned energy, shown in Figure 2.6, has a higher surface energy compared with Potential A with all the other properties, such as the lattice spacing, elastic constant and stacking fault energy, being held constant. Similar method was applied to Potential C where the same EAM energy was added on the original Potential C. The added EAM energy was tuned so that the ratio between the surface energy of the original potentials and the new potentials is the same as the ratio between the unstable stacking fault energy of original Potential A and Potential C.

Based on our current understanding of the fatigue crack growth, simulation results with the new potentials that have higher surface energies are expected to be similar to the results with original potentials, because the surface energy is considered as a less controlling parameter during the crack growth processes. For testification, the critical stress intensity factor when the first dislocation emits from the crack tip under Mode I loading, K_{Ie} , was tested for new and original potentials under both sharp and blunt crack

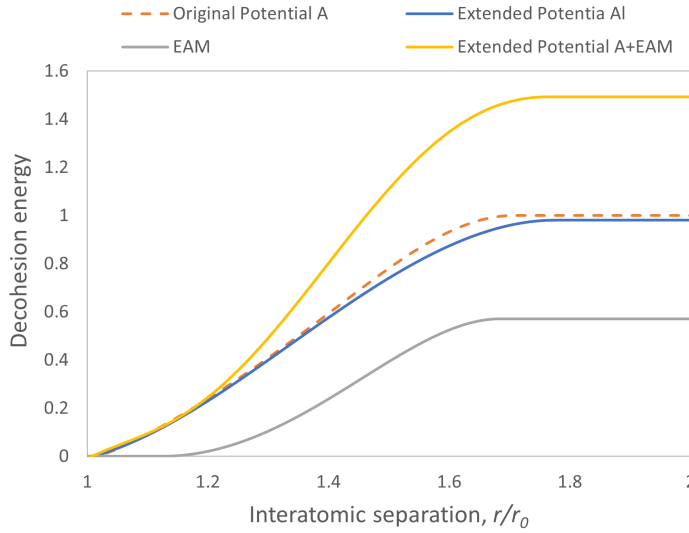


Figure 2.6: Decohesion energy vs nominated interatomic separation (by equilibrium atomic spacing) from Potential A, extended Potential A, EAM potential and the new potential by superposition. Units are normalized.

tip conditions. The comparison shows similar results for modified and original Potential C, but the crack behavior with modified Potential A seem to differ from that with the original potential, i.e. increase in the surface energy changes the dislocation nucleation activity significantly. Multiscale fatigue loading simulations with new potentials were also conducted, and preliminary results show distinct differences in the crack growth behavior when compared with the original results. Although application of the potentials and interpretation of the current results may need further investigation, the development process of these potentials is still valuable for future studies.

2.4 Isolating the Atomistic Simulation

It is acknowledged that material separation process at the crack tip under fatigue loading is complicated, as it involves intensive dislocation activities such as dislocation nucleation, glide, interaction, absorption, and annihilation. Due to the spacial and time scale

limit, observations of these activities are not easily accessible by experimental means. Atomistic simulation techniques, such as molecular dynamics (MD), are promising and can provide new opportunities and perspectives for studying and understanding crack tip processes occurring at the atomic scale, which governs the behaviors of materials and structures on larger scales.

Inspired by crack tip behaviors previously simulated using the CADD modeling, and the lack of sustained crack growth observed in all simulations performed by then, a set of purely atomistic simulations isolated from the multiscale framework were performed using an open source MD software, Large-scale Atomic/Molecular Massively Parallel Simulator (LAMMPS) [56]. The aim of this study was to test the contribution of dislocation motion to the crack growth in a simple setting. A purely atomistic specimen composed of 2D hexagonal lattices was created with Potential A [1] offering 3 different slip planes. Edge dislocations were continually inserted into the system at random locations and with random orientations followed by mechanical relaxation of the atomistic domain. Systems with and without preexisting crack were explored under conditions with and without static loading. Another set of simulations were performed with 5% of atoms serving as solute atoms with modified potential A (as detailed in Section 2.3). These solute atoms provided localized barriers to dislocation motion, and thus allowed for us to simulate an alloy-like material in a simple way.

In an unloaded material without preexisting crack, the inserted dislocations quickly exit the material to reduce strain energy during mechanical relaxation. One might expect this to eventually lead to no net change, or at most an evolution to a hexagonal or circular shape in order to reduce surface energy. For no-crack specimen under tensile load, the motion of the inserted dislocations would be biased and may lead to plastic deformation of the material. Simulation results are consistent with this hypothesis. Re-

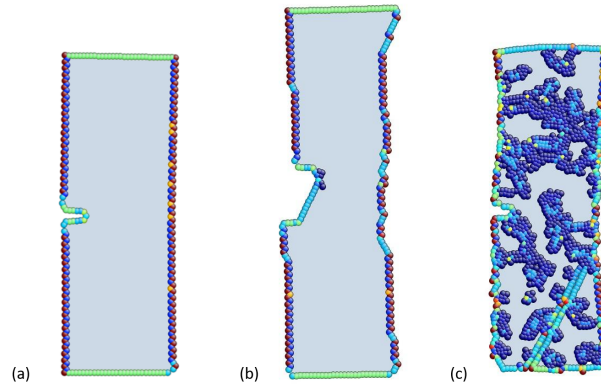


Figure 2.7: Specimens under static Mode-I loading showing only atoms with a centrosymmetry parameter not equal to that of the perfect hexagonal crystal, i.e. atoms at the crack surface, boundaries, clusters around alloy atoms, and dislocation cores. (a) Potential A simulation with no dislocation insertion; (b) Potential A simulation after 38 dislocations inserted; (c) Potential A simulation with solute atoms after 38 dislocations inserted. Insertion of dislocations is shown to promote the plastic deformation and crack growth.

garding cases with preexisting cracks, arrested cracks under static loading are observed to grow with random insertion of dislocations in both the ductile and brittle materials as seen in Figure 2.7. Under the same static loading condition and at the same loading step, specimens with random dislocation insertion experience larger deformation and crack growth than the reference simulation with no dislocation inserted. The deformation in the ductile material is more significant compared with that in the alloy-like material, which is reasonable considering atoms with deeper energy well functioning as barriers to the motion of inserted dislocations. Different domain sizes of the simulation were also tested and found to not affect the conclusion.

Despite the simple setting, results from these early atomistic simulations clearly demonstrate the irreplaceable role of dislocation activities in the crack growth process, suggesting dislocation emitted from sources away from the crack tip might be key to sustained fatigue crack growth. These findings along with other work motivated the development of the multiscale modeling tool in order to perform more comprehensive

investigations of fatigue crack growth in vacuum, and laid foundation for the discovery of the mechanism presented in Chapter 3.

2.5 Multiscale Model Development and Verification

Although atomistic modeling allows the examination of fatigue crack growth at the atomic scale, limitations of purely atomistic simulation do exist that hinder the capability of such models to fully capture true fatigue crack growth in real alloys. One of the largest challenges is the limited spacial domain which could ultimately lead to bias in crack tip behavior. To resolve the shortcomings of traditional atomistic simulations, multiscale modeling has been developed to accommodate a much larger spacial domain while still focusing on exploring the atomic-scale mechanisms occurring at the crack tip [57–63]. The CADD model, in particular, offered a unique solution to this problem and has been used to study fatigue crack growth in many literature [34, 54, 61, 62].

The CADD model consists of an atomistic region and a continuum region coupled by self-consistent displacement boundary conditions. An edge crack is created by removing multiple layers of atoms. The atomistic region around the crack tip allows the simulation to capture the atomic nature of crack tip process, and the continuum region outside the atomistic region accommodates a much larger spatial domain to mitigate the artificial influence on the dislocation movement due to small spatial domain. The two regions are coupled together by interface nodes and pad atoms. Displacements of the interface nodes computed from the atomistic simulation serve as part of the boundary conditions for the finite element analysis of the continuum region; results from finite element analysis are passed to the pad atoms which are then fixed during the following atomistic simulation. While previous work utilizing this model successfully addressed their re-

search questions, our attempts with CADD at the beginning of the project exposed some limitations of the model in regards to our specific research objectives, i.e. unrealistic crack tip behaviors were observed and no sustained crack growth was achieved in all simulations.

Specific issues that restricted further adoption of the CADD model include small loading range that can be successfully applied to the simulation system, and single slip plane presented in the examined crystal orientations, which may constrain the growth of the crack. To overcome these limitations, and also motivated by previous atomistic simulations results, we implemented a new version of the multiscale modeling tool built upon the concept of CADD. In specific, we built a framework to utilize highly efficient open source software LAMMPS [56] to conduct the molecular static simulation for the atomistic region, and a popular open-source computing platform named FEniCS [64] for the finite element analysis of the continuum region. This method is thus referred to as LF-CADD. The atomistic simulation box is composed of 2D hexagonal lattices with 3 different slip planes and a simple ductile interatomic potential with only nearest-neighbour pairwise interactions considered was utilized [1]. The integration of the two powerful packages enables us to simulate fatigue crack growth with large amount of dislocation motion to high cycle counts.

Development of the code was done in collaboration with Mingjie Zhao, another student from the group. My contribution to this work started by the creation of the overall framework in Python to accommodate successful operations of LAMMPS and FEniCS and smooth communications between the two software. This model was then improved to take advantage of parallel computing, enabling more efficient simulations. A number of ancillary functions were created to assist in the operation of the model and succeeding data processing. For the sake of computational cost, non-uniform mesh for

the continuum region was predefined with more precise elements around the atomistic region and coarser ones near the outer boundary. Atoms in the atomistic region were also produced and labeled prior to the beginning of the simulation in order to guarantee accurate data transferring during parallel computing and communications between the two regions. Crack tip tracking function is another example of the ancillary functions that is created to fulfill the tractability of the fatigue crack growth simulations in real time and for easier post-processing. The implementation of the discrete dislocation (DD) algorithm was completed by Mingjie Zhao, which allows dislocations emitted from the atomistic region to be passed into the continuum region, and activated dislocations from sources in the continuum region to be passes into the atomistic region.

Convergence studies were conducted afterwards to ensure the accuracy and efficiency of the model. Such studies included testing of the loading increment magnitude, potential interpreting points and so on. To optimize the utilization of computational resources, simulation running time as a function of the number of CPU cores used was also examined to make sure an optimized number of simulations can be conducted simultaneously and also complete in a timely manner.

Analytical and numerical solutions of the displacement field and stress field were analyzed and compared for the verification of the coupling of LAMMPS and FEniCS. As loads in this model are applied by prescribed displacements at the outer boundary of the continuum region based on given stress intensity factors at the crack tip, the first verification involved comparing the modeling displacement field to the analytic sharp crack asymptotic solution. Nodes on the interface, outer boundary and from the inner continuum region were selected for inspection. Results are shown in Table 2.1. The second verification involved a ramped loading simulation to assess the critical stress intensity factor at which the first dislocation nucleates from the crack tip. The observed

Table 2.1: Results of code verification of the displacement field. Units are normalized. The remaining error (which is deemed acceptable) is due to the analytic solution not accounting for the actual shape of the crack tip, and the linear shape functions used in the finite element analysis in the continuum domain.

$K_I = 0.0001$		ux			uy		
		Analytic	FEniCS	Error	Analytic	FEniCS	Error
Interface nodes	#1	2.014E-05	1.630E-05	-19.06%	-4.093E-05	-4.321E-05	5.58%
	#9	1.900E-05	1.674E-05	-11.86%	-9.349E-06	-1.013E-05	8.35%
	#21	1.900E-05	1.675E-05	-11.81%	9.349E-06	1.015E-05	8.60%
	#29	2.014E-05	1.632E-05	-19.00%	4.093E-05	4.325E-05	5.67%
Inner Continuum nodes	#233	2.086E-05	1.925E-05	-7.71%	-8.237E-05	-8.315E-05	0.94%
	#257	2.252E-05	2.122E-05	-5.79%	-6.035E-06	-5.786E-06	-4.14%
	#358	2.713E-05	2.641E-05	-2.68%	8.038E-06	7.799E-06	-2.98%
	#359	2.751E-05	2.621E-05	-4.76%	8.187E-05	8.267E-05	0.98%
	#517	4.541E-05	4.527E-05	-0.31%	-4.541E-05	-4.564E-05	0.50%
Outer boundary nodes	#643	4.541E-05	4.529E-05	-0.26%	4.541E-05	4.568E-05	0.60%
	#420	4.694E-05	4.694E-05	0.00%	-1.154E-04	-1.154E-04	0.00%
	#436	4.604E-05	4.604E-05	0.00%	-1.872E-05	-1.872E-05	0.00%
	#454	4.604E-05	4.604E-05	0.00%	1.872E-05	1.872E-05	0.00%
	#470	4.694E-05	4.694E-05	0.00%	1.154E-04	1.154E-04	0.00%

value was very close to Rice’s analytic solution of crack tip dislocation nucleation [55].

The LF-CADD code was also verified for discrete dislocation capabilities by Mingjie Zhao. Specifically, a simulation was performed that involved (1) a dislocation nucleating from the crack tip and gliding to the edge of the atomistic domain, (2) being passed from the atomistic domain to the continuum domain, and (3) moving within the continuum domain. The force on passed dislocation in the continuum domain was compared to the analytic sharp crack asymptotic solution, noting that computing this force correctly requires all aspects of the code to function properly due to the elastic interaction between the dislocation and the crack.

It should be noted that for subsequent multiscale modeling work presented in this chapter and Chapter 4, the concurrent multiscale approach was utilized without the implementation of the DD algorithm. Early investigation on the role of dislocation glide resistance in the continuum domain shows that while greater glide resistances reduce the plastic zone size in front of the crack tip, fatigue crack growth is observed to be independent of this parameter. This result is consistent with the conclusion of discrete dis-

location continuum modeling [65, 66] and experiments [28, 66–71]. The result provides validity for subsequently presented simulations in this chapter and Chapter 4 where dislocation motion was constrained to the atomistic domain without the help of the DD algorithm (effectively imposing a high glide resistance) in order to access high cycle counts.

2.6 Multiscale simulation of fatigue crack behavior in materials with different intrinsic ductility

By harnessing the novel implementation of the concurrently coupled atomistic - discrete dislocation approach detailed in the above section and contemporary computational resources, we are able to perform a number of fatigue crack simulations under different conditions to high cycle counts. Considering the generality existed in the fatigue fracture across different materials, here we focused on two potentials with tunable intrinsic ductility, which enables the general principles of material deformation and fracture to be elucidated without confining attention to a particular material system.

Intrinsic ductility of a material describes the competition between the brittle and ductile modes of deformation in a material with a crack, which can be characterized by the energy required for Griffith cleavage, G_{Ic} , and energy required for dislocation emission from the crack tip, G_{Ie} [72]. The two investigated potentials here - Potential A and Potential C as mentioned in Section 2.3 - have tuned G_{Ie} that is independent of G_{Ic} . Preliminary simulations with monotonic loading show that the critical stress intensity factor for nucleation of the first dislocation from the crack tip, K_{nuc} , is 6.8 for Potential A, and 8.4 for Potential C. For fatigue crack simulations, a range of cyclic mechanical loadings with load ratio $R = 0.25$ were applied, and the load increment after

each mechanical equilibration was 0.1. The effect of atomistic window size were also studied for Potential A. Simulations were carried out in the athermal limit to hundreds of cycles.

Here the results of fatigue crack simulations under a wide range of cyclic mechanical loading with Potential A are presented in Figure 2.8. Crack arrest is observed in many cases. The arrest of cracks is due to dislocation activities including emission and absorption being completely reversible during the loading and unloading processes. In simulations with larger loads (i.e. $\Delta K > 17$), sustained crack growth is shown in some cases throughout the duration of the simulations, where dislocation activities remain irreversible over the course of individual loading cycles. Interestingly there are some instances where dislocation activity appears reversible for 10's of loading cycles but then suddenly becomes irreversible again, spurring fatigue crack propagation. Effect of different domain sizes is not observed to be significant. To better understand the behavior in the $\Delta K > 17$ loading regime, a number of phenomena were examined, e.g. anti-shielding dislocation creation and annihilation, dislocation annihilation on slip planes that do not intersect the crack tip, dislocation-dislocation reactions, dislocation crossing of the crack plane, dislocation creation on unloading, dislocation density over the course of the loading cycle, crack tip opening distance, and crack tip opening angle. Sustained crack growth occurred in these simulations is found to require:

- The creation of dislocations on planes that do not intersect the crack during the loading part of the cycle;
- The emission of anti-shielding dislocations during the unloading part of the cycle;
- Dislocation reactions.

Examination of these dislocation activity and the preliminary findings inspired the subsequent more targeted simulations using the LF-CADD model with the implemented

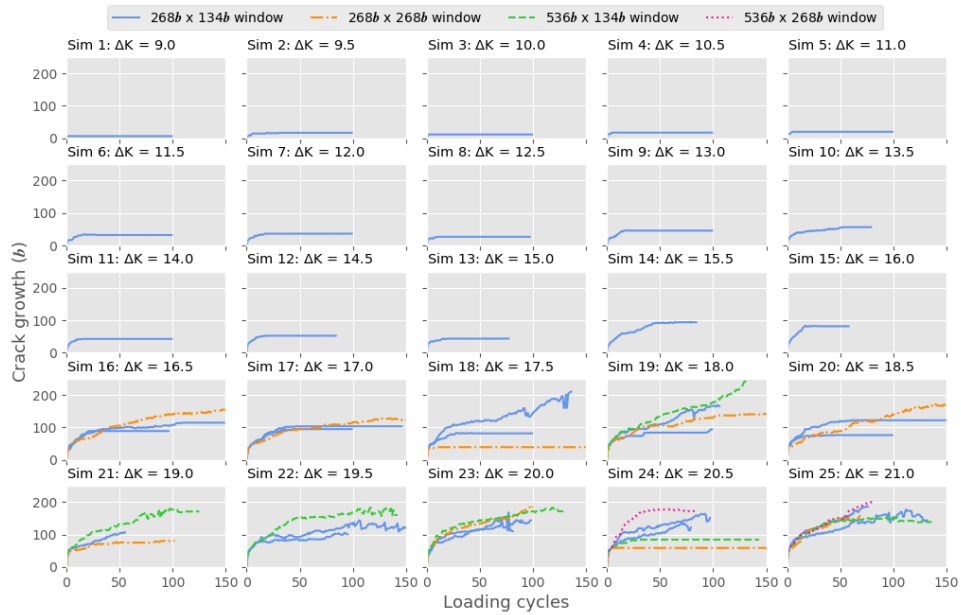


Figure 2.8: Plots of crack growth vs loading cycles from hexagonal lattice simulations for a range of atomistic window sizes with Potential A. Curves in different colors represent results from simulations with different atomistic domain sizes. The applied stress intensity range, ΔK , varies from 9.0 to 21.0. Cracks arrest at lower loads, and tend to grow as load increases. The effect of window size is shown to be not significant.

DD algorithm, and led to the reveal of the atomic mechanism governing sustained fatigue crack growth in vacuum, which is presented in Chapter 3.

With Potential C applied, cracks shows distinct behaviors under similar mechanical loadings. As no significant effect of atomistic window size on fatigue crack growth is found, the size of the atomistic region for simulations with Potential C was adjusted to accommodate potential cleavage fracture due to the more brittle material property. Results are presented in Figure 2.9. It can be noticed that cracks arrest much faster in these simulations compared with results with Potential A, generally within the first 10 cycles. No sustained crack growth is achieved under the tested loading conditions. Burst of crack growth is observed in 2 of the 25 simulations in the manner of cleavage, where crack propagation occurs through planar sectioning of the atomic bonds between atoms at the crack tip during the loading process. Under higher loads, crack closure appears

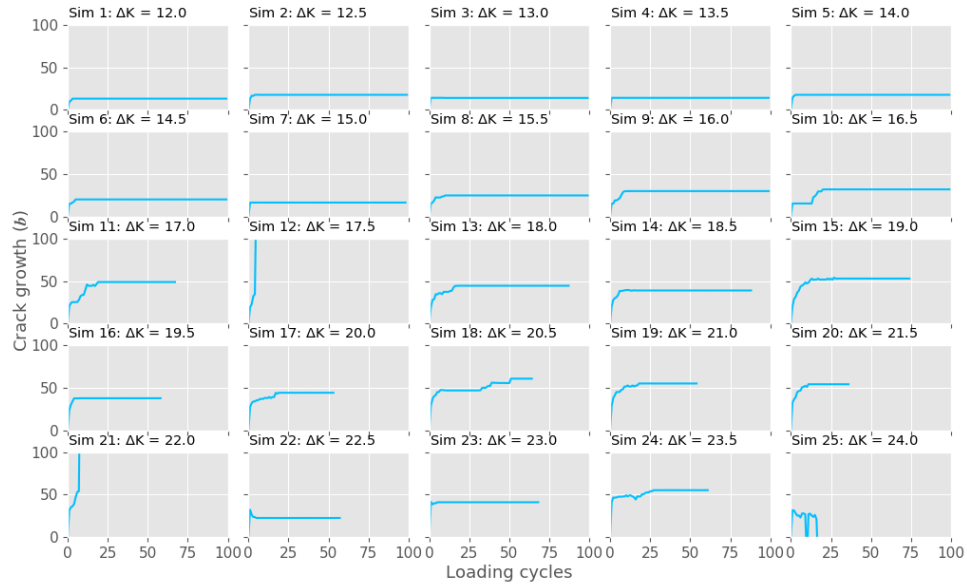


Figure 2.9: Plots of crack growth vs loading cycles from hexagonal lattice simulations with Potential C. The applied stress intensity range, ΔK , varies from 12.0 to 24.0. The size of the atomistic window is $[357 b \times 87 b]$. Crack arrest, cleavage and closure are observed.

due to the formation of artificial defect from dislocation pile-up.

Arrest of cracks after an initial transient period observed in both sets of simulations reconciles the standing discrepancy between model and experiment, whereby reports of crack growth in atomistic simulations occurs at loading amplitudes well below the corresponding experimentally thresholds for fatigue crack growth in vacuum [73]. Comparison between the two sets of results demonstrates different behaviors of fatigue cracks in materials with different ductility, implying different mechanisms governing the material separation processes at the crack tip in ductile and brittle materials. For subsequent studies of fatigue crack simulations in this thesis, Potential A was used to investigate the mechanisms of fatigue crack growth in ductile metal materials. It should be emphasized that the most primary results associated with these simulations are presented in Chapter 3. The discussion above aims at providing more context of the work that is essential for the arrival of the published work.

2.7 Multiscale simulation of fatigue crack behavior with annealing

The current setting of the fatigue crack simulation with a 2D hexagonal lattice and the intrinsically ductile interatomic potential offers three dislocation slip systems and glissile dislocation reaction, providing a beneficial environment for dislocation motion and interaction that accompany the growth of crack. Preliminary finding presented in Section 2.6 indicates the important role of dislocation reactions in facilitating sustained crack growth, which inspired us to further examine it by introducing annealing at certain step of the loading cycle. Additionally, dislocation pile-up might lead to defect formation inside the atomistic region (see Figure 2.10 for an example). Such defect could have artificial influence and thus impede the growth of crack in an unnatural way. The addition of annealing may help solve the issue by inducing redistribution of atoms at the elevated temperature.

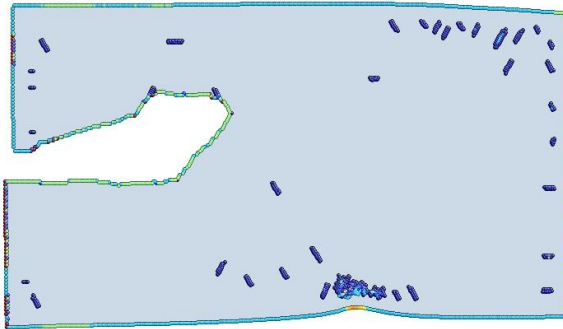


Figure 2.10: Atomistic domain in cyclic loading simulation with Potential A ($\Delta K = 19.5$). Only atoms with a centrosymmetry parameter not equal to that of the perfect hexagonal crystal are shown in the left figures, i.e. atoms at the crack surface, continuum-atomistic interface, and dislocation cores. An artificial defect is formed near the bottom interface due to dislocation pile-up.

The annealing process consisted of heating the atomistic region to half of the melting temperature over 100,000 time steps and then cooling back to zero temperature over

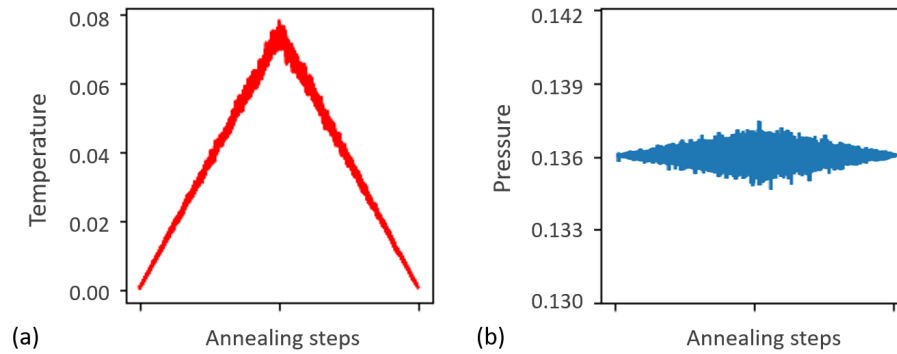


Figure 2.11: Plots of (a) temperature, and (b) pressure of the system during the annealing process. Units are normalized. Pressure of the system was maintained throughout the process.

100,000 time steps. To avoid complicating artifacts, the total pressure of the system was maintained during this thermal treatment 2.11. Two sets of 2D hexagonal lattice simulations with Potential A were conducted with annealing added at the peak and bottom of each loading cycle respectively (i.e. at K_{max} or K_{min}).

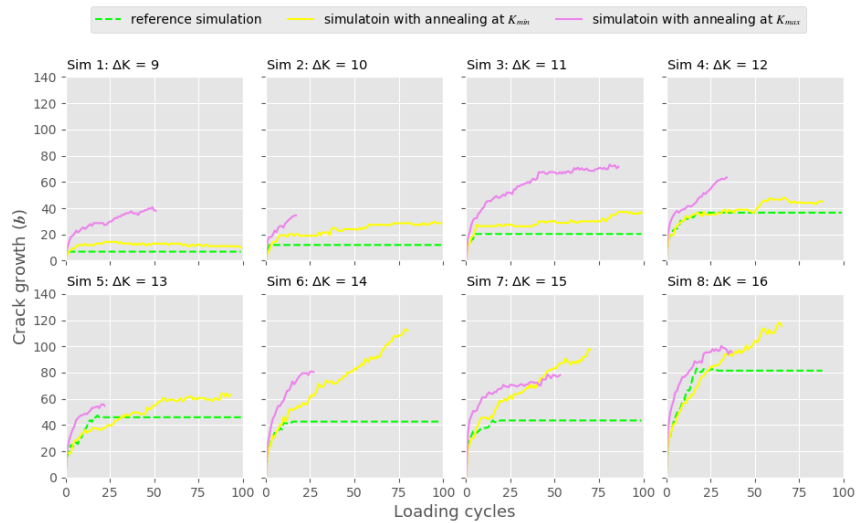


Figure 2.12: Plots of crack growth vs loading cycles from ductile hexagonal lattice simulations with annealing introduced at different steps of each loading cycle. The applied stress intensity range, ΔK , varies from 9.0 to 16.0. Annealing is shown to promote crack growth.

The intent of the annealing treatment is to facilitate more dislocation reactions. Results of the annealing simulations are presented in Figure 2.12 along with the reference simulations without annealing. There is a general trend observed that the annealing process promotes crack growth no matter where it occurs, and annealing at the peak of the loading cycle has a greater impact on the progression of the crack tip. By comparing the atomistic domain around the crack tip before and after annealing, it is suggested that the density of dislocations and the shape of the crack tip for the specific load are not substantially changed by the annealing process; and thus, it is solely the boost of dislocation reactions that facilitates the enhanced crack growth. The more prominent effect of annealing at the peak of the loading cycle could be attributed to higher dislocation density under a larger load of the cycle, which offers more opportunities for dislocation reactions that lead to sustained crack growth.

It must be reemphasized that studies like this guide our understanding of the fatigue crack behaviors and possible underlying mechanisms from different perspectives. It is the accumulation of the work discussed here along with those in other sections that lays the foundation for and finally leads to the primary thesis results presented in Chapter 3 and Chapter 4.

2.8 Multiscale simulation of fatigue crack behavior under Mode I + II loading

Structural components in real life are often subjected to variable, multi-axial loading during the service life. To understand the fatigue crack propagation in practical loading conditions, analytical and experimental studies have been conducted under one, or any combination, of the three loading modes [74–79]. Since cracks may change growth

direction when subjected to mixed-mode loading conditions, emphasises of these studies have been placed on not only the crack growth rate measurement but also the crack growth path prediction. However, it remains a challenge for experimental researchers to understand mixed-mode crack tip behaviors, as the complexity of the loading condition makes it hard to analyze the mode mixity and the associated stress intensity factor components through only direct observations. In light of the challenges, the new implementation of the concurrent multiscale approach can serve as a probe to understand more about the progression of crack under mixed-mode loading conditions.

Here a set of 2D hexagonal lattice simulations with Potential A were performed under loading of mixed modes I + II. Mixed-mode loads in the simulation were applied at the outer boundary of the continuum region by the superposition of prescribed displacements based on given stress intensity factors in different modes, K_I and K_{II} . A range of loads (i.e. ΔK) were tested, where the magnitudes of the two stress intensity factors in different modes were kept the same at each loading step (i.e. $K_I = K_{II}$).

Results are presented in Figure 2.13 with comparison between the crack growth in length under pure Mode-I and mixed-mode I+II loading, as well as the change in opening and offset between two crack surfaces under the mixed-mode loading. Arrested cracks in the reversible state are observed when the applied mixed-mode loads are small, yet the overall crack growth still increases when compared with pure mode I loading results. Nonetheless, under higher loads (i.e. $\Delta K > 10.5$), there is a significant increase in crack opening distance between crack surfaces along with a decrease in crack length as loading cycle proceeds.

Taking closer looks at the atomistic domain, Figure 2.14 presents the progression of the crack when subjected to a high load of $\Delta K = 11.5$. The shape of the crack

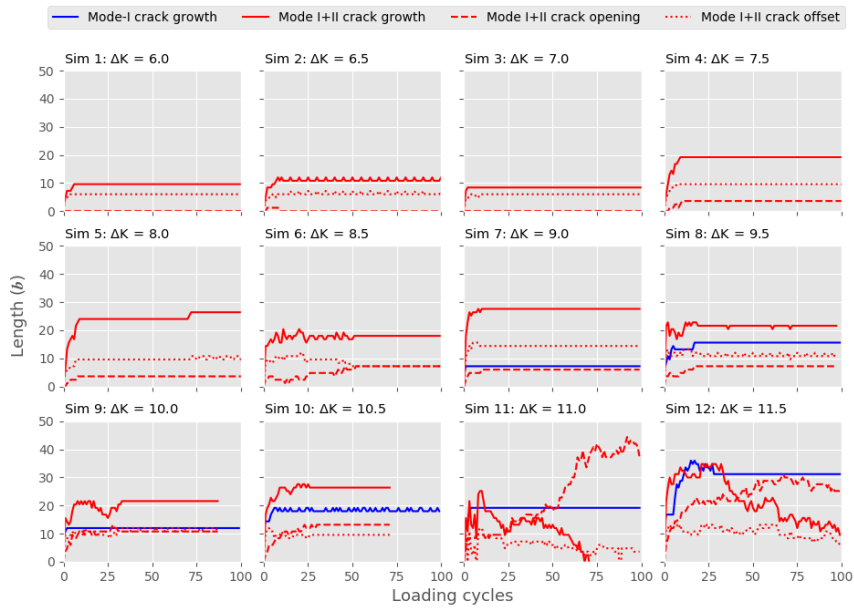


Figure 2.13: Plots of crack growth, crack opening and crack surface offset vs loading cycles from ductile hexagonal lattice simulations under pure mode I and mixed-mode I+II loading. The applied stress intensity range, ΔK , varies from 6.0 to 11.5.

tip is continually evolving under the mixed-mode load. It can be observed that the opening distance between two crack surfaces is enlarging while the length of the crack is shrinking. The change of the crack tip shape could be a sign of crack changing direction as observed in the experiments. Furthermore, the observed correlation between crack growth and crack opening reconciles with the statement that an enhanced opening could in turn lead to crack arrest by decreasing the near tip stresses [80]. Future studies with higher loads and other K_I/K_{II} ratios would be beneficial for further understandings of the fatigue crack behavior under mixed-mode loading.

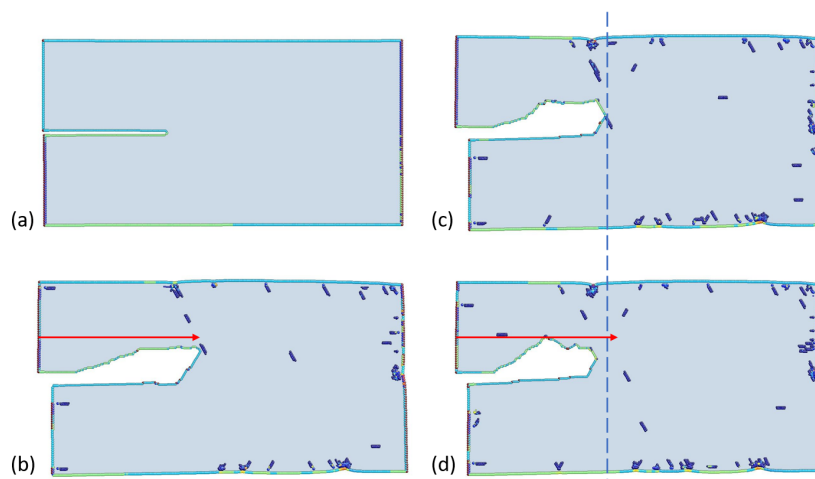


Figure 2.14: Atomistic domain in ductile hexagonal lattice simulation with $\Delta K = 11.5$ under mixed-mode I+II loading. Only atoms with a centrosymmetry parameter not equal to that of the perfect hexagonal crystal are shown in the left figures, i.e. atoms at the crack surface, continuum-atomistic interface, and dislocation cores. (a) Initial configuration at $K = 0.0$; (b) At the end of the 20th cycle; (c) At the end of the 40th cycle; (d) At the end of the 60th cycle. Increasing crack opening and decreasing crack length can be observed.

CHAPTER 3
**ATOMIC MECHANISM OF NEAR THRESHOLD FATIGUE CRACK
GROWTH IN VACUUM**

The growth of cracks governs engineering decisions across a broad range of industry. Yet, in many technologically relevant regimes, the process by which cracks grow remains unknown. A prime example is near threshold fatigue crack growth in vacuum environments, which can govern failures initiated from subsurface material defects [27, 28]. In this case, crack growth per loading cycle can be on the order of angstroms, inhibiting direct observation of the material separation process [24, 26, 81]. Accordingly, atomistic modeling may be the best tool to better understand the phenomenon.

While a large atomistic modeling literature exists [82–86], the link between modeled cracks and laboratory behavior is complicated by disconnects in stress state, simulation geometry, and thermal activation. In cases where care has been devoted to modeling a well-developed cyclic stress field [34, 54, 87–91], fatigue crack growth has been reported. However, such modeling outcomes occur at loading amplitudes well below the corresponding experimentally thresholds for fatigue crack growth in vacuum [73].

By harnessing a concurrent multiscale approach and contemporary computational resources, we have performed atomistic simulations to cycle counts well beyond those analyzed previously. Our simulations show that fatigue crack growth arrests after an initial transient period, reconciling the standing discrepancy between model and experiment.

This finding provides a new vantage to identify the mechanism(s) responsible for the near threshold fatigue crack growth phenomenon in vacuum [92–96]. In examining the atomic-scale function of hypothesized mechanisms, we find sustained crack growth

to only occur when edge dislocations return to the crack tip on a slip plane behind the one on which they were emitted. This process transfers material away from the crack tip, supporting a long-ago hypothesized necessity for near threshold fatigue crack growth in vacuum [97, 98]. The movement of material away from the crack tip inhibits the rewelding of crack faces at the bottom of the load cycle, consistent with carefully executed laboratory observations [99, 100].

The cyclic loads associated with experimentally observed fatigue crack growth thresholds entail micrometers of deformation at the crack tip [95, 101]. This well surpasses modern atomistic modeling capabilities, which at best could simulate a sufficient 2D domain for 10's of loading cycles (with a dedicated ExaFLOP supercomputer using ~\$500,000 of electricity). This challenge has limited the focus of previous studies towards nanometer cracks, lower loading amplitudes, and few loading cycles [34, 54, 87–91, 102–108]. A concurrent multiscale approach [109] addresses the challenge by reducing degrees of freedom, allowing larger simulation domains to be studied over more cycles without sacrificing atomic resolution at the crack tip. For crack behavior, the multiscaling is complicated by the movement of dislocations over large distances, and thus, a coupled atomistic discrete dislocation (CADD) approach is necessary [110]. To achieve the results presented here, a new parallel implementation was necessary, harnessing highly efficient open source finite element and atomistic simulation software. Details are discussed in the methods section.

We begin by presenting the results of a cyclically loaded mode I crack in an initially dislocation free f.c.c. aluminum crystal. The crack is placed on a {113} plane with its front along the $\langle 112 \rangle$ direction. This orientation is favorable relative to other options, as it enables the study of full dislocation emission in the athermal limit in a thin simulation cell [111]. These two features are necessary to make the simulation of many loading

cycles computationally tractable.

An additional strategy to make the many cycle simulations tractable is to limit the size of the plastic zone, reducing the need to integrate the motion of many dislocations over long distances each load cycle. Towards this goal, we investigated the role of dislocation glide resistance in the continuum domain ¹, whereby greater glide resistances reduce the plastic zone size and make the simulations less computationally demanding. Examining a wide range of glide resistances, 150-654 MPa, fatigue crack growth is observed to be independent of this parameter, (Figure 3.1a). This result is consistent with the conclusion of discrete dislocation continuum modeling [65, 66] and experiments [28, 66, 68, 70, 71, 112, 113] that have shown dislocation glide resistance to not directly influence near threshold fatigue crack growth. The result provides validity for subsequently presented simulations that will constrain dislocation motion to the atomistic domain (effectively imposing a high glide resistance) to access high cycle counts.

Simulating beyond the cycle counts previously accessed [34, 54, 87–91, 102–108] reveals crack arrest after the first 10's of cycles, independent of the dislocation glide resistance in the continuum domain (Figure 3.1b). In the arrested state, the crack tip, defect, and dislocation structure is reversible over the course of the cycle, even with repeated dislocation emission and absorption in some cases.

A challenge to interpreting these results relative to corresponding laboratory experiments is that the modeled crack - crystal orientation and thin periodic cell constrain dislocation slip to a single plane. This challenge cannot be directly addressed, as (1) choosing a multi-slip orientation would lead to crack tip twin emission at atomistic modeling timescales [111, 114] and (2) thickening the model to permit slip on other

¹The discontinuity of glide resistance between the atomistic and continuum domain is inconsequential for the results presented here as the driving force on dislocations in the atomistic domain is well above the glide resistance of typical engineering alloys.

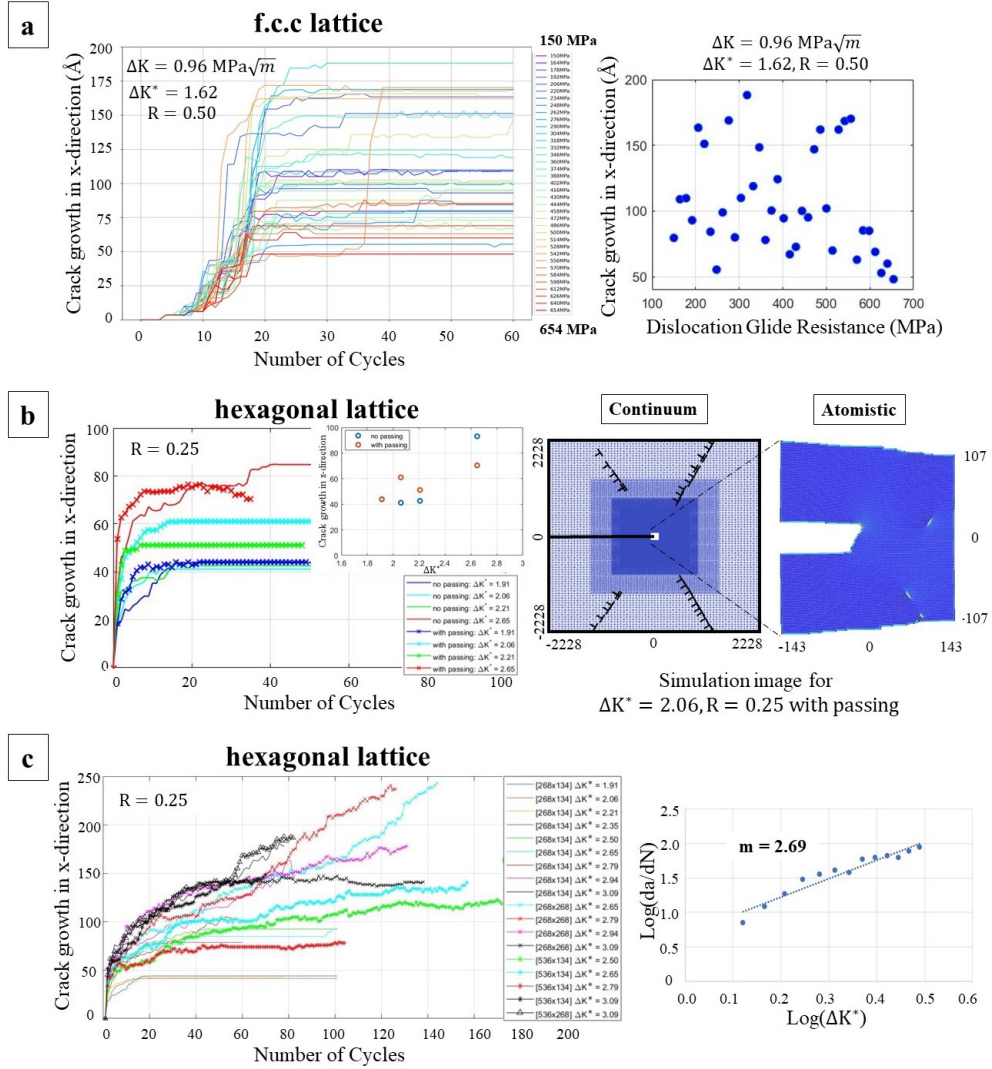


Figure 3.1: Crack advance as a function of loading cycle from three sets of simulations. (a) {113} crack in an f.c.c. aluminum lattice. Each curve represents a distinct dislocation glide resistance in the continuum domain. The majority of cases show crack growth over the first 20 cycles and crack arrest shortly after. On the right, the location of the arrested cracks are shown as a function of glide resistance, showing no correlation between the two variables. (b) A ductile hexagonal lattice at various loading amplitudes. Again, cracks arrest after an initial transient period. Cases are shown both with and without dislocation passing from atomistic to continuum domains to establish that blocking dislocation motion does not influence the behavior. The right shows the dislocation distribution and the crack tip configuration for an arrested crack. (c) A ductile hexagonal lattice with no dislocation passing at larger cycle counts and higher loading amplitudes. Crack arrest was observed in all but a few cases at the higher loading amplitudes. The right image is a plot of $\log(da/dN)$ vs. $\log(\Delta K)$ from the first 10 cycles showing the data conforms to Paris' law, consistent with previous atomistic simulations that analyzed crack growth in the initial transient period. m represents the Paris law exponent, i.e. log-log slope. For the hexagonal lattice simulations, distances are normalized by interatomic spacing, b , and stress intensities are normalized by the stress intensity required to nucleate the first dislocation, $\Delta K^* = \Delta K_I / K_I^{nuc}$.

planes would drastically increase the degrees of freedom making high cycle count simulations intractable. Accordingly, we have examined an opposite bound to the thin f.c.c. simulations, where dislocation slip is under-constrained. This case consists of a ductile hexagonal lattice with slip on 3 planes and glissile dislocation reactions. Details are given in the methods section.

Examining a series of loads, the hexagonal lattice exhibits the same response as the previously presented f.c.c case, with cracks arresting after an initial growth stage (Figure 3.1c). Again, this response is found to be independent of the dislocation glide resistance in the continuum, further establishing that emitted dislocations can be constrained in a sufficiently sized atomistic domain, without artificially influencing the characteristics of crack growth behavior.

Interpreting the above results to suggest that hexagonal lattice simulations with dislocations constrained to the atomistic region can be a valid tool for modeling fatigue crack behavior at attainable computational costs, such simulations were performed at higher loads and long cycle counts. As expected, increased loading amplitude led to increased crack growth, with some instances exhibiting sustained crack growth over the entire duration of the simulation, up to 180 cycles (Figure 3.1c). Comparison of the arrested and growing cracks highlights the complexity of the phenomenon. In both cases, instances of shielding and antishielding dislocation emission, absorption, and dislocation annihilation can be observed during loading cycles. This suggests that none of these mechanisms are sufficient for sustained near threshold fatigue crack growth in vacuum. The finding that dislocation emission from the crack tip is not sufficient for sustained crack growth in vacuum is consistent with the under prediction of the threshold amplitude by discrete dislocation models governed by this mechanism [115–117].

The occurrence of cyclically reversible / arrested crack configurations does decrease

with increased loading amplitude. This suggests that crack arrest is linked to the number of inelastic mechanisms that occur per cycle (such as dislocation emission, absorption, and dislocation reactions). Considering the probabilistic nature of crack arrest and that the modeled loading amplitudes are still significantly below experimental thresholds, we hypothesize that all cracks in Figure 3.1(c) will eventually arrest.

We hypothesize that the novel observation of the crack arrest behavior in Figure 3.1 cannot be attributed to our selection of model parameters, but instead represents a more general behavior that has just now been observed by simulating to cycle counts well beyond those examined previously. To support this assertion, we examined the correlation between the rate of crack growth, $\log(da/dN)$, versus loading amplitude, $\log(\Delta K)$, as commonly done in the fatigue literature (Figure 3.1c insert). Extracting data from the initial transient growth region during the first 10 loading cycles, the observed slope (Paris law exponent) is consistent with the atomistic modeling literature limited to low cycle counts. Specifically, a Paris law exponent of 2.7 has been observed in our simulations and 2.8 by Zhou et al. [90], 2.4 by Uhnakova et al. [87], 3.5 by Baker and Warner [54].

Beyond the benefit of computational cost, the coupled atomistic discrete dislocation model provides a means to directly assess the feasibility of previously suggested crack growth mechanisms without requiring increased loading amplitude, which would make simulation to high cycle counts intractable.

In this spirit, we examined the role of plastic slip reversibility, which has been considered key to fatigue failure for over a century² [121–123]. Toward this goal, simulations were performed with dislocation glide in the continuum domain being constrained to a single direction, away from the crack tip. As shown in Figure 3.2(a), cracks quickly

²Noting that the role of plastic slip reversibility on crack propagation has remained less clear [118–120]

arrested in these simulations, despite shielding and antishielding dislocations being continually emitted. Elementary analysis gives no expectation that this result would change at higher loading amplitudes, i.e. slip irreversibility (as implemented) is not sufficient for near threshold crack growth in vacuum.

A less severe plastic irreversibility might involve the formation of debris in front of the crack tip via pinned dislocation segments and/or junctions that are unable to return to the crack upon unloading. The formation of such debris is not uncommon in atomistic simulations, where it has produced transient periods of fatigue crack growth in some cases [54, 89]. Yet, the formation and stability of such debris in atomistic simulations is exaggerated due to the lack of thermal activation [124]. Experimentally, conflicting reports exist, with debris being observed near the crack tip [81] and the absence of it [24], albeit at a coarser scale.

Other suggested mechanisms involve the motion of dislocations into the vicinity of the crack tip. The arrival of such dislocations can provoke cleavage and dislocation emission [66, 125] and might be important for sustained fatigue crack growth. To examine this point, simulations were performed with starting configurations having arrays of dislocations and dislocation sources in the continuum. After preliminary analysis, simulations involving random configurations of dislocations and dislocation sources were abandoned for strategically chosen configurations that would best facilitate sustained crack growth³. Figure 3.2b shows an example where sources were aligned to emit dislocations towards the crack tip to promote growth. Details of simulation set up is discussed in the Methods section. While the presence of such sources did promote crack growth over the first ~5 cycles, the cracks ultimately arrested. Their arrest was due to the stress field of emitted dislocations eventually shielding sources from activating on subsequent

³Randomly placed preexisting dislocations and sources rarely leads to dislocations arriving within a range of influence of the crack tip

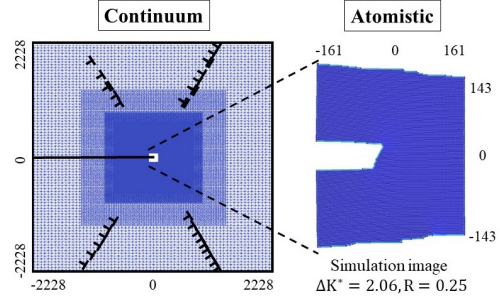
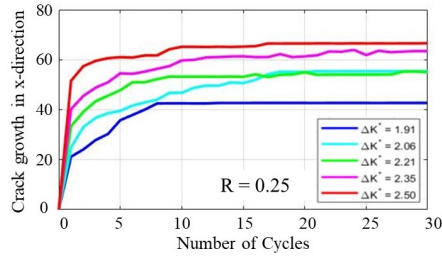
cycles such that no new dislocation dipoles are emitted, leading to a reversible configuration.

In a further attempt to produce sustained near threshold fatigue crack growth, pre-existing dislocations were aligned in the form of a dense persistent slip band (PSB) configured to send antishielding dislocations to the crack tip, promoting crack growth. Details of simulation set up are discussed in the methods section. The PSB configuration is particularly relevant given the many experimental observations of fatigue crack growth along PSBs [2, 28]. As shown in Figure 3.2c, the presence of the PSB does enhance growth over the first few cycles. However, the crack eventually arrests due to the formation of stable dislocation arrangements, preventing continued movement of PSB dislocations towards the crack tip to continually facilitate growth. Thus, preexisting dislocations are not a sufficient ingredient for sustaining near threshold fatigue crack growth, at least for the loads and configurations simulated here. Nonetheless, the results do not suggest a lack of interaction between propagating cracks and PSBs, and thus do not contradict the common observations of fatigue cracks at PSBs [126].

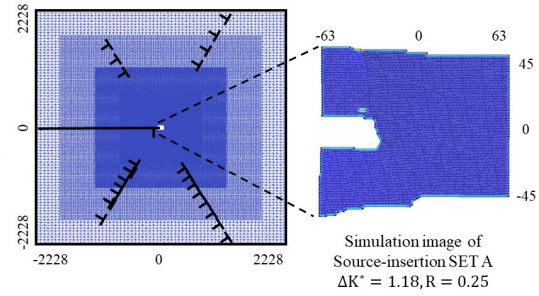
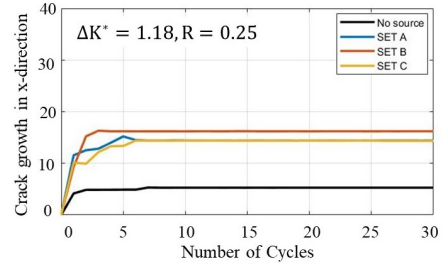
Both the simulations with strategically placed sources and PSBs suggest that crack growth could be sustained if dislocations of proper sign continuously arrived at the crack tip as it propagates. The most conceivable means that this might occur is by dislocations emitted from the crack tip changing planes prior to their return on the opposite side of the loading cycle. Such a process would provide a continuously moving source of dislocations that would enable continued fatigue crack propagation via the removal of material at the crack tip.

This hypothesis can easily be tested with the CADD simulation framework by changing the slip plane of emitted dislocations prior to their return to the crack tip. Simulations were conducted at low loading magnitudes where only 1 or 2 dislocations were emitted

(a) Slip irreversibility simulations



(b) Source-insertion simulations



(c) PSB simulations

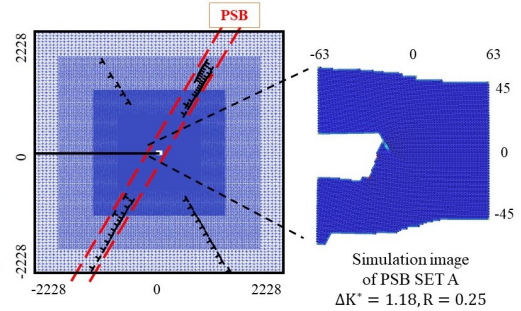
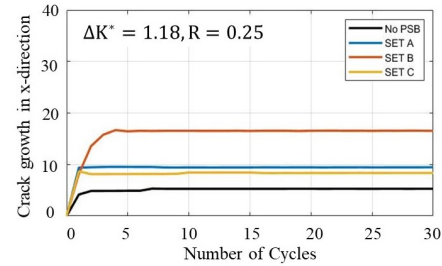


Figure 3.2: Crack advance as a function of loading cycle from three sets of simulations. Sample continuum and atomistic configurations are shown from when the crack reaches an arrested state. (a) Simulations with slip irreversibility, where dislocation motion is limited to the direction away from the crack tip. (b) Simulations with dislocation sources in the continuum, which exhibit enhanced crack growth over the initial cycles, but eventually crack arrest. (c) Simulations with pre-existing dislocations in the continuum aligned as a PSB. The presence of the PSB dislocations enhances growth over the initial cycles, but eventually crack arrest occurs. Details about SET A, B, and C in (b) and (c) are discussed in the methods section. Distances are normalized by interatomic spacing, b , and stress intensities are normalized by the stress intensity required to nucleate the first dislocation, $\Delta K^* = \Delta K_I / K_I^{nuc}$.

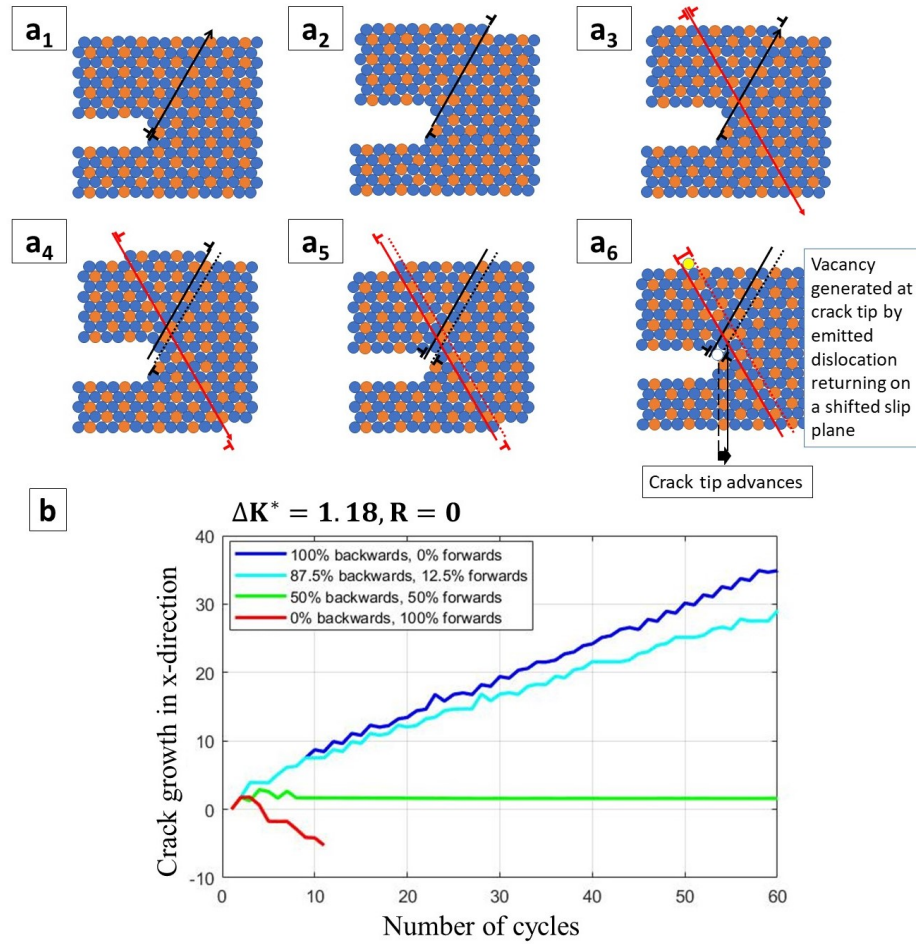


Figure 3.3: (a₁)-(a₆): Schematic of crack advance by slip trace intersection. Atom are colored to show deformation. A case is shown where the slip trace of a dislocation nucleated from the crack tip intersects the slip trace of a dislocation on a different slip plane. The intersection results in a change in slip plane when the dislocations return to their original position on the unload. This process leads to the removal of an atom from the crack tip without diffusion. Atom highlighted in yellow in (a₆) is the companion to the vacancy that was created at the crack tip. (b) Crack growth vs. number of cycles with the slip plane of emitted dislocations being changed prior to their absorption into the crack on the unload. The results show that shifting the slip plane of emitted dislocations backwards (in the opposite direction of crack growth) produces sustained crack growth, consistent with the schematic in (a₁)-(a₆). Crack closure was observed in the case when the slip planes were shifted forward, and no crack growth was observed when dislocations were shifted forward and backward in equal proportion. Distances are normalized by interatomic spacing, b , and stress intensity by the stress intensity required to nucleate the first dislocation, $\Delta K^* = \Delta K_I / K_I^{nuc}$.

and absorbed during a loading cycle. Details of the simulations are given in the methods section. Without changing the slip plane of these dislocations, the behavior of the crack at these low loading amplitudes is completely reversible from the first loading cycle. However, when the position of the emitted dislocations changes to a different plane prior to their absorption upon unload, continued crack growth is observed for the case of the new slip plane being behind the crack tip (Figure 3.3b). Conversely, when emitted shielding dislocations change planes in the other direction, moving in front of the crack tip, the crack closes.

This behavior can be understood by considering the cyclic motion of two intersecting slip traces, which can remove or place material at the crack tip over the course of a loading cycle (Figure 3.3a). The removal of material by the action of intersecting slip traces was hypothesized over 50 years ago by Cottrell and Hull [97] for the formation of surface intrusions; and now here, we find its occurrence at crack tips in the simulations presented in Figure 3.1(c) that exhibited fatigue crack growth at high cycle counts (Figure 3.4).

With that said, the intersection of slip traces may be exaggerated in the hexagonal lattice simulations due to the prevalence of glissile dislocation reactions relative to real 3D cubic lattices. Nonetheless, real 3D cubic lattices offer a double cross-slip mechanism that could produce a change in the plane of edge dislocations over the course of a loading cycle [97, 98, 127]. It is important to emphasize that in either case the dislocation shifting mechanism does not require diffusion, consistent with the weak influence of temperature on fatigue crack growth in the absence of environmental factors [48, 49].

In total, performing fatigue simulations to cycle counts beyond those previously accessible reveals a regime of transient sub-threshold fatigue crack growth in vacuum. This behavior reconciles the reports of crack growth in atomistic simulations at loading

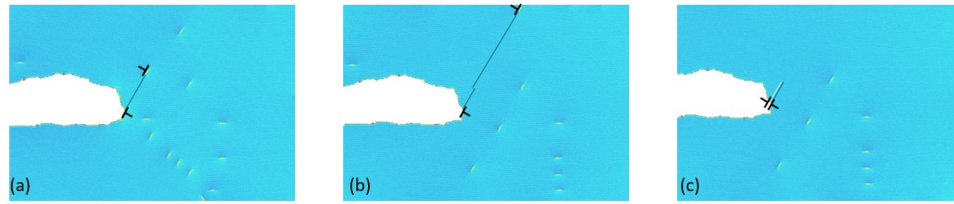


Figure 3.4: Example of crack growth by the intersection of slip traces in a hexagonal lattice simulation, $[600b \times 300b]$ $\Delta K^* = 3.09$. The black dislocation dipole in (a) highlights a dislocation that has been emitted from the crack on the upload of cycle 82. Upon further loading, (b) shows the slip trace of the emitted dislocation (black line) having been intersected by another dislocation slip trace. Upon unloading, (c) shows the highlighted emitted dislocation having returned to the crack tip in an offset location, leaving a pair of offset slip trace segments and removing an atom from the crack tip. Atoms are colored by strain relative to perfect lattice to illuminate dislocation cores.

amplitudes below experimental crack growth thresholds. Neither slip irreversibility, pre-existing dislocation sources, nor preexisting dislocations in the form of a slip band are observed to be sufficient for sustained fatigue crack growth at low loading amplitudes. Sustained fatigue crack growth is only observed when emitted dislocations change slip planes prior to absorbing back into the crack on the opposite side of the loading cycle. This process was observed to occur naturally in simulations by the intersection of slip traces, and is expected to occur in 3D crystals by an additional mechanism, i.e. the long-ago proposed double cross slip mechanism. Future atomistic simulations can harness this finding and that of the transient sub-threshold growth regime to better connect to the actual near threshold fatigue crack growth process. Ultimately, the slip plane shifting mechanism (whether due to slip trace intersection, double cross slip, or a yet to be determined mechanism) can be expressed in terms of fundamental material properties that can be computed from first principles via Khon-Sham Density Functional Theory. This link between alloy composition and fatigue crack growth resistance provides a route forward towards more robust continuum prognosis models and the design of fatigue resistant alloys.

3.1 Methods

The coupled atomistic discrete dislocation simulation setup is shown in Figure 3.5 and the full methodology is described in [109, 110].

The fcc aluminum simulations were performed in a $[4960b \times 4960b]$ continuum domain with a $[77b \times 84b \times 2b]$ embedded atomistic region at the crack tip. The atomistic region was governed by the Ercolessi and Adams [52] interatomic potential which has been shown to accurately reproduce pure aluminum crack tip behavior [128]. The crack was created by removing 3 consecutive planes of atoms. Loads were applied by prescribed displacements at the outer boundary of the continuum region corresponding to the solution for a sharp crack in an anisotropic linear elastic material subjected to mode I loading. The loading increment after each mechanical equilibration was $0.02 \text{ MPa } \sqrt{m}$. Dislocation nucleation first occurred at $K_I = K_{IN} = 0.59 \text{ MPa } \sqrt{m}$.

In the present work, we built a framework to utilize LAMMPS [56] to conduct the molecular static simulation for the atomistic region and FEniCS [64] for the finite element analysis of the continuum region. We refer to the method as LF-CADD. The underlying theory of this multiscale method was identical to Shilkrot et al [110], but the integration of the two open-source packages enabled us to simulate fatigue crack growth more efficiently and in parallel.

The hexagonal lattice simulations were performed in a $[4464b \times 4464b]$ continuum domain with an embedded atomistic region at the crack tip ranging from $[268b \times 134b]$ to $[536b \times 268b]$ (for simulations without continuum discrete dislocations). The crack was created by removing 3 consecutive planes of atoms.

The atomistic region was governed by a ductile interatomic pair potential given in

[129] (potential A). In the normalized units of the potential, the shear modulus μ is 10.61 and the critical load for the nucleation of the first dislocation is $K_I = K_{IN} = 6.8$. The Griffith cleavage value is $K_I = 7.5$. In the fatigue simulations the loading increment after each mechanical equilibration was $K = 0.1$. For discrete dislocations in the continuum, the lattice resistance normalized by the shear modulus was $1.9E-3$.

The simulation set up for the source-insertion and PSB cases is illustrated in Figure 3.6. For source-insertion simulations, an array of three Frank-Read sources, separated by $20b$, was inserted into the continuum just outside the atomistic window on each side of the crack. When the total resolved shear stress of a source exceeds a critical value as described in [130], it emitted dislocations dipoles on a slip plane that intersected the crack tip region, as shown in Figure 3.6(a). A total of three sets of simulations with variations in source array locations were conducted. In each set of the PSB simulations, a pre-existing PSB with width of $10b$ and spacing of $200b$ was constructed following the schematics by M.D. Sangid [2] as shown in 3.6(b). Among the three sets of simulations performed, two of the PSBs were oriented in the same direction as the slip plane making a 60° angle counterclockwise from the x-axis, and one 60° clockwise.

Figure 3.7 conveys the slip plane shifting implementation. After a dislocation emits and reaches the detection band near the atomistic-continuum interface, it is passed from the atomistic domain and placed outside of the continuum domain. At this time, a dislocation dipole is inserted on a neighboring slip plane. One of these dislocations is placed next to the passed dislocation outside the continuum domain and the other is placed just outside of the atomistic domain. Only the dislocation that is placed just outside the atomistic domain is mobile under the action of an applied stress. For the slip plane shifting simulations to be worthwhile, the shifted dislocation must return to the crack during the unloading portion of the load cycle. For computational expediency, the

distance from the crack tip that dislocations could travel was limited to $90b$ measured from the crack tip at the beginning of simulation and an artificial resolved shear stress of $0.12/\mu$ was added to the dislocation, both of which made dislocations return to the crack tip more quickly upon the unload.

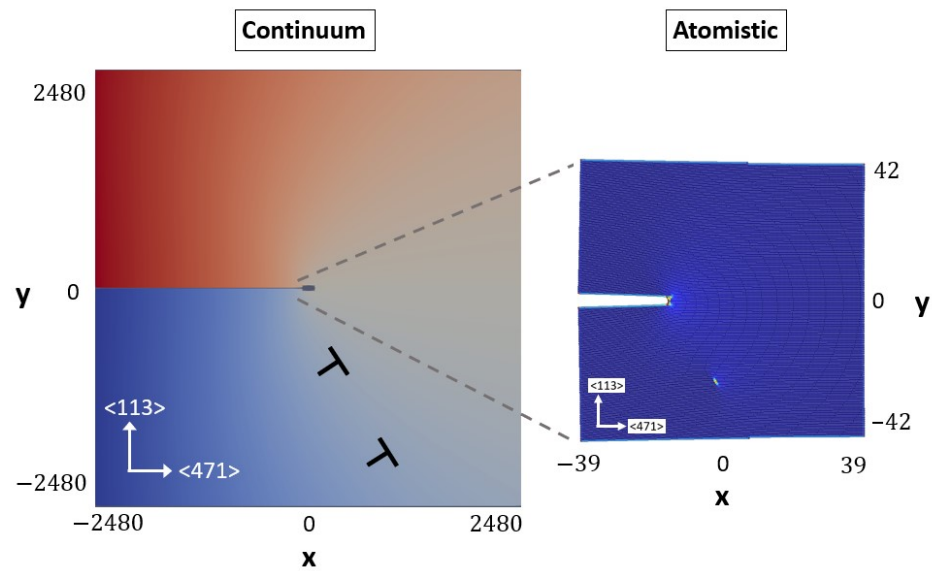


Figure 3.5: Multiscale simulation set up for the $\langle 471 \rangle / \langle 113 \rangle$ crack orientation in which an atomistic domain (right) is embedded in a linear elastic continuum domain (left). Dislocations can move between domains on their corresponding slip planes. The lengths given in this figure are normalized with respect to the burgers vector b , and the images are not drawn to scale. The continuum coloring represents the macroscopic displacement in the y direction and the atomistic coloring corresponds to the potential energy of the atoms, highlighting an edge dislocation that has been emitted from the crack tip.

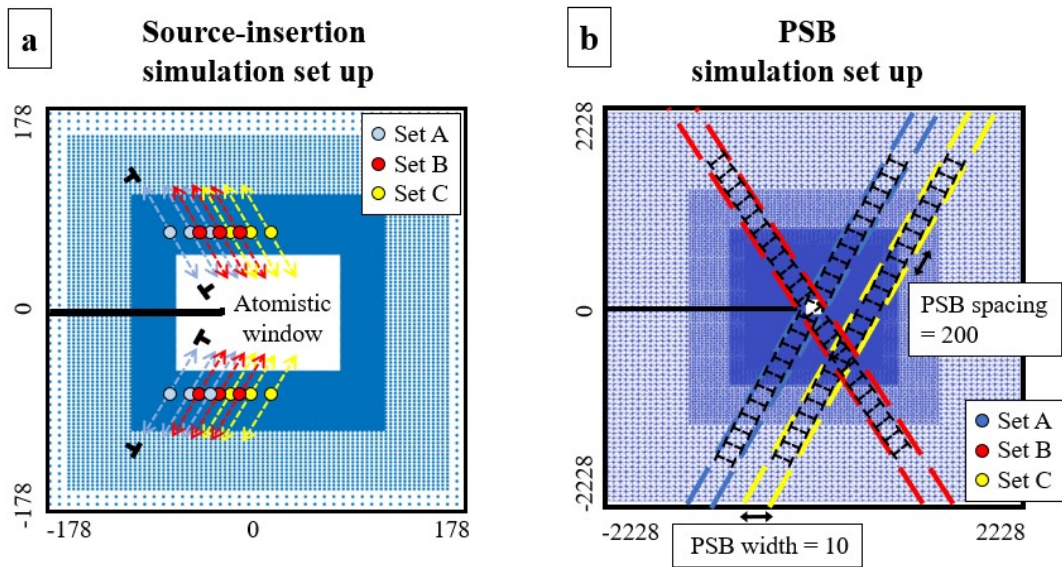


Figure 3.6: (a) Source-insertion simulation set up. In each set, an array of three Frank-Read sources was inserted into the continuum just outside the atomistic window on each side of the crack. The sources within each array were set apart by $20b$, and each source emitted a dislocation dipole when its total resolved shear stress exceeded a critical value along the slip plane. The dislocation entering the atomistic window was constructed to be an anti-shielding dislocation gliding towards the crack tip region. (b) PSB simulation set up. In each set, a pre-existing persistent slip band (PSB) with width of $10b$ and spacing of $200b$ was constructed following the schematics by M.D. Sangid [2]. The PSB was arranged to intersect the crack tip region. The lengths given in this figure are normalized with respect to the burgers vector b , and the images are not drawn to scale.

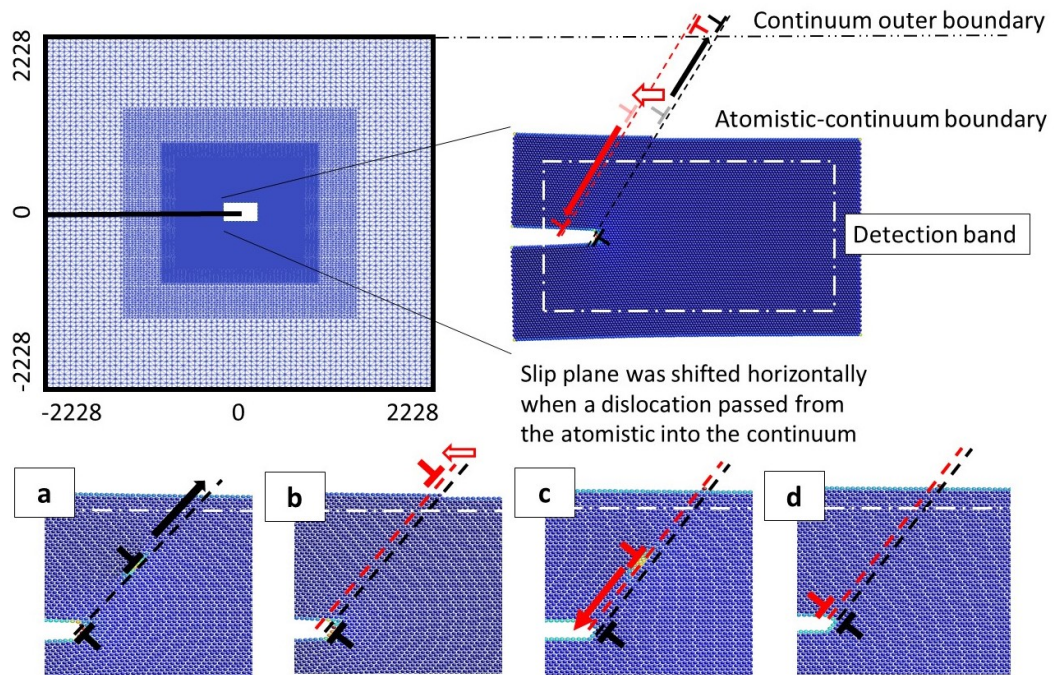


Figure 3.7: Illustration of slip plane shifting implementation. (a) When a dislocation (black) nucleated from the crack tip and glided across the detection band inside the atomistic domain, (b) its slip plane was shifted after being passed across the interface (red). In order to maintain the correct displacement fields of both the original and the shifted dislocations, the previously passed dislocation (black) was moved and pinned outside the continuum domain and a new “opposite” dipole dislocation (red) on the shifted slip plane was added. During unload, (c) the shifted (red) dislocation glided back into the atomistic and (d) eventually returned to the crack tip. In all slip plane shifting simulations, the distance of each shift is $1b$. The lengths given in this figure are normalized with respect to the burgers vector b , and the images are not drawn to scale.

CHAPTER 4

DISSOLUTION AT A CRACK TIP

The environment can accelerate crack growth rates by orders of magnitude, leading to unexpected and catastrophic outcomes. Examples include the role of humidity on aerospace alloys [131, 132], sulfides on pipeline steels [133], and liquid metals on reactor pressure vessels [134]. Yet, there are instances where environment acts in the opposite way, improving structural performance; with examples ranging from structural metals in specific liquid environments [69, 135–139] to the dissolving action of osteoclasts on bone, which is essential for maintaining bone fracture resistance [140].

Despite a long documented knowledge of environmental effects [141], the controlling mechanisms remain clouded. At fault are several challenges. First, multiple mechanisms can act simultaneously, e.g. dissolution, oxide fracture, oxide formation, and hydrogen embrittlement. Second, the scale of the material separation process on which the environment acts is atomistic, inhibiting direct observation [24, 81, 131, 142–145]. In light of these challenges, atomistic modeling can serve as a powerful probe to illuminate the mechanisms governing environmental effects [82], providing a means to study the material separation processes under the action of isolated mechanisms. Here, focus is directed towards the action of material dissolution at a crack tip.

A novel implementation of the concurrently coupled atomistic - discrete dislocation approach [110] is harnessed to allow the study of a highly deformed crack tip in a well developed crack stress field, better approaching real-world conditions. The model consists of an edge crack centered in an $[4464b \times 4464b]$ square domain (Figure 4.1), which is created by removing 3 consecutive planes of atoms. The $[268b \times 134b]$ atomistic region at the crack tip is coupled to the surrounding continuum region by self-consistent displacement boundary conditions [109]. Mechanical equilibrium is obtained

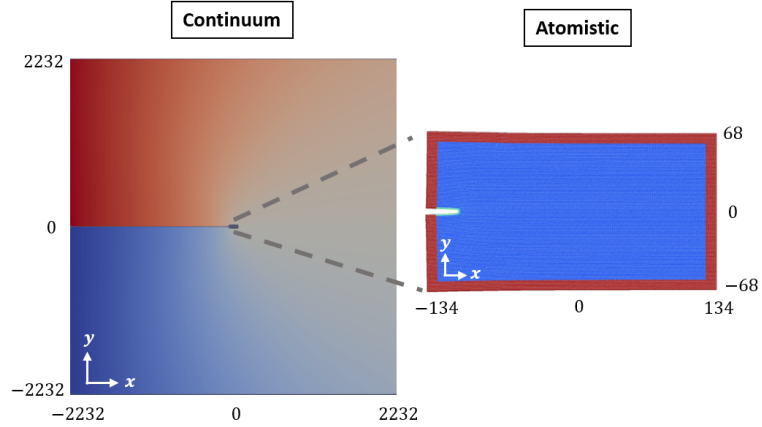


Figure 4.1: Multiscale simulation setup with an atomistic domain embedded in a linear elastic continuum domain. The lengths given in this figure are normalized by the burgers vector magnitude, \mathbf{b} , and the images are not drawn to scale. The continuum coloring represents the macroscopic displacement in the y direction, pad atoms are coloring in red, and atoms inside the atomistic region are colored according to their potential energy, highlighting the crack surface.

using LAMMPS [56] for the atomistic region and FEniCS [64] for the continuum region. We refer to this approach as LF-CADD. The continuum region is governed by 2D plane-strain linear elasticity with elastic constants chosen to match the interatomic potential of the atomistic region. Loads are applied by prescribed displacements at the outer boundary of the continuum region corresponding to the solution for a sharp crack in a linear elastic material subjected to mode I loading, and the loading increment after each mechanical equilibration was 0.015 (normalized by K_I^{nuc}). All cyclic loading simulations had a constant stress intensity range ($\Delta K^* = K_I^{max}/K_I^{nuc} - K_I^{min}/K_I^{nuc}$) throughout the simulation with a load ratio ($R = K_I^{max}/K_I^{min}$) of 0.25.

Even with the multiscale approach and the utilization of substantial computational resources, gaps between the atomistic model and reality still exist. Accordingly, the atomistic study must be focused towards specific features. Here, we target the large deformation history associated with cyclic loading to hundreds of cycles; motivated by the little understood but technologically consequential process of corrosion fatigue, which

can induce catastrophic failure under loads and environments that would be benign if acting alone [146, 147].

The high cycle counts are achieved by simulating a 2D hexagonal lattice in the athermal limit. The response of the hexagonal lattice is governed by the intrinsically ductile interatomic potential of Rajan et al. (Potential A in [148]). This approach is appealing in that it offers three dislocation slip systems and glissile dislocation reactions in 2D. In contrast, the alternative of using thin 3D crystallographies overconstrains plastic slip relative to real 3D geometries [149–152]. For the interatomic potential and crack-crystal orientation used here, $K_I^{nuc} = 6.8$.

An additional strategy to make the many cycle simulations tractable is to limit the size of the plastic zone, reducing the need to integrate the motion of many dislocations over long distances during each load cycle. Towards this goal, we investigated the role of dislocation glide resistance in the continuum domain¹, whereby greater glide resistances reduce the plastic zone size making the simulations less computationally demanding. Examining a wide range of glide resistances, fatigue crack growth is observed to be independent of this parameter [153]. This result is consistent with the conclusion of discrete dislocation continuum modeling [65, 66] and experiments [28, 66–71] that have shown dislocation glide resistance to not directly influence near threshold fatigue crack growth. The result provides validity for subsequently presented simulations where dislocation motion was constrained to the atomistic domain (effectively imposing a high glide resistance) in order to access high cycle counts.

To begin, the response of cracks subjected to dissolution at fixed stress intensity factors is presented. For simplicity and consistency with the athermal limit approximation,

¹The discontinuity of glide resistance between the atomistic and continuum domain is inconsequential for the results presented here as the driving force on dislocations in the atomistic domain is well above the glide resistance of ordinary engineering alloys.

dissolution was modeled by the removal of the highest energy surface atom followed by mechanical equilibration². The atom removal - mechanical equilibration process was repeated to simulate progressive dissolution in the context of the mechanical equilibration timescale being short relative to the interval between single atom dissolution events. A representative case at a fixed loading of $K^* = K_I/K_I^{nuc} = 1.96$ is shown in Figure 4.2. The images depict a progressive crack opening process due to dissolution, which is the first key result of this paper.

In coloring atoms by their energy levels, Figure 4.2 illustrates that the effect of the crack tip stress field is overwhelmed by the differences in the atomic coordination number of surface atoms. In most cases, dissolution begins with the removal of the lowly coordinated atoms at surface steps created by dislocation emission during mechanical loading. In the cases where no lowly coordinated atomic steps exist, the stress field does influence dissolution with atom removal occurring near a sharp corner of the crack. In this case a lowly coordinate surface step is formed and becomes the site for subsequent dissolution. Dissolution at surface steps does not lead to their removal, but causes step propagation, as can be seen in Figure 4.2(d). Geometry dictates that a propagating step will either be absorbed into a corner of the crack tip or eventually propagate away from the crack tip, acting to open (blunt) the crack.

The dissolution of atoms at a loaded crack tip can cause load redistribution of sufficient magnitude to induce dislocation emission, as seen when comparing Figure 4.2(c) with Figure 4.2(b). Relative to the vast literature on environmentally induced plasticity [147, 154–157], this result is noteworthy in that it shows the induction of plasticity without a change in surface energy, surface step energy, or surface film structure. While dissolution is not focused at the crack tip, the resulting dislocation emission is most

²Simulations involving a random room temperature effect in the selection of the dissolved atom did not produce qualitatively different results.

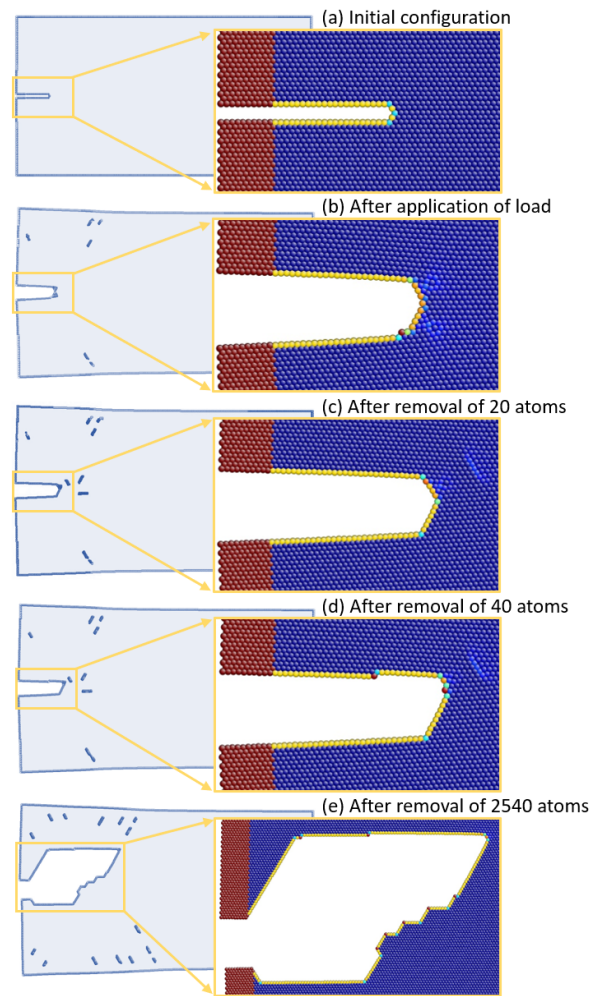


Figure 4.2: Atomistic domain and crack tip under static loading with dissolution. Only atoms with a centrosymmetry parameter not equal to that of the perfect hexagonal crystal are shown in the left figures, i.e. atoms at the crack surface, continuum-atomistic interface, and dislocation cores. Figures on the right show zoomed views of the crack with atoms colored by their energy, with the exception of the continuum region pad atoms that are shown in red. (a) Initial configuration at $K^* = 0.0$; (b) After application of load before atom removal ($K^* = 1.96$); (c) After removal of 20 atoms ($K^* = 1.96$); (d) After removal of 40 atoms ($K^* = 1.96$); (e) After removal of 2540 atoms ($K^* = 1.96$).

prevalent at the crack tip due to the load redistribution being most significant at that location. Subsequently, surface step formation occurs most frequently at the crack tip. However, the generation of surface steps at the crack tip does not sufficiently focus subsequent dissolution to the crack tip (such that crack growth dominates blunting) due to the propagation of the surface steps away from the crack tip.

On the whole, these simulations together with the long-established laboratory trend of plasticity induced dissolution [158, 159] suggest that dissolution induced crack propagation (if it exists) must occur via a mechanism not included here, such as surface film rupture or heterogeneous phases [147, 156, 157, 160, 161].

Next, the results of simulations that examine the action of dissolution under cyclic mechanical loading are presented, i.e. fatigue loading. To provide a baseline for comparison, cyclic loading simulations without dissolution were also performed. The progression of crack geometry without dissolution is shown in Figure 4.5(a). From these curves it is clear that the crack arrests after an initial growth stage, with all dislocation activity becoming fully reversible over the course of the loading cycle (Figure 4.3). As discussed in [153], this result is not thought to be attributable to a simulation artifacts, but instead result from the inaction of the mechanisms required for fatigue crack growth in vacuum. As such, we consider the loadings to be below the vacuum fatigue crack growth threshold.

Similar to the static loading simulations, dissolution was simulated by successively removing the highest energy atoms then mechanically equilibrating at the peak of each loading cycle. Comparing simulations with and without dissolution, the dissolution processes unlocks cracks from arrested states. In this way the dissolution process is found to be capable of promoting crack growth under cyclic mechanical loading, which is the second key result of this paper.

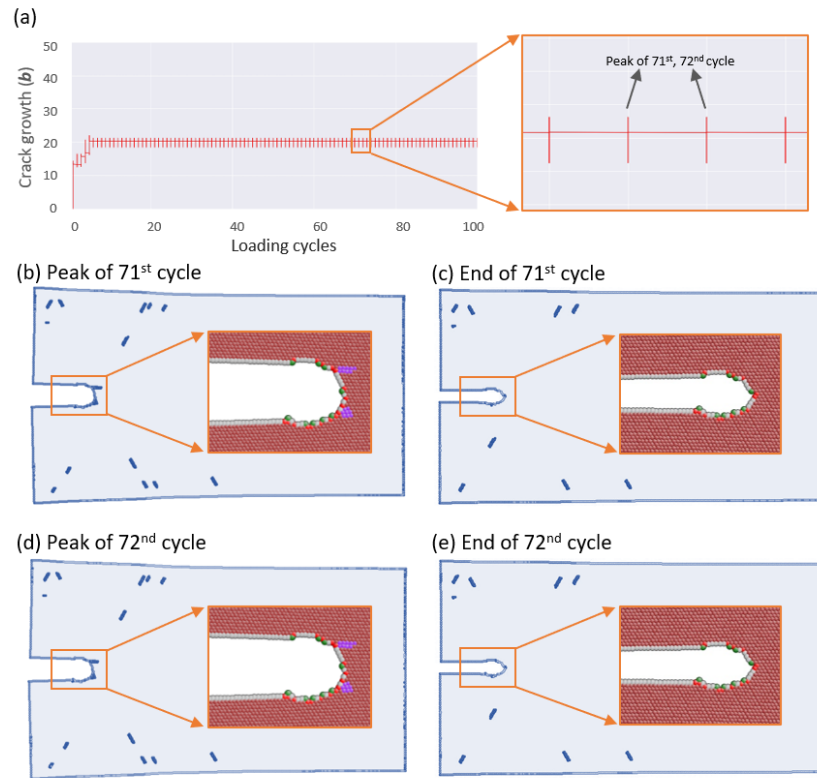


Figure 4.3: Crack growth and corresponding atomistic domain in cyclically loaded simulation with and without dissolution at $\Delta K^* = 1.62$. Only atoms with a centrosymmetry parameter not equal to that of the perfect hexagonal crystal are shown, i.e. atoms at the crack surface, continuum-atomistic interface, and dislocation cores. Inserts show zoomed view of the crack tip where atoms in the atomistic region are colored based on the coordination number. (a) Crack growth in x-direction as a function of simulation cycles; (b) Peak of the 71st cycle ($K^* = 2.16$); (c) End of the 71st cycle ($K^* = 0.54$); (d) Peak of the 72nd cycle ($K^* = 2.16$); (e) End of the 72nd cycle ($K^* = 0.54$).

A detailed example of this process is shown in Figure 4.4 for $\Delta K^* = 1.47$ and a dissolution rate of 10 atoms per mechanical loading cycle. The crack arrests at cycle 78 as emitted dislocations during loading are absorbed back to the crack during unloading, resulting in a reversible state. In cycle 83, the dissolution process is solely focused on a surface step at the crack face away from where dislocation emission and absorption occur. As such, the crack remains in the arrested state. However, in cycle 84, the propagating surface step is absorbed into the boundary of the atomistic domain. Subsequent

dissolution then occurs at the corners of the crack tip, causing a redistribution of load that is sufficient to induce dislocation emission. Ultimately, the action of dissolution and the induced dislocation emission advance the position of the crack tip at the peak of the next loading cycle, unlocking the crack from its reversible arrested state.

Increasing the per cycle dissolution rate decreases the time between crack tip atom removal events. This shortens the time that a crack resides in arrested states, which can consequently increase the average crack growth rate. The behavior is shown in Figs. 4.5(g) & 4.5(i), which display the results of simulations at $\Delta K^* = 1.47$ with differing dissolution rates. The enhancement of crack growth with dissolution plateaus, in correspondence with the elimination of arrested states to be unlocked. On this point, arrested states are less common at higher cyclic loading amplitudes, e.g. $\Delta K^* = 2.21$; and thus, the enhancement offered by dissolution is saturated to a lower value of dissolution rate, [Figs. 4.5(d) & 4.5(f)].

An increment in the dissolution rate also accelerates the rate of atom removal at the crack faces through increased surface step propagation. As in the static loading case, increasing the dissolution rate increases the crack opening under cyclic loading [Figs. 4.5(e) & 4.5(h)]. Consistent with the process not depending on the number of surface steps (but the collective distance that steps have propagated), the relationship between crack opening and dissolution rate is found to be linear and insensitive to loading amplitude [Figs. 4.5(c), 4.5(f), & 4.5(i)].

In total, the preceding indicates that while dissolution can enhance fatigue crack growth by freeing arrested cracks, it will always enhance crack opening. At a real-world engineering scale (millimeters) [162], an enhanced opening will govern the outcome. This is apparent when considering the dependence of near tip stresses on crack geometry. Characterizing crack opening as crack tip radius, ρ , and acknowledging that this value

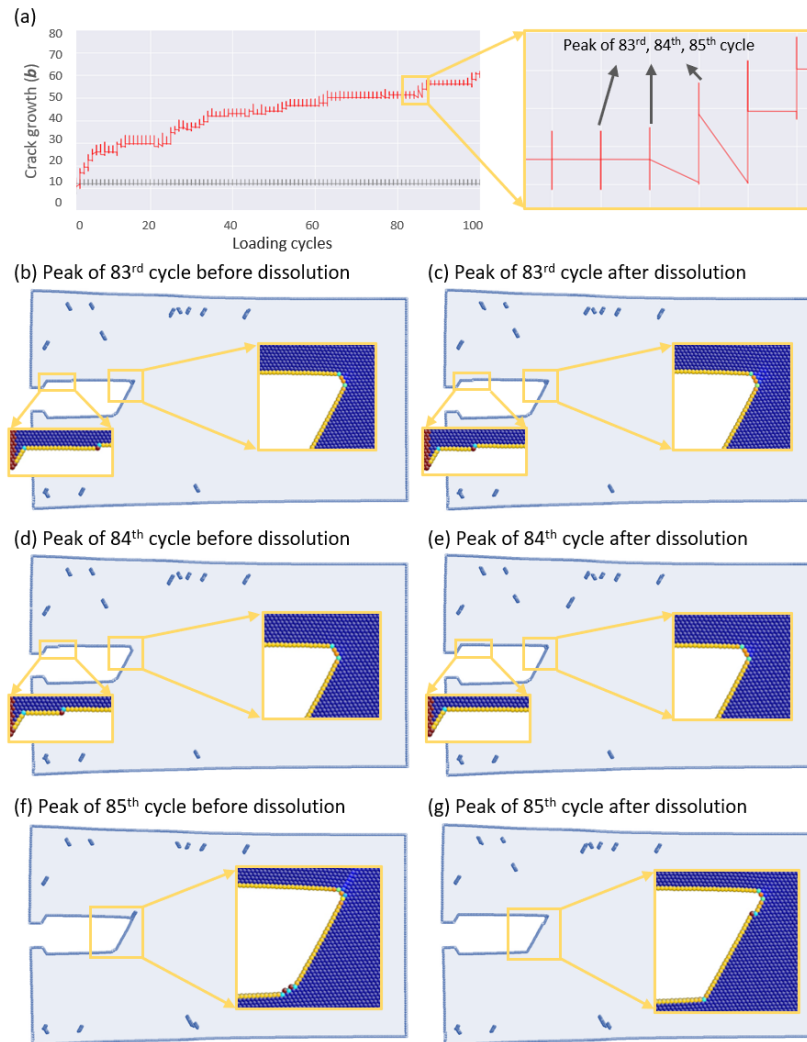


Figure 4.4: Atomistic domain and crack tip in cyclic loading simulation ($\Delta K^* = 1.47$) with dissolution rate of 10 atoms/cycle. Only atoms with a centrosymmetry parameter not equal to that of the perfect hexagonal crystal are shown in the primary images, i.e. atoms at the crack surface, continuum-atomistic interface, and dislocation cores. Inset images give zoomed views with atoms colored by their energy. (a) Crack growth in x-direction as a function of loading cycles with (in red) and without (in grey) dissolution ; (b) Peak of the 83rd cycle before dissolution; (c) Peak of the 83rd cycle after dissolution; (d) Peak of the 84th cycle before dissolution; (e) Peak of the 84th cycle after dissolution; (f) Peak of the 85th cycle before dissolution; (g) Peak of the 85th cycle after dissolution.

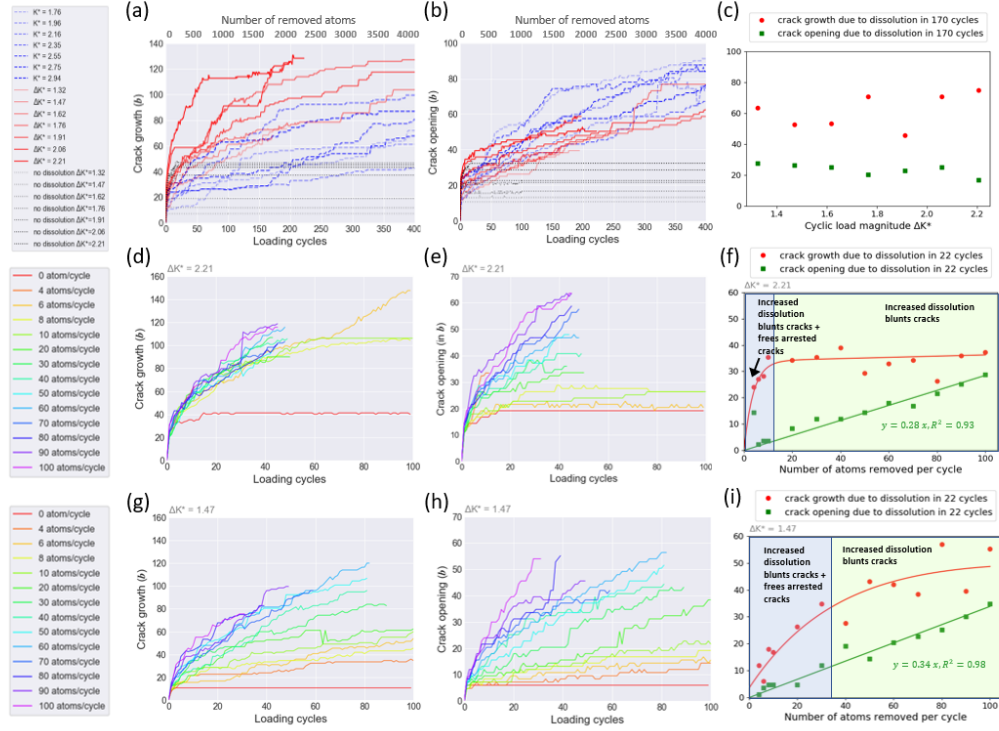


Figure 4.5: Crack growth and opening for a range of loadings and dissolution rates. In (a) and (b) cyclically loaded simulations with dissolution of 10 atoms per cycle are compared to a corresponding set of simulations with no dissolution w.r.t. the number of loading cycles. These simulations are also compared to a corresponding set of statically loaded simulations w.r.t. the number of atoms removed due to dissolution. In (c) the dissolution enhanced crack growth and opening for the cyclically loaded simulations is shown to be independent of loading amplitude at 170 cycles. In (d) through (f), and (g) through (i) the effects of dissolution rate are shown for two cyclic loading amplitudes, i.e. $\Delta K^* = 2.21$ and $\Delta K^* = 1.47$ respectively. The units of the y-axes are normalized by b . In (f) and (i) the gray region represents a regime where increasing dissolution rate will increase crack blunting and the frequency by which arrested cracks are freed. In the gray region, crack arrest is not common so increasing the dissolution rate will only increase crack blunting.

is orders of magnitude less than the crack length, a , Inglis's solution [80] gives near tip stresses that scale as

$$\sigma_{cracktip} \propto \sqrt{\frac{a}{\rho}}. \quad (4.1)$$

Given the discrepancy in the scale between a and ρ , crack tip stresses are dominated by changes in crack opening. For example, a crack of $a = 100\mu\text{m}$ and $\rho = 1 \text{ nm}$ that undergoes 10 nm of dissolution induced advance and opening would experience a decrease in near tip stresses of 70%. Accordingly, the results presented here point to dissolution inducing crack arrest via a blunting phenomenon. This motivates the question of whether dissolution induced opening might eventually cease while dissolution induced crack growth remains active. The simulation results of Figs. 4.5(a)-(c) which extend to 400 cycles do not show any indication of a trend towards this behavior, but it cannot be ruled out.

The inhibition or even arrest of cracks due to environment has been widely observed in the laboratory. In some cases involving structural alloys in aqueous and liquid metal environments, the behavior has been attributed to crack blunting via dissolution [69, 135–139]. However, in no cases could the dissolution mechanism be isolated from other potential mechanisms, e.g. the progressive buildup of corrosion products [163, 164]. Thus, the modeling outcomes presented here together with the available experimental data support the assertion that dissolution can inhibit and even arrest crack growth (in the face of the observed dissolution induced plasticity and plasticity enhanced dissolution). As such, this work motivates the incorporation of dissolution blunting mechanisms into crack growth prognosis (as done by [137]), and suggests that such a mechanism can be included in a load independent formulation.

CHAPTER 5
**ASSESSMENT OF ADDITIVE MANUFACTURING FOR INCREASING
SUSTAINABILITY AND PRODUCTIVITY OF SMALLHOLDER
AGRICULTURE**

5.1 Introduction

More productive and sustainable agriculture is a continuing goal of farmers and consumers across the globe. Innovative approaches that can increase crop yield and sustainability are often coupled to increased mechanization. In the context of smallholder farms, the System of Rice Intensification (SRI) is one example. SRI is an agroecological methodology for increasing the productivity of rice farming by improving the management of plants, soil, water and nutrients. It was developed in Madagascar in the 1980s, and has since spread to over 10 million smallholder farmers in over 50 countries [165, 166].

The adoption of SRI has been constrained by access to mechanical equipment, particularly for transplanting, direct-seeding and weeding operations [167, 168]. The labor requirement of SRI that could be a barrier for adoption is not necessarily intensive once the methods have been learned and mechanization of the operations is implemented [169, 170]. However, most rice farmers in Asia and Africa are smallholder farmers who still depend on manual labor for cultivation. While mechanization for smallholder rice farming has advanced, tools and equipment for SRI farming practices are not yet widely distributed. For many regions where smallholder agriculture is dominant, farming equipment is produced by local metalworkers/blacksmiths that have limited manufacturing resources [166, 171]. Accordingly, equipment with sufficient capability, reliability, and affordability is often unattainable. Rarely can complicated parts be fabricated

locally; thus, innovative equipment development remains isolated and customization based on local conditions is limited.

The emergence of additive manufacturing technology (also known as 3D printing) motivates exploring the extent to which this technology might address SRI mechanization challenges. Compared to traditional manufacturing practices, additive manufacturing (AM) can offer a means to more economically produce low volumes of parts without extensive machinery and infrastructure [172–174]. AM can offer increased customization, reduced waits and costs for replacement parts needed for individualized repairs [175], and the acceleration of the design-prototype-test cycle that ultimately spurs innovation [174]. In this report several AM methods are considered [176], with the majority of focus being directed towards the popular material extrusion 3D printing (ME3DP) approach. The ME3DP method consists of extruding a polymer through a heated nozzle(s) attached to a robotic gantry, allowing a three dimensional object to be autonomously built layer-by-layer.

Although the potential of applying AM technology to agricultural tools has been mentioned in the literature [177–179], the effectiveness of AM technology for addressing the specific needs of real smallholder agriculture communities has not been thoroughly discussed. Due to technological, language, and cultural barriers, useful information on the most important mechanical obstacles for SRI adoption is difficult to obtain and worthwhile of dissemination.

This report summarizes our recent effort to: (1) identify the mechanical obstacles that hinder the adoption of SRI practices for smallholder agricultural entities; and (2) explore the extent to which AM technology can benefit such entities, particularly the ability of AM technology to economically and reliably deliver products of sufficient dimensional precision and mechanical performance. It begins with a summary of our

communications with field partners regarding the mechanical obstacles faced relative to adopting SRI. Then, we assess the potential of AM technology to assist in overcoming these obstacles via two case studies comparing AM costs to traditional manufacturing as has been done in other contexts [180–185]. Some of the printed models were tested in the field for functionality and proof of concept.

5.2 Current mechanical obstacles in SRI adoption

To better understand the mechanization needs of smallholder farms, and more specifically what hinders them from adopting SRI, we managed to interact directly with five field partners. The same questions on the current local state of SRI adoption, the obstacles and mechanical limitations were asked through face-to-face meetings at Cornell, emails, questionnaires, Skype meetings, and site visits with the five partners we worked with - Mr. Asif Sharif from Pakistan; Dr. Debashish Sen from PSI, India; Mr. Yahya Salehuddin from SRI-MAS, Malaysia; Mr. Ousmane Djiré from SOCAFON, Mali; and FEDEAARAZ from Columbia. Responses from our field partners are summarized below.

5.2.1 Lahore, Pakistan

Mr. Asif Sharif is a farmer and innovator from Lahore, Pakistan. His agriculture company in Pakistan is committed to providing science-based solutions and effective alternatives for improving productivity and profitability. Mr Sharif visited Cornell in December 2016, during which time he shared his company’s design, prototyping, and manufacturing process, and the outstanding mechanical obstacles.

In order to maximize yield, precise control of plant-to-plant spacing is vital. This can be accomplished either by directly seeding in the open field, or transplanting plants after they have grown from seed in a controlled environment. Direct seeding is a much less laborious approach, but it cannot be applied to small, delicate, or expensive seed species due to inadequate planting machines available to the smallholder farmer. Selecting an exact number of seeds, especially when seeds have small and/or variable shapes, can be very challenging, e.g. carrot seeds are small and the size and shape of corn seeds vary substantially. Thus, affordable seeders customized to local seed varieties and conditions are needed.

The combination of seed size, seed shape, and local conditions, means that there is a low volume demand for many variations of economical seeding equipment. We infer that this makes the production of such equipment economically unfavorable for large volume agricultural equipment companies. Further, prototyping seeder design is restricted to traditional blacksmith type manufacturing in Mr Sharif's area. He described their manufacturing process as being driven first by physical tinkering, then by designing. Designs that have been successfully demonstrated as a prototype are then produced.

5.2.2 Uttarkhand, India

Dr. Debashish Sen is from PSI – a non-governmental organization (NGO) working on sustainable rice production intensification in the Himalayan region of Uttarkhand State in India. Dr. Dehashish visited Cornell in September 2016. During the meeting and the following email communications, he explained the current situation of SRI mechanization in his region, especially the obstacles hindering the development of equipment that would facilitate farmers' adoption of sustainable rice production practices.

The adoption of SRI requires frequent mechanical weeding [186]. Therefore, adequate access to weeders is crucial for smallholder farmers to implement SRI practices. Moreover, if the weeding operation can be improved, it could be more attractive for farmers to apply SRI methodology. However, in Himalayan region, the number of available weeders is insufficient, e.g. one weeder is shared by about 10 farmers in some areas. Additionally, current SRI equipment designs come from the south of India and are not suited for mountain soil. Ergonomically, available weeders are more suited for use by men (i.e. too high and too heavy), inconsistent with the custom of women often performing the weeding in this region.

The limited quantity of equipment in this area is attributed to a lack of skilled fabricators/welders. Equipment is typically made from plate steel, but there is not a fabricator/welder in every village. Dr. Sen estimated 10km as a typical distance from a village to a fabricator. Therefore, the number of fabricated equipment is restricted and broken equipment is often difficult to repair. As for new designs, local blacksmiths typically cannot fabricate from drawings. They must see a prototype, hindering the spread of new designs.

5.2.3 Selangor, Malaysia

Mr. Yahya Salehuddin is an equipment innovator from the NGO SRI-MAS in Malaysia, who provides leadership for SRI evaluation and innovation in the state of Selangor. We communicated through emails and Skype calls, and he described the major obstacles for SRI mechanization in Malaysia and shared with us his thoughts about modifications of current equipment.

As with our partner in Lahore, Pakistan, better seeding and transplanting machines

are needed in Selangor, Malaysia. Currently, seeding is performed manually, since the locally-made seeders are quite crude – they damage the seeds and don't seed evenly. For transplanting, it is not economical to pay farmers to transplant by hand, and the existing mechanical transplanters often place too many seedlings.

As with our partner in the Himalayan region of Uttarkhand India, Mr. Salehuddin is also looking into mechanizing the weeding process. He is primarily interested in importing motorized weeders (which are often referred to as “Weed Eaters” in the USA) that are mass-produced in China, and modifying them for rice production. A specific example he mentioned involved customized “shoes” around the shaft of the device that is used to better protect rice plants from being damaged by the device during the weeding process.

Mr. Salehuddin was clearly motivated to improve existing equipment for the local requirements of smallholder farmers, but performing such modifications locally appeared to be the constraining factor.

5.2.4 Ségou Region, Mali

Mr. Ousmane Djiré is the technical director of a metal smith company/association in the largest irrigation rice production zone in Mali. His company imports equipment prototypes from Asia and adopts them to local conditions. Currently the company has 17 workshops with 44 blacksmiths. During our Skype call and email communications, Mr. Djiré shared that his most substantial obstacles are similar to those discussed previously, i.e. seeding and weeding.

Mr Djiré is specifically interested in seeders. With SRI, only 1-2 seeds are desired

per hole, but the seeders imported to date and the modifications of them have not yet been able to achieve that goal. Mr Djiré's company does have designs/plans that might potentially address the current shortcomings. However, implementation of the designs appears slow and difficult, likely due to the manufacturing challenges of more complex load bearing parts, such as sprockets.

The manufacturing of a weeder rotor was also mentioned as being a substantial challenge by Mr. Djiré. The rotor of a weeder is the most expensive part to produce, being both time consuming and requiring precise dimensional control. Rotors are currently cut from sheet metal, then welded. Mr. Djiré's company is currently able to make and sell about 200 weeders during rice season. If the manufacturing cost of the weeder rotor can be reduced, weeder price could be reduced, making mechanical weeding more feasible for smallholder farmers.

5.2.5 Bogotá, Columbia

FEDEAARoz is a Colombian national association of rice farming professionals aimed at increasing the productivity and profitability of smallholder rice farmers. We were introduced to the association's achievements and challenges for SRI mechanization when we were invited to attend the Second Regional SRI Conference held in Bogotá, Colombia.

At the Bogotá office of FEDEAARoz, researchers demonstrated to us the limitations of the current seeders and weeders. As with our other partners, current seeders in Columbia cannot fulfill the requirement of SRI (only 1-2 seeds be placed in each hole). The variety of seed sizes and shapes was again pointed to as being central to this challenge. Researchers also shared a problem that they face when transplanting. One part of

the transplanter breaks easily during operation and thus needs to be replaced frequently. The easily broken part is a small load-bearing part with complex geometry that is difficult to be manufactured locally. They were enthusiastic about exploring the possibility of 3D printing technology to provide a solution for this problem.

In contrast to the other partners, access to weeding equipment did not appear to be a problem. However, work is ongoing to improve the design of available weeders. They are particularly interested in designs that can accelerate the weeding process, e.g. combining longitudinal and transverse motion along the rice rows. Their design process is hindered by the prototyping step, as it is time-consuming; and thus, makes the design iteration slow.

5.2.6 Summary of field partner interactions

Due to the wide spread of SRI (remote local communities across the globe) and the language difference between those small farms, information about general mechanical obstacles in SRI adaptations is not easily obtained; thus its discussion is worthwhile despite the deficiencies. Although the number of our partners is not large, they are from either agriculture companies or NGOs that are exposed to many, if not all, smallholder farms in their local areas. Thus, while caution must certainly be taken in generalizing the findings presented here, the data can be interpreted as having been obtained from a substantial number of farmers. Considering the interactions with all partners together, there are two clear mechanization obstacles shared by smallholder farmers across the globe: (1) the lack of capability to design and manufacture direct seeders that are suitable for the particulars of local seeds and conditions, and (2) the limited availability of appropriate weeders due to cost and/or reliable local manufacturing. This motivated

the subsequently presented study of seeders and weeders typical to smallholder agricultural. In this project, we focused on key components of the seeder and weeder, i.e. the roller of a Jang JP-1 push seeder (Figure 5.2) and the rotor of a Mandava weeder (Figure 5.5). The two objects are both printable and important to the successful implementation of SRI in smallholder rice farming, yet substantially different with regard to size and mechanical demands (Figure 5.1). The roller is the component of the JP-1 seeder that selects/singulates seeds. It is key to the success of a seeder for particular seeds and local conditions. It is small in size, can be printed by most ME3DP printers, and is not subjected to significant mechanical loading. The rotor of the weeder is a larger part and is the most geometrically complex part of the weeder. Its function requires it to regularly sustain significant mechanical loading. Accordingly, the rotor represents a bottleneck in local manufacturing and reliability of weeders customized to local conditions. Due to its size, the rotor can only be printed on machines with relatively large build platforms.

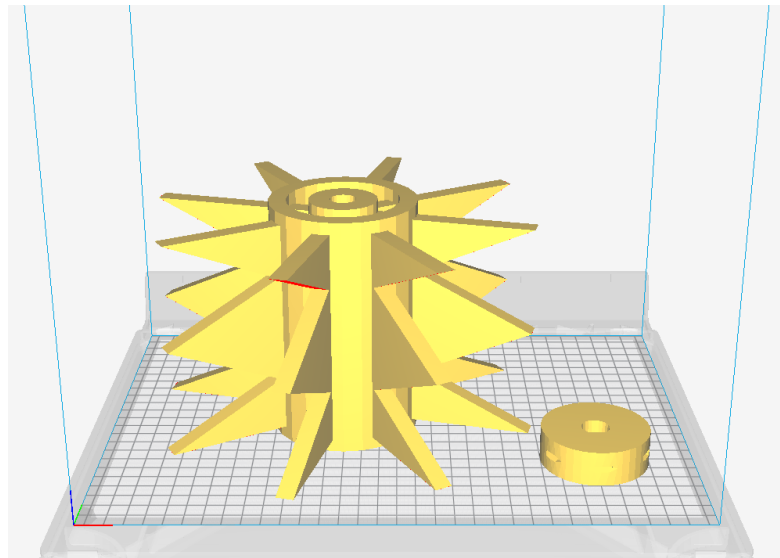


Figure 5.1: Computer models of the two components studied in this report: Mandava weeder rotor (left) and the Jang JP-1 push seeder roller (right). For scale, the square grid spacing represents 1cm.

5.3 Case 1: Jang JP-1 push seeder roller

As discussed in Section 2, a direct push seeder that can singulate and distribute seeds is of particular interest to smallholder farmers. However, from our survey of smallholder rice farmers, it appears that equipment capable of satisfying the SRI requirements of spacing between seed holes and the number of seeds per hole is not generally available. Motivated by this, innovative 3D models of the roller component for a prototypical push seeder, i.e. the Jan JP-1 (Figure 5.2), were designed at Cornell University using AutoCAD, and the unit cost of fabricating the roller was then examined. The costs associated with two tasks critical to SRI mechanization success were assessed: (1) fabricating functional prototypes during the design process, and (2) a low-volume production run. For design prototyping, we considered the case where 5 prototypes of differing geometries would be required to complete 5 design-build-test cycles and arrive at a final functional product design, $n_{prototypes} = 5$. For the low-volume production run, we considered the fabrication of 100 identical units, i.e. $n = 100$.

There is extensive literature on costing models of AM. Many focus on large-volume manufacturing from the business point of view, where they assume large numbers of identical parts are printed in the period of one year[180–185]. However, for smallholder farmers who are both the manufacturer and the consumer, their needs include rapid prototyping to adjust equipment to local conditions and low-volume manufacturing which could be as low as a few customized pieces with the ME3DP method. Thus, a simplistic costing model that focuses on the ME3DP and can also applied to other AM methods and traditional manufacturing methods is needed. Considering the production volumes associated with local smallholder agriculture needs, typical fabrication routes require an appreciable initial investment cost, $C_{investment}$, which is independent of the number of identical parts to be produced, n . Thus, the total cost per unit, C_{total}^{unit} , is a function of n .

To allow a one-to-one cost comparison, we have utilized a basic cost model

$$C_{total}^{unit} = C_{investment}/n + C_{direct}^{unit}, \quad (5.1)$$

where C_{direct}^{unit} represents the component of C_{total}^{unit} that is independent of the number of parts produced.



Figure 5.2: The Jang JP-1 push seeder which was recommended by our partner in Pakistan. Zoomed images show the roller component that was studied in section 3 and printed using ME3DP thermoplastic.

5.3.1 Traditional fabrication

Cost estimates were obtained for local roller fabrication from two of our field partners. Our Mali partner communicated that fabricating the roller locally by metalworkers/blacksmiths would be the most feasible approach in his setting. Although, he did express concern that the dimensional precision of the final product might be insufficient for the desired function. From our communications, the tooling required prior to production was unclear, e.g. jig creation. Thus, for simplicity, the total estimated unit

cost, $C_{total}^{unit} = \$26.60$, is assumed to entail no investment cost. In contrast, our Pakistani partner considered nylon injection molding to be the most feasible fabrication route to obtain a customized roller locally. In this case, dimensional precision is not expected to be a concern for the roller application. The partner estimated $C_{investment} = \$1,000$ for mold creation and $C_{direct}^{unit} = \$2.00$. This magnitude of investment cost is problematic for small production volumes, which are specifically where the smallholder agriculture need exists (emphasizing that the performance of the roller is governed by its sensitivity to local seed characteristics and conditions).

To provide context, quotes were also obtained for traditional fabrication of the roller in the United States. After discussion with a senior machinist at Cornell University, we concluded that computer numerical control (CNC) machining and injection molding would be the most typical routes for fabricating the roller component in the United States. Cost estimates were subsequently obtained from two U.S. companies (ICOMold and 3D Hubs) for both CNC and injection molding approaches. Two common thermoplastic materials (nylon and ABS) were considered. Prices for prototyping (i.e. $n = 1$ for each of the 5 iterations) and low-volume manufacturing (i.e. $n = 100$) are given in Table 5.1 along with the estimates obtained from the field partners. The costs for prototyping were inferred from single and multiple unit costs following equation 5.1. All prototyping unit costs were calculated with $n = 1$, given that investment costs would reoccur when producing an altered design, e.g. new jig or mold, other than for the ME3DP method where the printer investment cost is only required for the very first print (i.e. printer purchase and setup). Conclusions will not be affected for a greater number of iterations. While the most mechanically efficient geometries of the roller are a function the properties of the material that comprise it, this aspect is neglected here as mechanical performance is not key to the functionality of this roller, simplifying analysis.

Table 5.1: Unit cost of producing different numbers of rollers for the JP-1 seeder via various fabrication methods (information obtained from field partners in April 2018 and from U.S. companies in April 2019). The prototyping unit cost was calculated from the initial investment cost and the fixed direct unit cost only, without considering the possibility of subsequent production volumes.

Field partner/ U.S. supplier	Method	Material	Prototyping unit cost ($n = 1$) ($n_{iteration} = 5$)	Production unit cost ($n = 100$)
Segou Region, Mali	Plate cutting, bending, welding	Aluminum	\$26.60	\$26.60
Lahore, Pakistan	Injection molding	Nylon	\$1002.00	\$12.00
ICOMold, U.S.	Injection molding	Nylon	\$4554.26	\$47.52
ICOMold, U.S.	Injection molding	ABS	\$4402.16	\$45.10
3D Hubs, U.S.	CNC	Nylon	\$195.00	\$26.20
3D Hubs, U.S.	CNC	ABS	\$195.00	\$26.41
3D Hubs, U.S.	ME3DP	PLA	\$35.00	\$7.70
Cornell, U.S.	ME3DP (printer needed)	PLA	\$154.33	\$8.92
Cornell, U.S.	ME3DP (printer existing)	PLA	\$19.43	\$1.45
Jang JP Seed Roller N-6	commercially available product	Plastic	\$31.00	\$31.00

5.3.2 Additive manufacturing cost

A simplified costing model, inspired from the literature [180–185] is key to assessing the utility of the examined fabrication routes. As shown in equation 5.1, total cost per unit is computed from the independent investment cost, $C_{investment}$, which includes the machine cost and the labor cost during the setup and tuning period, and the direct unit cost, C_{direct}^{unit} , which consists of the material and labor costs involved in the activities during the manufacturing process. The simplified model enables information to be inferred from the obtained quotes, so that comparisons can be made.

Currently, the ME3DP additive manufacturing method typically requires an initial investment of ~\$100 to ~\$10,000 to acquire a printer[187]. A QIDI TECH I Dual Extruder Desktop 3D Printer (Figure 5.3) was used here for the cost analysis, a choice motivated by our positive experience with this particular machine. The QIDI TECH I is among the more affordable ME3DP printers, costing ~\$600, while still providing relatively high quality builds on a reasonable build platform (230x150x150 mm).

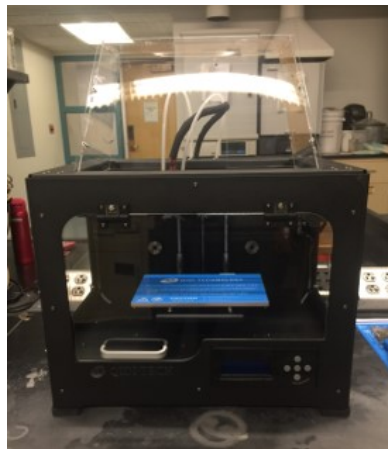


Figure 5.3: The ME3DP printer used in this project - QIDI TECHNOLOGY 3DP-QDA16-01 Dual Extruder Desktop 3D Printer, bought in September, 2016.

Table 5.2: Model variables and values for AM cost estimation.

Variable	Value
$C_{material}$	\$0.70
$C_{printer}$	\$638.20
R_{labor}	\$36.32/hour
$T_{assembly/calibration}$	3 hours
$T_{digitization}$	0.5 hours
$T_{bed_cleaning}$	10 seconds/part
$T_{part_removal}$	30 seconds/part
$T_{filament_loading}$	16.67 seconds/part

For the ME3DP unit cost estimate, $C_{investment}$ was considered to be the cost of purchasing the printer, the labor for printer assembly and calibration, and the labor for creating the printer instructions via a slicing program and tuning the printing parameters. The cost of digitally drawing the design was not included as that would be identical among all the digital fabrication approaches. Considering labor costs to be the product of a labor rate and time, the investment cost can be expressed as

$$C_{investment} = C_{printer} + R_{labor} * (T_{assembly/calibration} + T_{digitization}). \quad (5.2)$$

Values of the above parameters estimated from our ME3DP printing experience are listed in Table 5.2. A labor rate of \$36.32 per hour was used, which is the average employer cost for employee compensation reported by the U.S. Bureau of Labor Statistics [188] for December 2018. For reference, this corresponded to an average wage of \$24.91 per hour, significantly above the current minimum wage in New York State, \$11.10/hour [189]. Note that the labor cost listed here was based on performing the work at Cornell University, which may be different from other settings. Nonetheless, comparison with similar commercial goods suggests that the estimates used here are indeed reasonable.

Both material and labor costs contribute to C_{direct}^{unit} . To simplify, it was assumed that there are no unsuccessful prints during the manufacturing process after the initial tuning

period, and the labor required for printer maintenance is neglected since the time period for both the prototyping and the low-volume production process is relatively short. Considering PLA, a common thermoplastic for ME3DP, the filament cost for this project was \$29.11 per kg, or \$0.70 per roller. While in practice, a thermoplastic other than PLA, e.g. ABS or nylon, might be used, this would not change the conclusions of the cost analysis. Considering the dimension of the roller and the printing space of the ME3DP printer, 6 rollers can be simultaneously printed, reducing C_{direct}^{unit} [190]. Between subsequent prints, the completed rollers must be removed from the print bed and the print bed must be prepared/cleaned for the next print. From our experience, this task could be done at an average rate of 15 times per hour. Additionally, a new roll of filament must be loaded into the printer every 36 rollers, a task assumed to require 10 minutes of labor. Thus, 0.94 minutes of labor is required per roller. The direct unit cost is \$1.27 with 45% of that value being labor costs, following

$$C_{direct}^{unit} = C_{material} + R_{labor} * (T_{part_removal} + T_{bed_cleaning} + T_{filament_loading}). \quad (5.3)$$

Table 5.1 gives the per unit total costs for the prototyping and production examples. Two cases are discussed for ME3DP method – “printer needed” and “existing printer”. The first case considers when a new ME3DP printer must be purchased and the second case considers when a printer has been purchased and shared within a community. The unit cost for 100 pieces was examined considering this to represent a production volume that might be associated with delivering a roller tailored for conditions specific to a smallholder agriculture community. The cost difference between the prototyping and production cases for ME3DP is due to the initial machine and/or labor investment before the first print of a viable prototype, such as machine purchase, printer tuning, model slicing, and parameter setting, which is independent of the number of prints and

thus dominates the prototyping cost (where $n=1$). For large n , multiple parts can be printed by the same printer at the same time, and also since they are identical, the same code can be used for many times, and thus, the unit cost is decreased. In the case when a printer is purchased for the specific need, the capital cost for printer purchase is included in $C_{investment}$; while in the existing printer case, the cost of purchasing a printer was neglected, and $C_{investment}$ only considered the labor investment for one-off setup. As might be expected, the most expensive approach of those considered is outsourced injection molding within the United States. Outsourced CNC fabrication within the United States is significantly less expensive at $n = 100$, and is comparably priced with the cost estimate provided by our Mali partner for local metal fabrication. The injection molding estimate provided by our Pakistani partner is the most economically appealing of the traditional fabrication approaches but is above the ME3DP fabrication routes. Purchasing a ME3DP printer to produce 100 identical rollers appears to be the most cost effective. The delivery time associated with the ME3DP process is similar with all other methods, estimating that the fabrication of an aluminum roller in Mali might be 3hr/part and that injection molding time in Pakistan will be comparable to the United States.

For prototyping, the costs associated with mold fabrication make standard injection molding a noncompetitive option (Table 5.1). Outsourced CNC fabrication is substantially lower in cost, yet it is still significantly above the cost of outsourced ME3DP fabrication. Even if ME3DP is done locally and requires the purchase of a printer solely for fabricating the prototypes, we estimate the cost to be below that of outsourced CNC fabrication. When a ME3DP printer is available onsite, this presents the best route for prototyping, especially when considering that single prototype rollers can be printed in a few hours as opposed to the multiple business day turnaround time offered by the outsourced fabrication routes.

The retail cost of a similar commercial product that is designed for small to medium-size seeds is listed in Table 5.1 for reference. It can be seen that fabrication via both ME3DP and the local metal shop are economically advantageous for both prototyping and production scenarios.

Prototyping using the local metal shop in Mali is appealing for both cost and delivery time, provided the required dimensional precision can be obtained. For the printed rollers using our ME3DP printer, we measured the overall width and height of 3 successive prints. The dimension precision is 100.7% in the direction perpendicular to the building axes and 105.3% in the direction parallel to the building axes. Although the 5% dimensional precision error could have been reduced through calibration procedures, effort was not devoted towards this goal, given that no practical difficulty arose from the fit of the roller into the seeder. The value of precision may drop for small features like the holes on the perimeter of the roller due to the limits of the layer height and track width that are inherent in the ME3DP manufacturing method. Other factors like the thermal distortion during the printing process may also affect the precision of the final part.

As a proof of concept, we conducted four design-build-test cycles that involved 14 distinct designs having different shaped and/or dimensioned holes for rice seeds to be singulated. Three roller designs were tested on tilled soil during the final prototyping cycle. The average number of seeds deposited per hill for the final design approached the goal of unity, i.e. 1.6 seeds per hole, with a standard deviation of 1.0. Considering that the initial design (with a seed hole size of 1.5 times the seed width) did not distribute any seeds, the progress made over the four prototyping cycles supports the assertion that by facilitating design-build-test cycles under local conditions, ME3DP technology can aid in the design of seeders that are more capable of meeting the local challenges of SRI adoption. On this point, we note that additional opportunities for improving

seeder performance (beyond roller design) were identified during the prototyping cycles that could be harnessed in an actual application. The design iterations performed to date were inspired from field test results. To facilitate further improvement beyond the publication date of this manuscript, the designs have been uploaded to an online 3D printing community¹.

The proof of concept testing illustrated that the ME3DP used here produces rollers of sufficient dimensional accuracy, strength, wear resistance, and surface finish to fulfill its function, at least for the duration of prototype testing. Fatigue and wear performance for actual application durations, beyond prototyping were not assessed.

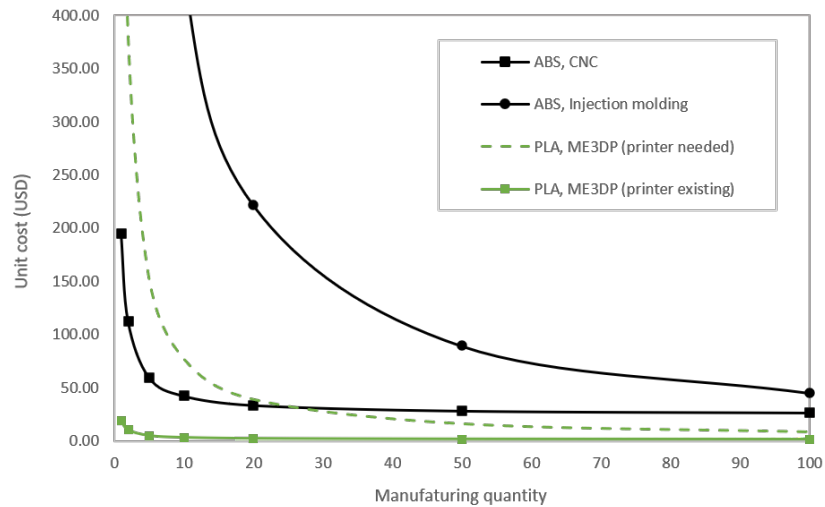


Figure 5.4: Unit cost of the JP-1 seeder roller for different fabrication methods. Curves were plotted from equation 5.1 with parameters obtained by fitting the model to obtained quotes.

¹Studied cases and related models have been shared for reference and/or future development: <https://www.thingiverse.com/guwenjia0929/collections/seeder-roller-and-weeder-rotor-models>.

5.4 Case 2: Mandava weeder rotor

The rotary weeder is another important ingredient for the successful adoption of SRI [165], and the rotor is a key component of the weeder. Relative to other components, the rotor is the most challenging component to fabricate and often governs the failure of existing weeders. The rotor requires high dimensional precision, mechanical strength, and decent wear resistance (Figure 5.5), motivating the selection of the Mandava weeder rotor as a case study. Drawings of the weeder rotor were provided by Earth Links, a non-profit environmental organization, and the designs of the model were evolved from the existing rotors on the market.

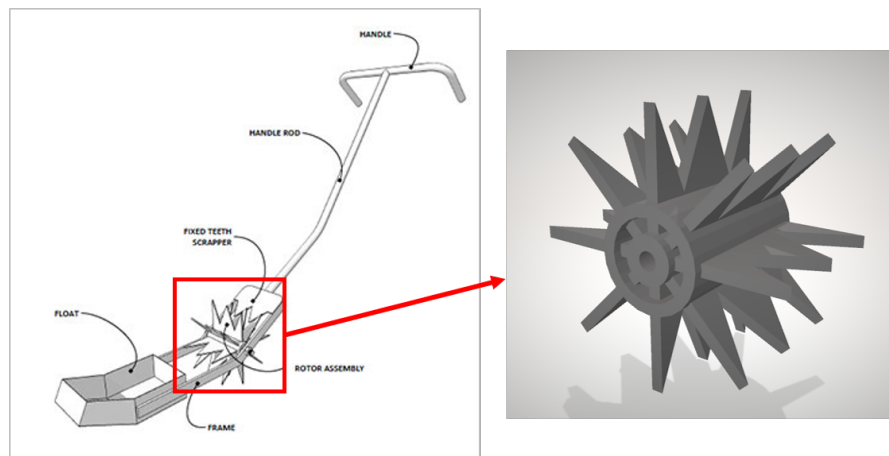


Figure 5.5: Sketch of the Mandava weeder developed by an Indian farmer. It is widely used due to its lighter weight. The zoomed view shows a 3D model of the rotor of the Mandava weeder which is the most geometrically complex part of the weeder. Drawings were provided by Earth Links, Inc.

5.4.1 Traditional fabrication cost

Several estimates of the cost for traditional fabrication of the Mandava weeder rotor were obtained. Mr. Djiré provided details on a common fabrication process in Mali,

involving the bending, cutting, and welding of steel sheet. His estimated costs for this local fabrication route are given in Table 5.3. According to Mr. Djiré, a key challenge is that the dimensions of the final product are not controlled adequately, often inhibiting assembly and/or functionality. Furthermore, the manufacturing time is longer than desired, restricting the availability of such products when considering the number of qualified labors and available tools.

Fabrication of the rotor in the U.S. was also examined. First, quotes from two independent machine shops on the Cornell University Ithaca campus were obtained. Similar to Mr. Djiré's estimate, the Cornell estimates were associated with a fabrication route that involved cutting, bending, and welding sheet steel. The estimates were partitioned into labor and material costs, with the majority of expense being associated with labor. As shown in Table 5.4, the labor cost is as much as 96 percent of the total cost. The labor cost associated with initial setup and tooling, was estimated for producing two quantities of rotors, i.e. 1 and 10. From equation 5.1, the initial setup and tooling costs, $C_{investment}$ is estimated to be 116.5 and 95.9 percent of C_{direct}^{unit} for the two traditional manufacturers, respectively. Practically, this equates to the total cost per part becoming approximately constant when production volume exceeds 10 parts. Considering the costs in Table 5.3, the estimates given by the three entities do seem consistent, keeping in mind that the end products may differ due to quality of materials, training of the machinist, and access to high performance tools and distribution networks. The current local fabrication approach of Mr. Djiré is justified when considering the traditional manufacturing cost of the roller in the U.S. together with the cost of distributing small quantities of parts to remote locations, as shown for a specific example in Table 5.5.

Table 5.3: Unit cost of producing the Mandava weeder rotor via various fabrication methods. The quotes were obtained from field partners in April 2018 and from U.S. machine shops in February 2018. Quotes for additive manufacturing were obtained in June 2018. LASSP and CEE machine shops are both on the Cornell Ithaca NY campus.

Field partner U.S. supplier	Method	Material	Prototyping unit cost (n=1) ($n_{iteration} = 5$)	Production unit cost (n=100)
SOCAFON, Mali	Cutting, bending, welding	Steel sheet	\$17.70	\$17.70
CEE machine shop	Cutting, bending, welding	Steel sheet	\$722.61	\$337.61
LASSP machine shop	Cutting, bending, welding	Steel sheet	\$737.61	\$380.11
3D Hubs	ME3DP	PLA	\$125.34	\$123.60
3D Hubs	ME3DP	Nylon	\$294.69	\$290.98
Shapeways	Selective Laser Sintering	Aluminum	\$8714.73	\$8714.73
Kraftwurx	Selective Laser Sintering	Stainless steel	\$22040.73	\$22040.73
Shapeways	Binder jetting	Stainless steel	\$4641.40	\$4641.40
Ponoko	Binder jetting	Stainless steel	\$13250.35	\$13250.35
Estimated Quote	WAAM	Mild steel	\$398.66	\$272.81

Table 5.4: Manufacturing cost breakdown of producing one Mandava weeder rotor at two Cornell University machine shops in Ithaca, U.S. (quotes obtained in February 2018).

Machine shop	Unit cost (n=1)		Unit cost (n=10)	
	Labor cost	Material cost	Labor cost	Material cost
CEE machine shop	\$700	\$22.61	\$350	\$22.61
LASSP machine shop	\$715	\$22.61	\$390	\$22.61
		Total cost	Total cost	Total cost
		\$722.61	\$737.61	\$372.61
				\$412.61

Table 5.5: Shipping cost of 50 rotors from the U.S. (quotes obtained in April 2019).

Destination	Air freight cost	Estimated time
India	\$456	7-10 business days
Mali	\$575	7-10 business days

5.4.2 Additive manufacturing cost

Considering the mechanical and wear demands on the rotor together with the properties of AM polymers [191, 192], metal AM was of primary consideration. A very popular approach to produce metal parts of high dimensional and mechanical quality is powder bed fusion (PBF) [193–195]. Considering that typical metal PBF machines currently cost well over \$100,000, outsourcing PBF fabrication is common. Cost estimates associated with outsourcing PBF fabrication of the rotor within the United States were over an order of magnitude more expensive than traditional manufacturing (Table 5.3).

A more economic metal AM approach involves using the wire fed gas metal arc welding process under robotic control [196–204] and is referred to as the wire arc additive manufacturing process (WAAM). While WAAM machines can be built for as little as \$2,000 [196], they generally cost between tens and hundreds of thousands of dollars. Thus, like with PBF, outsourcing WAAM fabrication is most appealing for low volume small holder agriculture applications. While we were unable to obtain an official quote for WAAM fabrication of the rotor, we were able to obtain the information necessary to speculate [205, 206]. An investment cost, $C_{investment}$, of 3.5 hours labor setup time is estimated. The direct unit cost, C_{direct}^{unit} , is estimated to involve 2 hours of WAAM machine usage at an estimated rate of \$95/hr. C_{direct}^{unit} also entails an hour of labor and \$45 of material. This corresponds to the use of mild steel welding wire to create the same rotor geometry as would be made via traditional manufacturing from sheet steel. For consistency, the labor rate used in the previous sections was used for the WAAM labor rate, \$36/hr. With these assumptions, outsourced WAAM fabrication of the rotor is almost a

factor of 2 more economical than traditional manufacturing in the U.S. for single unit production, and of similar cost beyond 10's of units (Figure 5.6 and Table 5.3).

Proof of concept testing was not performed with the rotor, but given its function and steel construction, surface finish, and strength and wear performance are not expected to be problematic. Of greatest concern is dimensional accuracy and fit with the weeder, considering that the length scale of residual stresses associated with the WAAM build process can cause deformation. It is likely that such challenges could be addressed, but this would entail an increased cost that was not considered here, e.g. building with supports.

It is also worthwhile to estimate the cost of fabricating the rotor with ME3DP technology. ME3DP technology is capable of producing fully metal parts via the extrusion of metal-infused thermoplastic filaments followed by furnace sintering [207]. However our experience with this technology suggests that further development is needed prior to gaining the capability to produce parts of sufficient mechanical performance and dimensional accuracy.

A second motivation to consider ME3DP construction of the rotor is that, dramatically different rotor designs accessible to AM fabrication may provide sufficient performance with current technology, e.g. poly carbonate filament. Such novel designs might be further enhanced by the use of coatings to provide sufficient wear performance. Complementing this is the point that for prototyping purposes, fatigue and wear performance of current technology may be sufficient for identifying rotor designs best suited for local conditions, e.g. soils characteristics and ergonomics.

Given that the dimensions of the rotor exceed the work space of our ME3DP printer and many other low-cost ME3DP printers, outsourced ME3DP fabrication costs for the

rotor were obtained. As expected, the outsourced ME3DP costs are the most economical of the AM approaches considered (Table 5.3). The cost difference between two ME3DP quotes is due to the chosen material, which results in different filament costs, printer temperature requirements, printer tuning time, etc. As discussed previously, there is a difference between the prototyping and production unit costs, but the difference is much smaller than in the previous case of the roller. This is because the rotor is larger in size, such that there can only be one rotor printed per build. Thus the labor costs per part of printing one-offs is more similar to that for printing large numbers, than it is for the roller. Altering the rotor design to consist of several smaller interlocking pieces might allow for the use of more typical low-cost ME3DP printers, via the reduction in the size of the required print bed.

Other possible implementations of low cost ME3DP for metal printing might involve using ME3DP to print patterns for investment casting, either directly or indirectly by printing a master pattern to make a silicone rubber mould to make investment patterns [208, 209]. Alternatively, ME3DP can be used to print molds with higher melting temperature thermoplastics that could be used for injection casting lower melting temperature thermoplastics [210]. We requested quotes from several 3D printing assisted metal casting service providers, but they were unable to provide cost estimations due to the dimension of this rotor. Thus, the potential of these technologies has been left for future work.

5.5 Summary and Conclusion

This project began by identifying dispersed field partners who could share their knowledge of local obstacles hindering the adoption of SRI practices. To our knowledge,

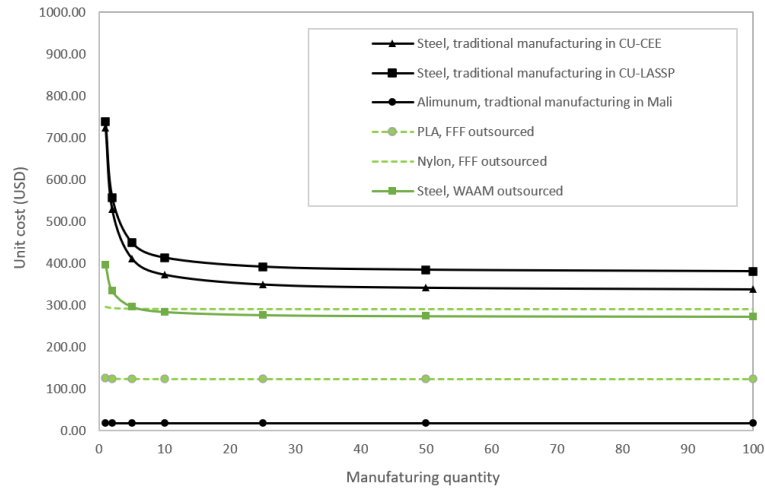


Figure 5.6: Unit cost of the Mandava weeder rotor via different manufacturing methods.

such information has not been collected before, and thus provides an important stepping stone towards the goal of broader SRI adoption. Through the reported discussions, two prevailing mechanization obstacles were identified: (1) the lack of capability to design and manufacture direct seeders that are suitable for the particulars of local seeds and conditions, and (2) the limited availability of appropriate weeder due to cost and/or reliable local manufacturing.

Specific components were identified as the source of each obstacle, i.e. the roller in a push seeder (which singulates and places seeds at the required spacing) and the rotor in a push weeder (which is the part in contact with the ground). Focusing on the ME3DP method for prototyping and low-volume production runs, a simplified costing model was built to infer the cost curve from the obtainable information. Costs for manufacturing these two components in the U.S. and in the field were studied and compared. The acquired data and the following field test suggests that ME3DP technology can rapidly provide functional rollers for seeders and be economically advantageous in the small-holder agriculture setting, where several design prototypes and low-volume production

runs are needed.

The second case study consisted of the rotor component of a push weeder. In this case (as currently designed) thermoplastics may provide insufficient mechanical performance, thus limiting the application of established ME3DP technology to short duration prototype tests. While powder bed fusion metal approaches are capable of producing rotors of sufficient characteristics to perform their function, the cost of such fabrication technology is prohibitive. Thus, wire arc additive manufacturing (WAAM) was considered and shown to be an economically attractive approach relative to traditional fabrication in the US. With that said, fabrication in the field by traditional approaches remains economically superior for low volume production. This outcome is a result of the requirement that the rotor must sustain substantial loads and resist wear to function effectively, yet is not a part requiring high dimensional precision.

Considering the clear benefit that ME3DP can offer when it can be effectively used, as demonstrated here for the roller, plenty of motivations exist to advance this technology so that higher performance ME3DP parts can be produced. There are a myriad of routes for attaining this goal, e.g. (1) the extension of ME3DP technology to metal alloy parts of sufficient load bearing capacity and wear resistance; (2) the improvement of the thermoplastic materials on which ME3DP printing currently relies; and perhaps most promising in the near term (3) the identifying designs capable of harnessing ME3DP technology in its current state or with small modifications, e.g. coatings. For example, one might envision modifying the design of the rotor to reduce stresses and wear by utilizing the wider geometric design space offered by AM, while also examining the exciting possibility of designs with improved functionality that might have been previously unattainable with the traditional manufacturing routes that have been relied upon to this point.

CHAPTER 6

CONCLUSION AND FUTURE WORK

In summary, through the presented work in this thesis we are able to shed light on the atomistic-scale mechanisms governing fatigue crack growth in vacuum and the role of material dissolution on the crack tip in the context of environmentally assisted cracking, while making an effort to apply acquired scientific principles and resources to solve actual problems in the field. The promising finding of the mechanism for fatigue crack growth at the atomic scale that can be simulated by our concurrent multiscale model opens the door for future investigations to improve the modeling and prediction of the fatigue crack in real life.

In order to further understand the applicability of the uncovered mechanism, parametric studies would be the next steps. Attempts have been made to study the isolated effect of surface energy on fatigue crack behavior via modification of the intrinsic ductile potentials. However, interpretation of the current results and implementation of the modified potentials may need further analysis and exploration. Aside from continuous investigations on the surface energy which is considered a less controlling parameter, studies could also be carried out to examine other variables such as the stacking fault energies, elastic constant and strength of the material, to name a few. Ultimately, efforts should be made to relate fatigue crack growth tendency to fundamental material properties through systematical parametric studies.

While studies of fatigue crack in vacuum are of significant importance, understanding of environmentally assisted cracks are of equal value from a practical point of view. Environmental effects on fatigue crack growth might come from many mechanisms. Compared with material dissolution that has been studied, hydrogen embrittlement and oxide layer formation due to presence of water molecules seem to have larger impacts

over the growth of fatigue crack in real environments. Thus, it would be worthwhile to build upon our current multiscale model and expand its capability to simulate interactions between Hydrogen atoms and fatigue surfaces, and also study crack behaviors in the presence of oxide layers. Comprehensive analysis should also include fatigue crack growth simulations in accordance with different H₂O exposure levels, as hydrogen embrittlement and oxide layer formation could have different mechanisms at different exposure levels resulting in different fatigue crack growth behavior.

As introduced at the beginning of the thesis, material separation processes consist of not only crack propagating but also crack initiation. It is acknowledged that nucleation and growth of a crack to a detectable size accounts for most of the cracking process. The newly implemented model can also be utilized to uncover key mechanisms governing the associated fatigue crack initiation process. Inspired by our recent work about the role of dissolution on crack growth, we can continue to study the effect of dissolution on crack initiation adopting a similar strategy, which may provide some fresh perspectives about the critical pit-to-crack transition process. To connect to the realistic contexts, a next step might be to simulate crack initiation from a corrosion pit across a wide range of H₂O vapor exposures,

Finally, based on all results obtained through the completed and proposed work as well as available experimental data, it would be of great engineering importance to develop microscopic material separation laws consistent with the discovered governing mechanisms. And from a broader perspective, utilizing these laws to improve and/or validate existing macroscopic fatigue prediction frameworks would be the ultimate objective of the studies presented in this thesis.

BIBLIOGRAPHY

- [1] VP Rajan, DH Warner, and WA Curtin. An interatomic pair potential with tunable intrinsic ductility. *Modelling and Simulation in Materials Science and Engineering*, 24(2):025005, 2016.
- [2] Michael D Sangid. The physics of fatigue crack initiation. *International journal of fatigue*, 57:58–72, 2013.
- [3] A. K. Das. *Metallurgy of Failure Analysis*. McGraw-Hill Professional, 1997.
- [4] Richard Palmer Reed. *The economic effects of fracture in the United States*, volume 647. US Department of Commerce, National Bureau of Standards, 1983.
- [5] M Shenoy, J Zhang, and David L McDowell. Estimating fatigue sensitivity to polycrystalline ni-base superalloy microstructures using a computational approach. *Fatigue & Fracture of Engineering Materials & Structures*, 30(10):889–904, 2007.
- [6] JR Mayeur and DL McDowell. A three-dimensional crystal plasticity model for duplex ti–6al–4v. *International journal of plasticity*, 23(9):1457–1485, 2007.
- [7] DL McDowell and FPE Dunne. Microstructure-sensitive computational modeling of fatigue crack formation. *International journal of fatigue*, 32(9):1521–1542, 2010.
- [8] JD Hochhalter, DJ Littlewood, MG Veilleux, JE Bozek, AM Maniatty, AD Rollett, and AR Ingraffea. A geometric approach to modeling microstructurally small fatigue crack formation: Iii. development of a semi-empirical model for nucleation. *Modelling and Simulation in Materials Science and Engineering*, 19(3):035008, 2011.
- [9] Michael D Sangid, Hans J Maier, and Huseyin Sehitoglu. An energy-based microstructure model to account for fatigue scatter in polycrystals. *Journal of the Mechanics and Physics of Solids*, 59(3):595–609, 2011.
- [10] Franz Oswald Riemelmoser, Peter Gumbsch, and Reinhard Pippan. Dislocation modelling of fatigue cracks: an overview. *Materials transactions*, 42(1):2–13, 2001.
- [11] VS Deshpande, A Needleman, and E Van der Giessen. Scaling of discrete dislocation predictions for near-threshold fatigue crack growth. *Acta Materialia*, 51(15):4637–4651, 2003.
- [12] S Groh, S Olarnrithinun, WA Curtin, A Needleman, VS Deshpande, and E Van der Giessen. Fatigue crack growth from a cracked elastic particle into a ductile matrix. *Philosophical Magazine*, 88(30-32):3565–3583, 2008.

- [13] WA Curtin, VS Deshpande, A Needleman, E Van der Giessen, and Mathias Wallin. Hybrid discrete dislocation models for fatigue crack growth. *International journal of fatigue*, 32(9):1511–1520, 2010.
- [14] R Pippan, C Zelger, E Gach, C Bichler, and H Weinhandl. On the mechanism of fatigue crack propagation in ductile metallic materials. *Fatigue & Fracture of Engineering Materials & Structures*, 34(1):1–16, 2011.
- [15] George R Irwin. Analysis of stresses and strains near the end of a crack traversing a plate. 1997.
- [16] Harold M Westergaard. Bearing pressures and cracks. *Trans AIME, J. Appl. Mech.*, 6:49–53, 1939.
- [17] ME Fine and RO Ritchie. Fatigue-crack initiation and near-threshold crack growth. *Fatigue and microstructure*, pages 245–278, 1979.
- [18] Campbell Laird. Mechanisms and theories of fatigue. *Fatigue and microstructure*, pages 149–203, 1979.
- [19] Mirko Klesnil and P Lukác. *Fatigue of metallic materials*, volume 71. Elsevier, 1992.
- [20] Robert O Ritchie. Influence of microstructure on near-threshold fatigue-crack propagation in ultra-high strength steel. *Metal Science*, 11(8-9):368–381, 1977.
- [21] RG Forman. Study of fatigue crack initiation from flaws using fracture mechanics theory. *Engineering Fracture Mechanics*, 4(2):333–345, 1972.
- [22] D Eylon and CM Pierce. Effect of microstructure on notch fatigue properties of ti-6al-4v. *Metallurgical Transactions A*, 7(1):111–121, 1976.
- [23] M Makkonen. Predicting the total fatigue life in metals. *International Journal of fatigue*, 31(7):1163–1175, 2009.
- [24] S M Ohr. An electron microscope study of crack tip deformation and its impact on the dislocation theory of fracture. *Materials Science and Engineering*, 72:1–35, 1985.
- [25] G. M. Bond, I. M. Robertson, and H. K. Birnbaum. The influence of hydrogen on deformation and fracture processes in high-strength aluminum alloys. *Acta Metallurgica*, 35(9):2289–2296, 1987.
- [26] S. Lynch. Some fractographic contributions to understanding fatigue crack growth. *International Journal of Fatigue*, 104:12–26, 2017.
- [27] Y. Murakami. *Metal fatigue: effects of small defects and nonmetallic inclusions*. Elsevier Science Ltd, 2002.
- [28] U. Zerbst, M. Vormwald, R. Pippan, H. P. Gänser, C. Sarrazin-Baudoux, and

- M. Madia. About the Fatigue Crack Propagation Threshold of Metals as a Design Criterion - a Review. *Engineering Fracture Mechanics*, 153(November 2014):190–243, 2016.
- [29] R Wang, H Mughrabi, S McGovern, and M Rapp. Fatigue of copper single crystals in vacuum and in air i: Persistent slip bands and dislocation microstructures. *Materials Science and Engineering*, 65(2):219–233, 1984.
- [30] Yunjo Ro, Sean R Agnew, and Richard P Gangloff. Effect of environment on fatigue crack wake dislocation structure in al-cu-mg. *Metallurgical and Materials Transactions A*, 43(7):2275–2292, 2012.
- [31] JT Burns, JJ Jones, AD Thompson, and JS Warner Locke. Fatigue crack propagation of aerospace aluminum alloy 7075-t651 in high altitude environments. *International Journal of Fatigue*, 106:196–207, 2018.
- [32] SGFRO Suresh, GF Zamiski, and D RO Ritchie. Oxide-induced crack closure: an explanation for near-threshold corrosion fatigue crack growth behavior. *Metallurgical and Materials Transactions A*, 12(8):1435–1443, 1981.
- [33] I-Hsuang Lo and Wen-Ta Tsai. Effect of selective dissolution on fatigue crack initiation in 2205 duplex stainless steel. *Corrosion science*, 49(4):1847–1861, 2007.
- [34] RJ Zamora, KL Baker, and DH Warner. Illuminating the chemo-mechanics of hydrogen enhanced fatigue crack growth in aluminum alloys. *Acta Materialia*, 100:232–239, 2015.
- [35] P Ko Liaw and WA Logsdon. Fatigue crack growth threshold at cryogenic temperatures: a review. *Engineering Fracture Mechanics*, 22(4):585–594, 1985.
- [36] X-L Zheng and B-T Lü. Fatigue crack propagation in metals at low temperatures. In *Handbook of fatigue crack propagation in metallic structures*, pages 1385–1412. Elsevier, 1994.
- [37] Ki Jong Park and Chong Soo Lee. Fatigue crack propagation in al-li 8090 alloy at room (300 k) and cryogenic (77 k) temperatures. *Scripta materialia*, 34(2), 1996.
- [38] H Mayer, M Papakyriacou, B Zettl, and S Vacic. Endurance limit and threshold stress intensity of die cast magnesium and aluminium alloys at elevated temperatures. *International journal of fatigue*, 27(9):1076–1088, 2005.
- [39] Y Uematsu, K Tokaji, and M Kawamura. Fatigue behaviour of sic-particulate-reinforced aluminium alloy composites with different particle sizes at elevated temperatures. *Composites Science and Technology*, 68(13):2785–2791, 2008.
- [40] Jean Petit and C Sarrazin-Baudoux. Some critical aspects of low rate fatigue crack

- propagation in metallic materials. *International journal of fatigue*, 32(6):962–970, 2010.
- [41] R Yarullin and I Ishtyryakov. Fatigue surface crack growth in aluminum alloys under different temperatures. *Procedia Engineering*, 160:199–206, 2016.
- [42] J Ruiz and M Elices. Effect of water vapour pressure and frequency on fatigue behaviour in 7017-t651 aluminium alloy plate. *Acta materialia*, 45(1):281–293, 1997.
- [43] JT Burns and RP Gangloff. Effect of loading environment on fatigue crack formation and microstructurally small fatigue propagation in al–zn–mg–cu. *Metall Mater Trans A*, 44:2083–2105, 2012.
- [44] H Ishii and J Weertman. Fatigue crack propagation in copper and cu- al single crystals. *Metallurgical and Materials Transactions B*, 2(12):3441–3452, 1971.
- [45] PJ Cotterill and JF Knott. Effects of temperature and environment on fatigue crack growth mechanisms in a 9% cr 1% mo steel. *Acta metallurgica et materialia*, 40(10):2753–2764, 1992.
- [46] AH Rosenberger, BD Worth, JM Larsen, MV Nathal, R Darolia, CT Liu, PL Martin, DB Miracle, R Wagner, and M Yamaguchi. Structural intermetallics. In *The minerals metals and materials society*, pages 555–561. 1997.
- [47] Robert S Piascik, Richard P Gangloff, Ashok Saxena, et al. Elevated temperature effects on fatigue and fracture. ASTM, 1997.
- [48] G. Henaff, A. Tonneau, and C. Mabru. Near-threshold fatigue crack growth mechanisms in TiAl alloys. *Struct Intermetall*, pages 305–314, 2001.
- [49] J. Petit, G. Henaff, and C. Sarrazin-Baudoux. Environmentally assisted fatigue in the gaseous atmosphere. *Compr Struct Integr*, 6:211—280, 2003.
- [50] Eyouiléki AWI. *Multiscale approach of fatigue crack initiation and propagation in face-centered cubic metals and alloys*. PhD thesis, Sorbonne University, 2021.
- [51] Derek H Warner and WA Curtin. Origins and implications of temperature-dependent activation energy barriers for dislocation nucleation in face-centered cubic metals. *Acta Materialia*, 57(14):4267–4277, 2009.
- [52] Furio Ercolessi and James B Adams. Interatomic potentials from first-principles calculations. *Materials Research Society Symposium Proceedings*, 291:31–36, 1993.
- [53] A.K. Nair, D.H. Warner, and R.G. Hennig. Coupled quantum-continuum analysis of crack tip processes in aluminum. *Journal of the Mechanics and Physics of Solids*, 59(12), 2011.

- [54] Kristopher Learion Baker and DH Warner. An atomistic investigation into the nature of near threshold fatigue crack growth in aluminum alloys. *Engineering Fracture Mechanics*, 115:111–121, 2014.
- [55] James R Rice. Dislocation nucleation from a crack tip: an analysis based on the peierls concept. *Journal of the Mechanics and Physics of Solids*, 40(2):239–271, 1992.
- [56] S Plimpton. Fast Parallel Algorithms for Short-Range Molecular Dynamics. *Journal of Computational Physics*, 117:1–19, 1995.
- [57] S Kohlhoff, P Gumbsch, and HF Fischmeister. Crack propagation in bcc crystals studied with a combined finite-element and atomistic model. *Philosophical Magazine A*, 64(4):851–878, 1991.
- [58] Ellad B Tadmor, Michael Ortiz, and Rob Phillips. Quasicontinuum analysis of defects in solids. *Philosophical magazine A*, 73(6):1529–1563, 1996.
- [59] VB Shenoy, R Miller, EB Tadmor, R Phillips, and M Ortiz. Quasicontinuum models of interfacial structure and deformation. *Physical Review Letters*, 80(4):742, 1998.
- [60] Robert E Rudd and Jeremy Q Broughton. Concurrent coupling of length scales in solid state systems. *Physica status solidi (b)*, 217(1):251–291, 2000.
- [61] LE Shilkrot, Ronald E Miller, and WA Curtin. Coupled atomistic and discrete dislocation plasticity. *Physical review letters*, 89(2):025501, 2002.
- [62] LE Shilkrot, Ronald E Miller, and William A Curtin. Multiscale plasticity modeling: coupled atomistics and discrete dislocation mechanics. *Journal of the Mechanics and Physics of Solids*, 52(4):755–787, 2004.
- [63] AK Nair, DH Warner, RG Hennig, and WA Curtin. Coupling quantum and continuum scales to predict crack tip dislocation nucleation. *Scripta Materialia*, 63(12):1212–1215, 2010.
- [64] Anders Logg, Kent Andre Mardal, and Garth N Wells. *Automated solution of differential equations by the finite element method*, volume 84. Springer-Verlag Berlin Heidelberg, 2012.
- [65] R. Pippan. Dislocation Emission and Fatigue Crack Growth Threshold. *Acta Metallurgica Et Materialia*, 39(3):255–262, 1991.
- [66] V. S. Deshpande, A. Needleman, and E. Van der Giessen. Scaling of Discrete Dislocation Predictions for Near-threshold Fatigue Crack Growth. *Acta Materialia*, 51(15):4637–4651, 2003.

- [67] A. J. Jr. McEVILY and T. L. Johnston. The Role of Cross-Slip in Brittle Fracture and Fatigue. *International Journal of Fracture Mechanics*, 3:45–74, 1967.
- [68] P. K. Liaw, T. R. Lea, and W. A. Logsdon. Near-threshold Fatigue Crack Growth Behavior in Metals. *Acta Metallurgica*, 31(10):1581–1587, 1983.
- [69] M. O. Speidel, M. J. Blackburn, T. R. Beck, and J. A. Feeney. Corrosion Fatigue and Stress Corrosion Crack Growth in High Strength Aluminum Alloys, Magnesium Alloys, and Titanium Alloys Exposed to Aqueous Solutions. *Corrosion fatigue: Chemistry, mechanics and microstructure*, pages 343–345, 1972.
- [70] R. Pippin. The Effective Threshold of Fatigue Crack Propagation in Aluminium Alloys. I. The Influence of Yield Stress and Chemical Composition. *Philosophical Magazine A*, 77(4):861–873, 4 1998.
- [71] J. Wasén and E. Heier. Fatigue Crack Growth Thresholds - the Influence of Young's Modulus and Fracture Surface Roughness. *International Journal of Fatigue*, 20(10):737–742, 1998.
- [72] J. R. Rice and R. Thomson. Ductile versus brittle behaviour of crystals. *Philosophical Magazine*, 29(1):73–97, 1974.
- [73] A. K. Vasudevan, K. Sadananda, and R. L. Holtz. Analysis of vacuum fatigue crack growth results and its implications. *International Journal of Fatigue*, 27(10-12):1519–1529, 2005.
- [74] J. Qian and A. Fatemi. Mixed mode fatigue crack growth: a literature survey. *Engineering fracture mechanics*, 55(6):969–990, 1996.
- [75] S. Biner. Fatigue crack growth studies under mixed-mode loading. *International Journal of Fatigue*, 23:259–263, 2001.
- [76] J. K. Kim and C. S. Kim. Fatigue crack growth behavior of rail steel under mode I and mixed mode loadings. *Materials Science and Engineering: A*, 338(1-2):191–201, 2002.
- [77] S. Seitzl and Z. Knésl. Two parameter fracture mechanics: Fatigue crack behavior under mixed mode conditions. *Engineering Fracture Mechanics*, 75(3-4):857–865, 2008.
- [78] A. L. Silva, A. M. De Jesus, J. Xavier, J. A. F. Correia, and A. A. Fernandes. Combined analytical-numerical methodologies for the evaluation of mixed-mode (I+II) fatigue crack growth rates in structural steels. *Engineering Fracture Mechanics*, 185:124–138, 2017.
- [79] D. Rozumek, Z. Marciniak, G. Lesiuk, J. A. Correia, and A. M. P. de Jesus. Experimental and numerical investigation of mixed mode I+II

- ii and i+ iii fatigue crack growth in s355j0 steel. *International Journal of Fatigue*, 113:160–170, 2018.
- [80] C. E. Inglis. Stresses in a Plate due to the Presence of Cracks and Sharp Corners. *Trans Inst Naval Archit*, 55:219–241, 1913.
- [81] G.M. Bond, I.M. Robertson, and H.K. Birnbaum. The influence of hydrogen on deformation and fracture processes in high-strength aluminum alloys. *Acta Metallurgica*, 35(9):2289–2296, 1987.
- [82] E. Bitzek, J.R Kermode, and P. Gumbsch. Atomistic aspects of fracture. *International Journal of Fracture*, 191(1-2):13–30, 2015.
- [83] P. Andric and W.A. Curtin. Atomistic modeling of fracture. *Modelling and Simulation in Materials Science and Engineering*, 27(1), 2019.
- [84] P. Chowdhury and H. Sehitoglu. Atomistic Energetics and Critical Twinning Stress Prediction in Face and Body Centered Cubic Metals: Recent Progress. *Journal of Engineering Materials and Technology, Transactions of the ASME*, 140(2), 2018.
- [85] J. Zhang and S. Ghosh. Molecular dynamics based study and characterization of deformation mechanisms near a crack in a crystalline material. *Journal of the Mechanics and Physics of Solids*, 61(8):1670–1690, 2013.
- [86] S. Ghosh and J. Zhang. Elastic crack propagation model for crystalline solids using a self-consistent coupled atomistic–continuum framework. *International Journal of Fracture*, 208(1-2):171–189, 2017.
- [87] Alena Uhnáková, Anna MacHová, and Petr Hora. 3D atomistic simulation of fatigue behavior of a ductile crack in bcc iron. *International Journal of Fatigue*, 33(9):1182–1188, 2011.
- [88] D Farkas, M Willemann, and B Hyde. Atomistic mechanisms of fatigue in nanocrystalline metals. *Physical Review Letters*, 94(16):29–32, 2005.
- [89] Paul White. Molecular dynamic modelling of fatigue crack growth in aluminium using LEFM boundary conditions. *International Journal of Fatigue*, 44:141–150, 2012.
- [90] Xiaoling Zhou, Xiaoyan Li, and Changqing Chen. Atomistic mechanisms of fatigue in nanotwinned metals. *Acta Materialia*, 99:77–86, 2015.
- [91] Enqiang Lin and Yongming Liu. Atomistic simulations of fatigue crack growth in single crystal aluminum. *ASME International Mechanical Engineering Congress and Exposition, Proceedings (IMECE)*, 9:1–4, 2013.

- [92] D.C. Slavik, C.P. Blankenship, E.A. Starke, and R.P. Gangloff. Intrinsic fatigue crack growth. *Metallurgical Transactions A*, 24(8):1807–1817, 1993.
- [93] B. Holper, H. Mayer, A. K. Vasudevan, and S. E. Stanzl-Tschegg. Near threshold fatigue crack growth at positive load ratio in aluminium alloys at low and ultrasonic frequency: Influences of strain rate, slip behaviour and air humidity. *International Journal of Fatigue*, 26(1):27–38, 2004.
- [94] R.J.H. Wanhill. Fractography of fatigue crack propagation in 2024-T3 and 7075-16 aluminum alloys in air and vacuum. *Metallurgical Transactions A*, 6(8):1587–1596, 1975.
- [95] J.T. Burns, R.W. Bush, J.H. Ai, J.L. Jones, Y. Lee, and R.P. Gangloff. Effect of water vapor pressure on fatigue crack growth in Al – Zn – Cu – Mg over wide-range stress intensity factor loading. *Engineering Fracture Mechanics*, 137:34–55, 2015.
- [96] M. Gao, P.S. Pao, and R.P. Wei. Chemical and metallurgical aspects of environmentally assisted fatigue crack growth in 7075-T651 aluminum alloy. *Metallurgical Transactions A*, 19(7):1739–1750, 1988.
- [97] A.H. Cottrell and D. Hull. Extrusion and intrusion by cyclic slip in copper. *Proceedings of the Royal Society of London. Series A. Mathematical and Physical Sciences*, 242(1229):211–213, 1957.
- [98] N.F. Mott. A theory of the origin of fatigue cracks. *Acta Metallurgica*, 6(3):195–197, 1958.
- [99] C. Laird and G.C. Smith. Initial stages of damage in high stress fatigue in some pure metals. *Philosophical Magazine*, 8(95):1945–1963, 1963.
- [100] A.K. Vasudévan and K. Sadananda. Classification of fatigue crack growth behavior. *Metallurgical and Materials Transactions A*, 26(5):1221–1234, 1995.
- [101] S. Suresh. *Fatigue of Materials*. Cambridge University Press, 2nd edition, 1998.
- [102] T. Tang, S. Kim, and M.F. Horstemeyer. Fatigue crack growth in magnesium single crystals under cyclic loading: Molecular dynamics simulation. *Computational Materials Science*, 48(2):426–439, 2010.
- [103] G.P. Potirniche and M.F. Horstemeyer. On the growth of nanoscale fatigue cracks. *Philosophical Magazine Letters*, 86(3):185–193, 2006.
- [104] M. Ladinek and T. Hofer. On the influence of loading order in nanostructural fatigue crack propagation in BCC Iron—a molecular dynamics study. *Metals*, 9(6):1–12, 2019.
- [105] X.T. Shu, S.F. Xiao, H.Q. Deng, L. Ma, and W. Hu. Atomistic simulation of crack

- propagation in single crystal tungsten under cyclic loading. *Journal of Materials Research*, 32(8):1474–1483, 2017.
- [106] A. Machová, J. Pokluda, Al. Uhnáková, and P. Hora. 3D atomistic studies of fatigue behaviour of edge crack (0 0 1) in bcc iron loaded in mode I and II. *International Journal of Fatigue*, 66:11–19, 2014.
- [107] W.P. Wu, Y.L. Li, and X.Y. Sun. Molecular dynamics simulation-based cohesive zone representation of fatigue crack growth in a single crystal nickel. *Computational Materials Science*, 109:66–75, 2015.
- [108] R.Z. Qiu, Y.C. Lin, and T.H. Fang. Fatigue crack growth characteristics of Fe and Ni under cyclic loading using a quasi-continuum method. *Beilstein Journal of Nanotechnology*, 9(1):1000–1014, 2018.
- [109] R.E. Miller and E.B. Tadmor. A unified framework and performance benchmark of fourteen multiscale atomistic/continuum coupling methods. *Modelling and Simulation in Materials Science and Engineering*, 17(5), 2009.
- [110] L.E. Shilkrot, R.E. Miller, and W.A. Curtin. Multiscale plasticity modeling: Coupled atomistics and discrete dislocation mechanics. *Journal of the Mechanics and Physics of Solids*, 52(4):755–787, 2004.
- [111] V.I. Yamakov, D.H. Warner, R.J. Zamora, E. Saether, W.A. Curtin, and E.H. Glaessgen. Investigation of crack tip dislocation emission in aluminum using multiscale molecular dynamics simulation and continuum modeling. *Journal of the Mechanics and Physics of Solids*, 65(1):35–53, 2014.
- [112] M.O. Speidel, M.J. Blackburn, T.R. Beck, and J.A. Feeney. Corrosion fatigue and stress corrosion crack growth in high strength aluminum alloys, magnesium alloys, and titanium alloys exposed to aqueous solutions. *Corrosion fatigue: Chemistry, mechanics and microstructure*, pages 343–345, 1972.
- [113] A.J. McEvily and T.L. Johnston. The role of cross-slip in brittle fracture and fatigue. *International Journal of Fracture Mechanics*, 3:45–74, 1967.
- [114] D.H. Warner, W.A. Curtin, and S. Qu. Rate dependence of crack-tip processes predicts twinning trends in f.c.c. metals. *Nature Materials*, 6(11):876–881, 2007.
- [115] R. Pippin and H. Weinhandl. Discrete dislocation modelling of near threshold fatigue crack propagation. *International Journal of Fatigue*, 32(9):1503–1510, 2010.
- [116] A.J. Wilkinson, S.G. Roberts, and P.B. Hirsch. Modelling the threshold conditions for propagation of stage I fatigue cracks. *Acta Materialia*, 46(2):379–390, 1998.

- [117] K. Sadananda and P. Shahinian. Prediction of threshold stress intensity for fatigue crack growth using a dislocation model. *International Journal of Fracture*, 13(5):585–594, 1977.
- [118] C.H. Wells. An Analysis of the Effect of Slip Character on Cyclic Deformation and Fatigue. *Acta Metallurgica*, 17:443–449, 1969.
- [119] X.J. Wu, A.K. Koul, and A.S. Krausz. A transgranular fatigue crack growth model based on restricted slip reversibility. *Metallurgical Transactions A*, 24(6):1373–1380, 1993.
- [120] C. Fong and D. Tromans. High frequency stage I corrosion fatigue of austenitic stainless steel (316L). *Metallurgical Transactions A*, 19(11):2753–2764, 1988.
- [121] J.A. Ewing and J.C.W. Humfrey. VI. The fracture of metals under repeated alternations of stress. *Philosophical Transactions of the Royal Society of London. Series A, Containing Papers of a Mathematical or Physical Character*, 200:321–330, 1903.
- [122] P.J.E. Forsyth. Exudation of Material from Slip Bands at the Surface of Fatigued Crystals of an Aluminium-Copper Alloy. *Nature*, 171(4343):172–173, 1953.
- [123] Z. Fan, O.H. Duparc, and M. Sauzay. Molecular dynamics simulation of surface step reconstruction and irreversibility under cyclic loading. *Acta Materialia*, 102:149–161, 2016.
- [124] K.L. Baker and D.H. Warner. Extended timescale atomistic modeling of crack tip behavior in aluminum. *Modelling and Simulation in Materials Science and Engineering*, 20(6), 2012.
- [125] E. Bitzek and P. Gumbsch. Mechanisms of dislocation multiplication at crack tips. *Acta Materialia*, 61(4):1394–1403, 2013.
- [126] M. Sauzay and M.O. Moussa. Prediction of grain boundary stress fields and microcrack initiation induced by slip band impingement. *International Journal of Fracture*, 184(1-2):215–240, 2013.
- [127] A.J. McEvily and R.G. Boettner. On fatigue crack propagation in F.C.C. metals. *Acta Metallurgica*, 11:725–743, 1963.
- [128] A. K. Nair, D. H. Warner, and R. G. Hennig. Coupled quantum-continuum analysis of crack tip processes in aluminum. *Journal of the Mechanics and Physics of Solids*, 59(12):2476–2487, 2011.
- [129] V. P. Rajan, D. H. Warner, and W. A. Curtin. An interatomic pair potential with tunable intrinsic ductility. *Modelling and Simulation in Materials Science and Engineering*, 24(2), 2016.

- [130] E. Van der Giessen and A. Needleman. Modelling and Simulation in Materials Science and Engineering Related content Discrete dislocation plasticity : a simple planar model Discrete dislocation plasticity : a simple planar model. *Modelling and Simulation in Materials Science and Engineering*, 3:689–735, 1995.
- [131] S. P. Lynch. Environmentally assisted cracking: Overview of evidence for an adsorption-induced localised-slip process. *Acta Metallurgica*, 36(10):2639–2661, 1988.
- [132] J. T. Burns, R. W. Bush, J. H. Ai, J. L. Jones, Y. Lee, and R. P. Gangloff. Effect of Water Vapor Pressure on Fatigue Crack Growth in Al-Zn-Cu-Mg over Wide-range Stress Intensity Factor Loading. *Engineering Fracture Mechanics*, 137:34–55, 2015.
- [133] R. L. Eadie, K. E. Szklarz, and R. L. Sutherby. Corrosion Fatigue and Near-neutral pH Stress Corrosion Cracking of Pipeline Steel and the Effect of Hydrogen Sulfide. *Corrosion*, 61(2):167–173, 2005.
- [134] P. M. Scott and A. E. Truswell. Corrosion Fatigue Crack Growth in Reactor Pressure Vessel Steels in PWR Primary Water. *Journal of Pressure Vessel Technology, Transactions of the ASME*, 105(3):245–254, 1983.
- [135] A. Creager and P. C. Paris. Elastic field equations for blunt cracks with reference to stress corrosion cracking. *International Journal of Fracture Mechanics*, 3:247–252, 1967.
- [136] J. C. Radon, C. M. Branco, and L. E. Culver. Crack Blunting and Arrest in Corrosion Fatigue of Mild Steel. *International Journal of Fracture*, 12(3):467–469, 1976.
- [137] I. M. Austen. *Quantitative Understanding of Corrosion Fatigue Crack Growth Behaviour*. Commission of the European Communities, Directorate-General Science, Research and Development., 1983.
- [138] D. A. Wheeler, R. G. Hoagland, and J. P. Hirth. Evidence for Crack Tip Oxidation Effects During the Liquid Metal Embrittlement of AA 7075 Aluminum Alloy by Mercury. *Corrosion*, 45(3):207–212, 1989.
- [139] P. J. L. Fernandes and D. R. H. Jones. The Effect of Temperature on Fatigue Crack Growth in Liquid Metal Environments. *Corrosion Science*, 38(5):745–754, 1996.
- [140] J. F. Charles and A. O. Aliprantis. Osteoclasts: More than ‘Bone Eaters’. *Trends in molecular medicine*, 20(8):449–459, 2014.
- [141] Pliny the Elder. *Natural History*. London, A. Islip, 1634.

- [142] I M Robertson and H K Birnbaum. An HVEM study of hydrogen effects on the deformation and fracture of nickel. *Acta Metallurgica*, 34(3):353–366, 1986.
- [143] G. O. Ilevbare, O. Schneider, R. G. Kelly, and J. R. Scully. In Situ Confocal Laser Scanning Microscopy of AA 2024-T3 Corrosion Metrology : I . Localized Corrosion of Particles In Situ Confocal Laser Scanning Microscopy of AA 2024-T3 Corrosion Metrology. *Journal ofThe Electrochemical Society*, 151(8):453–464, 2004.
- [144] A. Turnbull. Corrosion Pitting and Environmentally Assisted Small Crack Growth. *Proceedings of the Royal Society A*, 470(2169), 2014.
- [145] T. J. Stannard, J. J. Williams, and S. S. Singh. 3d Time-Resolved Observations of Corrosion and Corrosion-Fatigue Crack Initiation and Growth in Peak-Aged Al 7075 Using Synchrotron X-Ray Tomography. *Corrosion Science*, 138(November 2017):340–352, 2018.
- [146] S Suresh. *Fatigue of Materials*. Cambridge University Press, 10 1998.
- [147] R. P. Gangloff. Corrosion Fatigue Crack Propagation in Metals. pages 55–109, 1989.
- [148] V. P. Rajan, D. H. Warner, and W. A. Curtin. An Interatomic Pair Potential with Tunable Intrinsic Ductility. *Modelling and Simulation in Materials Science and Engineering*, 24(2), 2016.
- [149] D. H. Warner, W. A. Curtin, and S. Qu. Rate dependence of crack-tip processes predicts twinning trends in f.c.c. metals. *Nature Materials*, 6(11), 2007.
- [150] G. Venkatramani, S. Ghosh, and M. Mills. A Size-Dependent Crystal Plasticity Finite-Element Model for Creep and Load Shedding in Polycrystalline Titanium Alloys. *Acta Materialia*, 55(11):3971–3986, 2007.
- [151] V. I. Yamakov, D. H. Warner, R. J. Zamora, E. Saether, W. A. Curtin, and E. H. Glaessgen. Investigation of Crack Tip Dislocation Emission in Aluminum Using Multiscale Molecular Dynamics Simulation and Continuum Modeling. *Journal of the Mechanics and Physics of Solids*, 65(1), 2014.
- [152] Z. Fan, O. Hardouin Duparc, and M. Sauzay. Molecular Dynamics Simulation of Surface Step Reconstruction and Irreversibility under Cyclic Loading. *Acta Materialia*, 102:149–161, 2016.
- [153] M Zhao, W Gu, and D. H. Warner. Atomic mechanism of near threshold fatigue crack growth in vacuum. [*Unpublished manuscript*], 2021.
- [154] E N da C Andrade. The Rehbinder Effect. *Proceedings of the Physical Society.*, 63:990–995, 1950.

- [155] S. P. Lynch. The Mechanism of Liquid-Metal Embrittlement-Crack Growth in Aluminum Single Crystals and Other Metals in Liquid-Metal Environments. Technical report, Aeronautical Research Laboratories, 1977.
- [156] Jr. Hudak, S. J., D. L. Davidson, and R. A. Page. The Role of Crack-tip Deformation in Corrosion Fatigue Crack Growth. *Embrittlement by the Localized Crack Environment*, pages 173–197, 1984.
- [157] F. P. Ford. Status of Research on Environmentally Assisted Cracking in LWR Pressure Vessel Steels. *Journal of Pressure Vessel Technology*, 110, 1988.
- [158] T. P. Hoar and J. M. West. Mechano-Chemical Anodic Dissolution. *Nature*, 181(4612):835–835, 1958.
- [159] T. P. Hoar and J. C. Scully. Mechanochemical Anodic Dissolution of Austenitic Stainless Steel in Hot Chloride Solution at Controlled Electrode Potential. *Journal of The Electrochemical Society*, 111, 1964.
- [160] J. C. Scully. The Mechanical Parameters of Stress-Corrosion Cracking. *Corrosion Science*, 8(10):759–769, 1968.
- [161] R. W. Revie and H. H. Uhlig. *Corrosion and Corrosion Control*. John Wiley & Sons, 2008.
- [162] M. E. Hoffman and P. C. Hoffman. Corrosion and Fatigue Research - Structural Issues and Relevance to Naval Aviation. *International Journal of Fatigue*, 23:1–10, 2001.
- [163] G. E. Nordmark and W. G. Fricke. Fatigue Crack Arrest at Low Stress Intensities in a Corrosive Environment. *Journal of Testing and Evaluation*, 6(5):301–303, 1978.
- [164] R. van der Velden, H. L. Ewalds, W. A. Schultze, and A. Punter. Anomalous Fatigue Crack Growth Retardation in Steels for Offshore Applications. In *Corrosion Fatigue: Mechanics, Metallurgy, Electrochemistry, and Engineering*, pages 64–80. ASTM International, 1983.
- [165] W. A. Stoop, N. Uphoff, and A. Kassam. A review of agricultural research issues raised by the system of rice intensification (sri) from madagascar: opportunities for improving farming systems for resource-poor farmers. *Agricultural Systems*, 71:249–274, 2002.
- [166] M. Noltze, S. Schwarze, and M. Qaim. Understanding the adoption of system

- technologies in smallholder agriculture: The system of rice intensification (sri) in timor leste. *Agricultural Systems*, 108:64 – 73, 2012.
- [167] A. Satyanarayana, T. M. Thiyagarajan, and N. Uphoff. Opportunities for water saving with higher yield from the system of rice intensification. *Irrigation Science*, 25(2):99–115, Jan 2007.
- [168] P. C. Mohapatra, M. Din, B. C. Parida, S. P. Patel, P. Mishra, et al. Effect of mechanical planting and weeding on yield, water-use efficiency and cost of production under modified system of rice intensification. *Indian Journal of Agricultural Sciences*, 82(3):280–283, 2012.
- [169] A. Sharif. Technical adaptations for mechanized sri production to achieve water saving and increased profitability in punjab, pakistan. *Paddy and Water Environment*, 9(1):111–119, 2011.
- [170] B. Abraham, H. Araya, T. Berhe, S. Edwards, B. Gujja, R. B. Khadka, Y. S. Koma, D. Sen, A. Sharif, E. Styger, et al. The system of crop intensification: reports from the field on improving agricultural production, food security, and resilience to climate change for multiple crops. *Agriculture & Food Security*, 3(1):4, 2014.
- [171] S. K. Sinha and J. Talati. Productivity impacts of the system of rice intensification (sri): A case study in west bengal, india. *Agricultural Water Management*, 87(1):55 – 60, 2007.
- [172] B. Mueller. Additive manufacturing technologies—rapid prototyping to direct digital manufacturing. *Assembly Automation*, 32(2), 2012.
- [173] D. S. Thomas and S. W. Gilbert. Costs and cost effectiveness of additive manufacturing. *NIST Special Publication*, 1176:12, 2014.
- [174] W. E. Frazier. Metal additive manufacturing: a review. *Journal of Materials Engineering and Performance*, 23(6):1917–1928, 2014.
- [175] S. Chekurov and M. Salmi. Additive manufacturing in offsite repair of consumer electronics. *Physics Procedia*, 89:23 – 30, 2017. 16th Nordic Laser Materials Processing Conference, NOLAMP16.
- [176] K. V. Wong and A. Hernandez. A review of additive manufacturing. *ISRN Mechanical Engineering*, 2012, 2012.
- [177] J. Pearce. Applications of Open Source 3-D Printing on Small Farms. *Organic Farming*, 1(1):19 – 35, December 2013.
- [178] F. R. Ishengoma and A. B. Mtaho. 3d printing: developing countries perspectives. *International Journal of Computer Applications*, 104(11):30 – 34, 2014.

- [179] T. Birtchnell and W. Hoyle. *3D printing for development in the global south: The 3D4D challenge*. Springer, 2014.
- [180] N. Hopkinson and P. Dicknes. Analysis of rapid manufacturing—using layer manufacturing processes for production. *Proceedings of the Institution of Mechanical Engineers, Part C: Journal of Mechanical Engineering Science*, 217(1):31–39, 2003.
- [181] M. Ruffo, C. Tuck, and R. Hague. Cost estimation for rapid manufacturing—laser sintering production for low to medium volumes. *Proceedings of the Institution of Mechanical Engineers, Part B: Journal of Engineering Manufacture*, 220(9):1417–1427, 2006.
- [182] E. Atzeni and A. Salmi. Economics of additive manufacturing for end-usable metal parts. *The International Journal of Advanced Manufacturing Technology*, 62(9-12):1147–1155, 2012.
- [183] B.T. Wittbrodt, A.G. Glover, J. Laureto, G.C. Anzalone, D. Oppliger, J.L. Irwin, and J.M. Pearce. Life-cycle economic analysis of distributed manufacturing with open-source 3-d printers. *Mechatronics*, 23(6):713 – 726, 2013.
- [184] A. Emelogu, M. Marufuzzaman, S. M. Thompson, N. Shamsaei, and L. Bian. Additive manufacturing of biomedical implants: A feasibility assessment via supply-chain cost analysis. *Additive Manufacturing*, 11:97 – 113, 2016.
- [185] G. Costabile, M. Fera, F. Fruggiero, A. Lambiase, and D. Pham. Cost models of additive manufacturing: A literature review. *International Journal of Industrial Engineering Computations*, 8(2):263–283, 2017.
- [186] V. R. Haden, J. M. Duxbury, A. DiTommaso, and J. E. Losey. Weed community dynamics in the system of rice intensification (sri) and the efficacy of mechanical cultivation and competitive rice cultivars for weed control in indonesia. *Journal of Sustainable Agriculture*, 30(4):5–26, 2007.
- [187] 3Ders. Price compare - 3d printers. Retrieved September 6, 2019; Available from: <http://www.3ders.org/pricecompare/3dprinters/>.
- [188] U.S. Bureau of Labor Statistics. Employer costs for employee compensation. 2019.
- [189] New York Department of Labor. Minimum wage order for miscellaneous industries and occupations. 2016.
- [190] M. Salmi, I. F. Ituarte, S. Chekurov, and E. Huotilainen. Effect of build orientation in 3d printing production for material extrusion, material jetting, binder

- jetting, sheet object lamination, vat photopolymerisation, and powder bed fusion. *International Journal of Collaborative Enterprise*, 5(3-4):218–231, 2016.
- [191] S. Park and D. W. Rosen. Quantifying effects of material extrusion additive manufacturing process on mechanical properties of lattice structures using as-fabricated voxel modeling. *Additive Manufacturing*, 12:265 – 273, 2016. Special Issue on Modeling & Simulation for Additive Manufacturing.
- [192] J. R. C. Dizon, A. H. Espera, Q. Chen, and R. C. Advincula. Mechanical characterization of 3d-printed polymers. *Additive Manufacturing*, 20:44 – 67, 2018.
- [193] P Li, DH Warner, and N Phan. Predicting the fatigue performance of an additively manufactured ti-6al-4v component from witness coupon behavior, 2020.
- [194] JW Pegues, S Shao, N Shamsaei, N Sanaei, A Fatemi, DH Warner, P Li, and N Phan. Fatigue of additive manufactured ti-6al-4v, part i: The effects of powder feedstock, manufacturing, and post-process conditions on the resulting microstructure and defects. *International Journal of Fatigue*, 132:105358, 2020.
- [195] R Molaei, A Fatemi, N Sanaei, J Pegues, N Shamsaei, S Shao, P Li, DH Warner, and N Phan. Fatigue of additive manufactured ti-6al-4v, part ii: The relationship between microstructure, material cyclic properties, and component performance. *International Journal of Fatigue*, 132:105363, 2020.
- [196] G. C. Anzalone, C. Zhang, B. Wijnen, P. G. Sanders, and J. M. Pearce. A low-cost open-source metal 3-d printer. *IEEE Access*, 1:803–810, 2013.
- [197] A. S. Haselhuhn, B. Wijnen, G. C. Anzalone, P. G. Sanders, and J. M. Pearce. In situ formation of substrate release mechanisms for gas metal arc weld metal 3-d printing. *Journal of Materials Processing Technology*, 226:50 – 59, 2015.
- [198] YuMing Zhang, Yiwei Chen, Pengjiu Li, and Alan T Male. Weld deposition-based rapid prototyping: a preliminary study. *Journal of Materials Processing Technology*, 135(2-3):347–357, 2003.
- [199] Amberlee S Haselhuhn, Eli J Gooding, Alexandra G Glover, Gerald C Anzalone, Bas Wijnen, Paul G Sanders, and Joshua M Pearce. Substrate release mechanisms for gas metal arc weld 3d aluminum metal printing. *3D Printing and Additive Manufacturing*, 1(4):204–209, 2014.
- [200] Donghong Ding, Zengxi Pan, Dominic Cuiuri, and Huijun Li. Wire-feed additive manufacturing of metal components: technologies, developments and future interests. *The International Journal of Advanced Manufacturing Technology*, 81(1-4):465–481, 2015.
- [201] Stewart W Williams, Filomeno Martina, Adrian C Addison, Jialuo Ding, Goncalo

- Pardal, and P Colegrove. Wire+ arc additive manufacturing. *Materials Science and Technology*, 32(7):641–647, 2016.
- [202] Dirk Herzog, Vanessa Seyda, Eric Wycisk, and Claus Emmelmann. Additive manufacturing of metals. *Acta Materialia*, 117:371–392, 2016.
- [203] X Lu, YF Zhou, XL Xing, LY Shao, QX Yang, and SY Gao. Open-source wire and arc additive manufacturing system: formability, microstructures, and mechanical properties. *The International Journal of Advanced Manufacturing Technology*, 93(5-8):2145–2154, 2017.
- [204] Johnnieew Zhong Li, Mohd Rizal Alkahari, Nor Ana Binti Rosli, Rafidah Hasan, Mohd Nizam Sudin, and Faiz Redza Ramli. Review of wire arc additive manufacturing for 3d metal printing. *International Journal of Automation Technology*, 13(3):346–353, 2019.
- [205] Yuming Zhang, University of Kentucky (email communication, Jun 10, 2020).
- [206] Filomeno Martina, WAAM3D (email communication, Jun 12, 2020).
- [207] S. H. Masood and W. Q. Song. Development of new metal/polymer materials for rapid tooling using fused deposition modelling. *Materials & design*, 25(7):587–594, 2004.
- [208] C. W. Lee, C. K. Chua, C. M. Cheah, L. H. Tan, and C. Feng. Rapid investment casting: direct and indirect approaches via fused deposition modelling. *The International Journal of Advanced Manufacturing Technology*, 23(1):93–101, Jan 2004.
- [209] P. Kumar, I. P. S. Ahuja, and R. Singh. Application of fusion deposition modelling for rapid investment casting- a review. *International Journal of Materials Engineering Innovation*, 3(3-4):204–227, 2012.
- [210] P. Chung, J. A. Heller, M. Etemadi, P. E. Ottoson, J. A. Liu, L. Rand, and S. Roy. Rapid and low-cost prototyping of medical devices using 3d printed molds for liquid injection molding. *Journal of Visualized Experiments*, (88):e51745, 2014.